DOUBLY CABIBBO SUPPRESSED DECAYS OF THE CHARGED *D* MESON

James Stephen Wiener

A DISSERTATION
PRESENTED TO THE FACULTY
OF PRINCETON UNIVERSITY
IN CANDIDACY FOR THE DEGREE
OF DOCTOR OF PHILOSOPHY

RECOMMENDED FOR ACCEPTANCE
BY THE DEPARTMENT OF
PHYSICS

November 1994

Acknowledgements

High energy physics is first and foremost a collaborative effort. The individuals who deserve mention for making a crucial contribution to this work are numerous. They include all the members of the E791 collaboration without whose superlative work and love of physics this thesis could not have been written. As well as the previous collaborations (E516, E691,E769) that constructed parts of the E791 spectrometer.

Despite the impossibility of acknowledging in detail all those who made important contributions to my work, I would like to mention several of the physicists who have helped me the most in what is an admittedly incomplete list.

My advisor, Milind Purohit, for teaching me how to be an experimental high energy physicist. Mike Sokoloff, Guy Blaylock, Jeff Appel, and Ai Nguyen for carefully examining my work and providing thoughtful comments and suggestions. Steve Bracker for giving me the conviction that the only way to do things is the right way. Finally, Tom Carter, Scott Radetzsky, Nick Witchey, Keith Thorne, Krish Gounder, and Ai Nguyen for providing much help and friendship.

Abstract

Doubly Cabibbo suppressed decays of the D^+ test theories of hadronic charm decay. They are also intrinsically interesting because no DCSDs of charmed mesons have been observed.

In this thesis, we report on the results of a high sensitivity search for the doubly Cabibbo suppressed decays $D^+ \rightarrow K^+\pi^+\pi^-$ and $D^+ \rightarrow K^+K^+K^-$ and the resonant modes $D^+ \rightarrow K^*(892)\pi^+$ and $D^+ \rightarrow K^+\phi$. The data are from Fermilab experiment E791, a fixed target experiment in the proton beam line.

We measure $\frac{\Gamma(D^+\rightarrow K^+\pi^+\pi^-)}{\Gamma(D^+\rightarrow K^-\pi^+\pi^+)} \times \frac{1}{tan^4\theta_c} = 3.5 \pm 1.1 \pm 0.4$ and $\frac{\Gamma(D^+\rightarrow K^*(892)\pi^+)}{\Gamma(D^+\rightarrow K^-\pi^+\pi^+)} \times \frac{1}{tan^4\theta_c} = 2.9 \pm 1.0 \pm 0.2$. These results add to the body of evidence that suggests the source of the discrepancy between the D^+ lifetime on one hand and the D^0 and D_s^+ lifetimes on the other hand is destructive interference in the D^+ hadronic diagrams.

We set a limit $\frac{\Gamma(D^+\rightarrow K^+K^+K^-)}{\Gamma(D^+\rightarrow K^-\pi^+\pi^+)} < 0.0044$ @ 90% CL which contradicts an observation of this mode by WA82. We also set the limit $\frac{\Gamma(D^+\rightarrow\phi K^+)}{\Gamma(D^+\rightarrow\phi\pi^+)} < 0.0524$ @ 90% CL which is consistent with an observation of this mode by E691.

Contents

List of Figures

List of Tables

Chapter 1

Theoretical Framework

1.1 Introduction

The Standard Model is the theoretical paradigm of high energy physics. According to the Standard Model, the physics of electroweak interactions of charm quarks should be among the most uninteresting in the theory. The charged current couplings of charm quarks are known to be given by the Cabibbo angle to a high degree of accuracy, the theory predicts very small $D^0 - \overline{D^0}$ mixing, and no CP violation [Bi88a]. However, in another light these shortcomings can viewed as assets. The lack of more interesting standard model interactions means that charmed hadrons can be a "clean" laboratory in which to study hadron dynamics. Also, since the Standard Model predictions of $D^0 - \overline{D}^0$ mixing and CP violation are so small, any observation of these phenomena would be indicative of new physics. This thesis will describe a high sensitivity search for some of the doubly Cabibbo suppressed decays (DCSDs) of the D^+. In addition a high sensitivity search for CP violation in D^+ decays will be described. These are of interest both as observations of as yet undiscovered decays and as another chance to confront the theory of charm meson dynamics with experiment.

1.2 The Standard Model

The Standard Model is a gauge field theory. As such, enumerating the theory is in large part equivalent to identifying its constituent particles and their properties. The fundamental elements of matter in the model are three families of fermions.

$$\begin{pmatrix} u & e \\ d & \nu_e \end{pmatrix} \quad \begin{pmatrix} c & \mu \\ s & \nu_\mu \end{pmatrix} \quad \begin{pmatrix} t & \tau \\ b & \nu_\tau \end{pmatrix}$$

Each family contains two quarks and two leptons. Because of the properties of the strong force, isolated quarks are never observed. Instead they are always dressed in mesons ($q\overline{q}$ pairs) and baryons (qqq triplets).

Interactions in the theory are invariant under the application of the gauge group $G = SU(3) \times SU(2) \times U(1)$. The symmetries of this group give rise to 12 gauge bosons; 8 gluons, the $W^{\pm}$, the Z^0, and the γ, which mediate interactions between the theory's fermions.

The U(1) electromagnetic symmetry is manifested in the photon which mediates interactions between electrically charged quarks and leptons. While this interaction is probably the most important and familiar, it doesn't bear directly on the physics of this thesis.

The SU(2) weak symmetry consists of both a flavour changing charged current , the $W^{\pm}$, and a flavour conserving neutral current, the Z^0. The charged current interactions are responsible for doubly Cabibbo suppressed decays. The coupling of the charged current interaction is assumed to be universal, that is the decays

$$u \to d' \qquad c \to s' \qquad t \to b'$$

are of the same strength. The d', s', and b' states are superpositions of the d, s, and b mass eigenstates. The Cabibbo-Kobayashi-Maskawa (CKM) matrix rotates the quark mass eigenstates into the weak decay eigenstates (equation 1.1). The lepton weak and mass eigenstates are identical and hence their coupling to the W is 1.

$$\begin{pmatrix} d' \\ s' \\ b' \end{pmatrix} = \begin{pmatrix} V_{ud} & V_{us} & V_{ub} \\ V_{cd} & V_{cs} & V_{cb} \\ V_{td} & V_{ts} & V_{tb} \end{pmatrix} \begin{pmatrix} d \\ s \\ b \end{pmatrix} \tag{1.1}$$

The varying magnitudes of the elements of the CKM matrix mean that the strength of the transitions between the mass eigenstates is not universal. In particular the (d, s) subspace is known to be parameterized to a high degree of accuracy by the Cabibbo angle.

$$\begin{pmatrix} d' \\ s' \end{pmatrix} = \begin{pmatrix} \cos\theta_c & \sin\theta_c \\ -\sin\theta_c & \cos\theta_c \end{pmatrix} \begin{pmatrix} d \\ s \end{pmatrix}$$

Therefore, decays involving charm-down, and up-strange vertices are suppressed relative to charm-strange, and up-down vertices. Doubly Cabibbo suppressed decays involve two Cabibbo suppressed vertices.

The SU(3) color symmetry gives rise to 8 gluons which mediate the strong force. The strong force modifies the quark currents and the meson states in weak transitions. Attempts to include strong force effects in the theory of the charm meson decays have been made by Bauer, Stech, and Wirbel and others. One of the motivations for studying DCSDs is to compare these models with experiment.

1.3 The Discovery of Charm

As early as 1964, a fourth quark was speculated to exist in order to complete the symmetry between the number of quarks and leptons. The idea was reintroduced

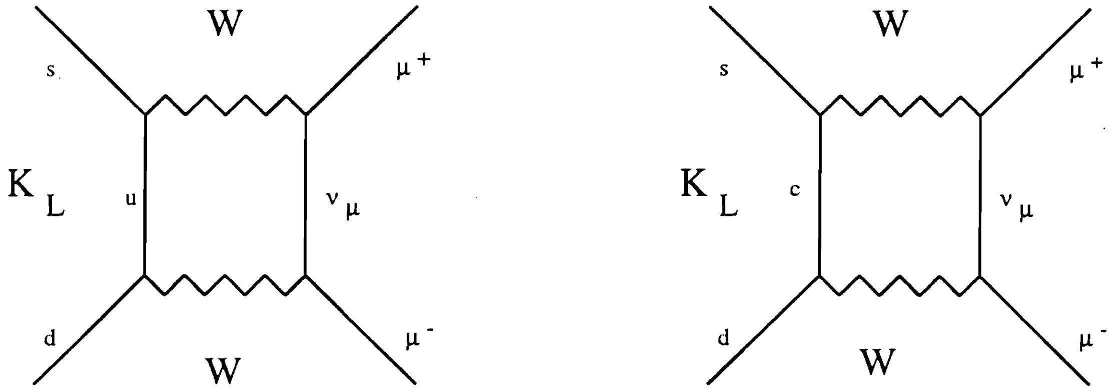

$A \propto \cos\theta_c \sin\theta_c$ $A \propto -\cos\theta_c \sin\theta_c$

Figure 1.1: $K_L \to \mu^+\mu^-$

in 1970 by Glashow, Iliopoulos, and Maiani [Gl70] in order explain the absence of flavour changing neutral currents in K meson decays. For instance, the decay $K_L \to \mu^+\mu^-$ was known to be highly suppressed.

The diagrams illustrated in figure 1.1 contribute to the $K_L \to \mu^+\mu^-$ decay.

Since the amplitudes enter with opposite signs they cancel, if the mass difference between the u and c quark can be ignored. This famous effect is called the GIM mechanism and it is made possible by the existence of a fourth quark. The quark was called charm, precisely because in the context of the Standard Model it wards off this evil.

The discovery in November 1974 of a very narrow resonance at 3.1 GeV was made independently in $e^+ e^-$ annihilation at SLAC and proton-proton collisions at Brookhaven. This resonance, the J/Ψ particle, was immediately interpreted as a bound state of a $c\bar{c}$ pair. It was one of the seminal events in high energy physics. It established the Standard Model as the leading theory of elementary particle interactions.

1.4 The Spectator Model of D Meson decays

There are four mechanisms by which charm mesons can decay; spectator decays (figure 1.2a), W-annihilation (figure 1.2b), internal emission (figure 1.2c), and W-exchange (figure 1.2d). Naively, the dominant process should be the spectator diagram, since the internal emission diagram should be suppressed by color matching and the W-exchange and W-annihilation diagrams are helicity suppressed (angular and linear momentum conservation require right-handed fermions and left-handed anti-fermions at the light quark vertex). In addition, the W-exchange and annihilation diagrams are "wave function" suppressed. The annihilation diagram 1(b) requires the overlap of the c and $\bar{s}$ quark's wave function in order to proceed. Also, since at the mass scale of the D mesons the weak force is point like, diagram 1(d) also requires a similar overlap of wave functions. Therefore, the partial width of these decay mechanisms is given by

$$\Gamma_{WA} \propto G_F^2 |f_D|^2 m_\pi^2 \qquad \text{[Bi88a]}$$

Where, f_D is the D decay constant. Since, $f_D \approx 0.2$ GeV the WA partial width should be suppressed by approximately a factor of 500.

By assuming the spectator diagram dominates one can obtain a simple estimate of the lifetimes of the D^0, D^+, and D_s^+ mesons (equation 1.2). Where the factor of 5 is from the 2 possible semileptonic decays and the 3 possible Cabibbo favored hadronic decays (counting color). The experimental values for these lifetimes [PDG92] are of the same order of magnitude as this prediction.

$$\tau_{D^0} = \tau_{D^+} = \tau_{D_s^+} = 5\frac{G_F^2 m_c^5}{192\pi^3} \approx 9 \times 10^{-13} sec \tag{1.2}$$

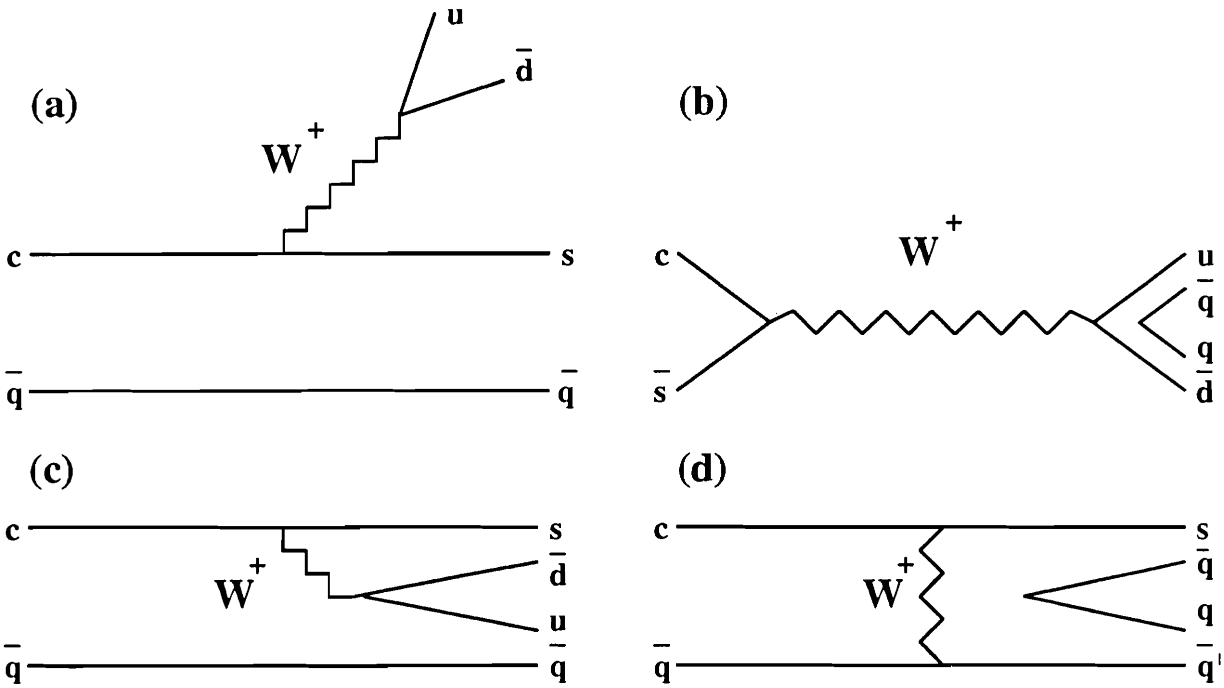

Figure 1.2: Cabibbo favored charm meson hadronic decay mechanisms:
(a) Spectator, (b) W-annihilation, (c) internal W-emission, and (d) W-exchange

$$\tau_{D^0} = 4.21 \pm .10 \times 10^{-13} sec$$

$$\tau_{D^+} = 10.66 \pm .23 \times 10^{-13} sec$$

$$\tau_{D_s^+} = 4.50^{+.30}_{-.28} \times 10^{-13} sec$$

However, the Spectator Model fails to predict $\tau_D^+ \approx 2.5 \times \tau_{D^0}, \tau_{D_s^+}$. This discrepancy has been the focus of much experimental and theoretical work in the past 10 years. An important fact is that semileptonic partial widths for each of these mesons are equal to within experimental precision[PDG92]. This suggests that hadronic effects are responsible for the discrepancy.

$$\Gamma^{SL}_{D^0} = 1.81 \pm .18 \times 10^{13} sec^{-1}$$

$$\Gamma^{SL}_{D^+} = 1.83 \pm .29 \times 10^{13} sec^{-1}$$

$$\Gamma^{SL}_{D_s^+} = 1.1 \pm 1.2 \times 10^{13} sec^{-1}$$

Note, however that it is the D^+ semileptonic branching ratio which comes out in accordance with the naive Standard Model prediction of 20%. The current explanation for this anomaly is an overall enhancement, by about a factor of two, of the non-leptonic decay modes of all D Mesons.

One possible is explanation is that the WA diagrams (W-exchange and W-annihilation diagrams) which are Cabibbo suppressed for the D^+ (figure 1.3a), contribute to the total width. Since the Cabibbo favored form of these diagrams exist for the D_s^+ (figure 1.3b) and the D^0 (figure 1.3c) this would explain their greater total width. It may be that because of the presence of additional particles, such as gluons, the helicity suppression of these diagrams can be obviated. However, the "wave function" suppression remains. Therefore, it is believed that a more likely possibility is that the spectator diagram of D^+ is somehow suppressed. The spectator decay of the D^+ has two identical anti-down quarks in its final state. The exchange of these particles should introduce a minus sign (by Fermi statistics) in the amplitude for the spectator decays. This destructive interference might be responsible for the longer D^+ lifetime (see Figure 1.4). These qualitative arguments make the need for a more sophisticated theoretical treatment clear.

1.5 The Phenomenology of Bauer, Stech, and Wirbel

A phenomenological approach to two body decays of D mesons has been developed by Stech and collaborators (Bauer-Stech[Ba85], Fakirov-Stech[Fa78], and Bauer-Stech-Wirbel[Ba87)]). Their recipe starts by ignoring WA interactions and by using an effective Lagrangian (equation 1.3) for the quark currents which includes the 1-gluon perturbative QCD corrections.

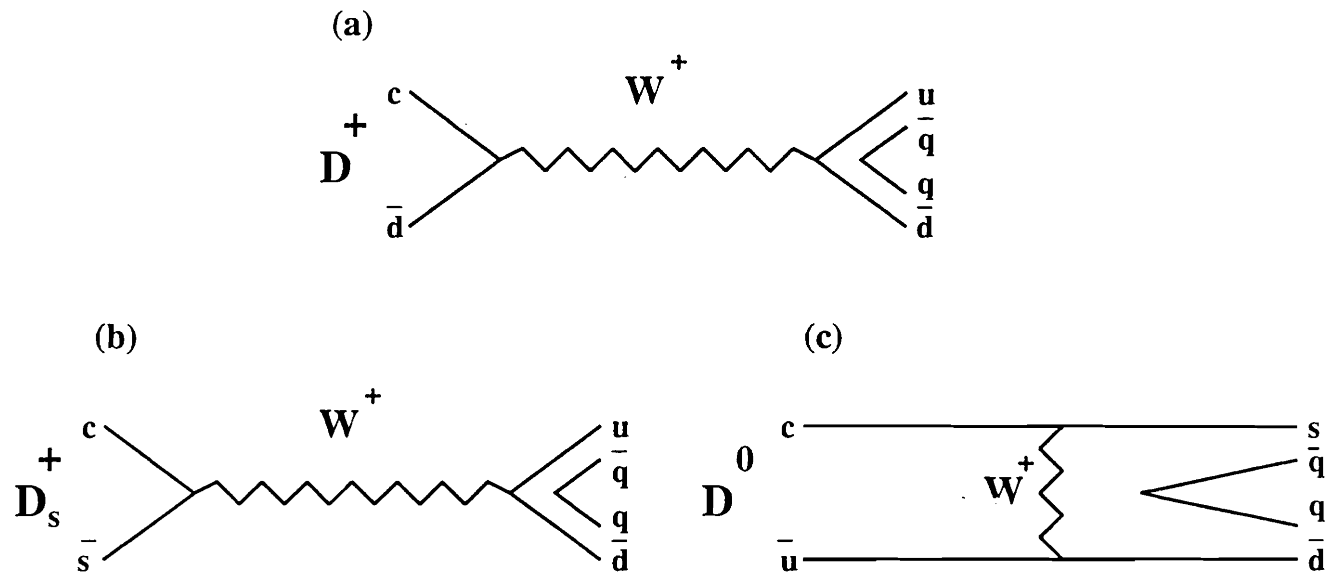

Figure 1.3: WA Diagrams: (a) of the D^+, (b) of the D_s^+, and (c) of the D^0

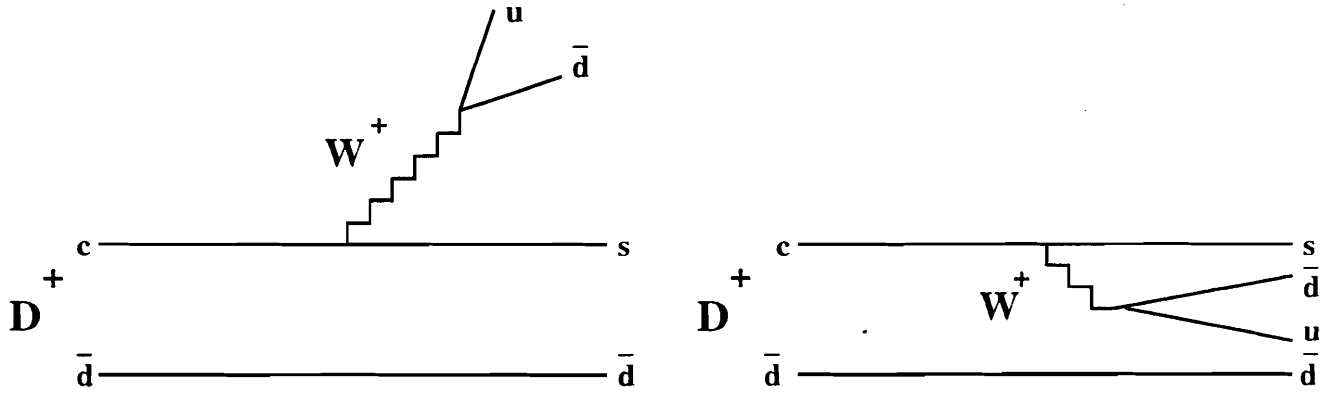

Figure 1.4: D^+ spectator decay diagram and the diagram obtained by exchange of identical $\overline{d}$ quarks

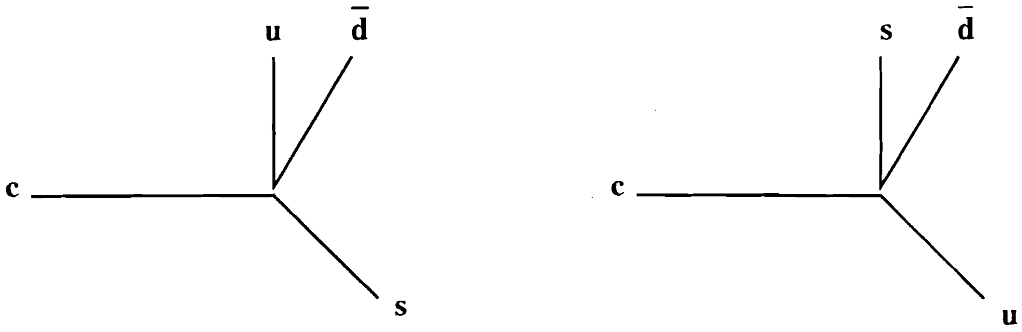

(a) (b)

Figure 1.5: The Effective Lagrangian, (a) Charged Current and (b) Neutral Current

$$L_{eff} \propto \frac{c_+ + c_-}{2} \bar{s}_L \gamma_\mu c_L \bar{u}_L \gamma^\mu d_L + \frac{c_+ - c_-}{2} \bar{u}_L \gamma_\mu c_L \bar{s}_L \gamma^\mu d_L \qquad (1.3)$$

Where the $c_\pm$ are calculated from perturbative QCD. This first term of this effective Lagrangian is the usual standard model charged current (figure 1.5(a)). The second term is an effective neutral current (figure 1.5(b)).

One then writes down the transition amplitude (equation 1.4).

$$T(D \to f) \propto a_1 \langle f \mid \bar{s}_L \gamma_\mu c_L \bar{u}_L \gamma^\mu d_L \mid D \rangle + a_2 \langle f \mid \bar{u}_L \gamma_\mu c_L \bar{s}_L \gamma^\mu d_L \mid D \rangle \qquad (1.4)$$

where

$$a_1 = \frac{1}{2}(c_+ + c_-) + \frac{\xi}{2}(c_+ - c_-)$$

$$a_2 = \frac{1}{2}(c_+ - c_-) + \frac{\xi}{2}(c_+ + c_-)$$

An extra parameter ξ is introduced to take into the account the effects of color matching in hadrons. Finally for two body decays a factorization ansatz is made. That is for two particles A and B in the final state [Bi88a].

$$\langle f \mid J_\mu J^\mu \mid D\rangle = \langle A, B \mid J_\mu \mid 0\rangle\langle A, B \mid J^\mu \mid D\rangle$$

Using this model predictions about the two body decays of charm mesons can be made. The charged current term gives rise to $D^0 \rightarrow M_1^{\pm} M_2^{\mp}$ and $D^+ \rightarrow M_1^+ M_2^0$ decays (figure 1.6), while the neutral current term is responsible for $D^0 \rightarrow M_1^0 M_2^0$ and $D^+ \rightarrow M_1^+ M_2^0$ decay (figure 1.7).

Therefore, there are three classes of transitions about which BSW make predictions. Class I are of the form $D^0 \rightarrow M_1^{\pm} M_2^{\mp}$ and are proportional to a_1. Class II are of the form $D^0 \rightarrow M_1^0 M_2^0$ and are proportional to a_2. Class III are of the form $D^+ \rightarrow M_1^+ M_2^0$ are are proportional to $a_1 + (1 + \alpha)a_2$ (α is generally positive). The experimental values for a_1 and a_2 were obtained by fitting to MARK III data [Bi88a].

$$a_1 \simeq 1.2 \pm .1 \qquad\qquad a_2 \simeq -.5 \pm .1$$

Since a_2 is negative, the BSW model predicts destructive interference and hence smaller partial widths in D^+ decays. Therefore, BSW predict $\frac{\tau_{D^+}}{\tau_{D^0}} > 1$. In general, as Table 1.1 shows, the BSW model seems to do reasonably well for Cabibbo allowed decays.

The model is known to do even better for B meson decays where the factorization ansatz is expected to work very well. For B decays $|a_1| \approx 1.15$ and $|a_2| \approx 0.26$ [Ya93].

1.6 Doubly Cabibbo Suppressed Decays of the D^+

In the roughest approximation, the rate of doubly Cabibbo suppressed decays should be suppressed by a factor of $\tan^4 \theta_c \sim 3 \times 10^{-3}$. However, it has been argued in the previous sections that the relatively long lifetime of the D^+ is due to

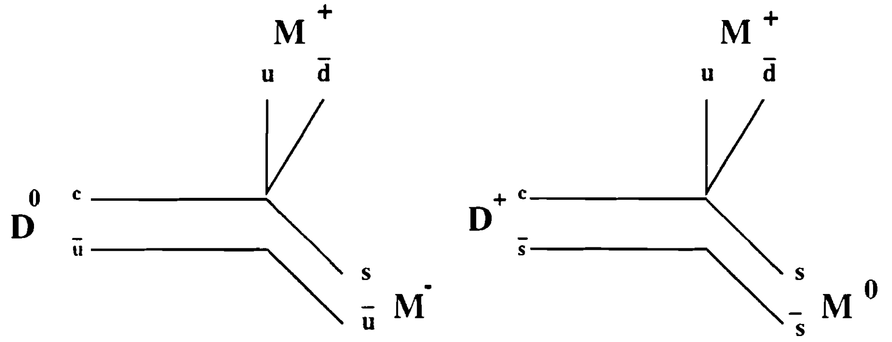

(a) (b)

Figure 1.6: Decays mediated by the effective charged current

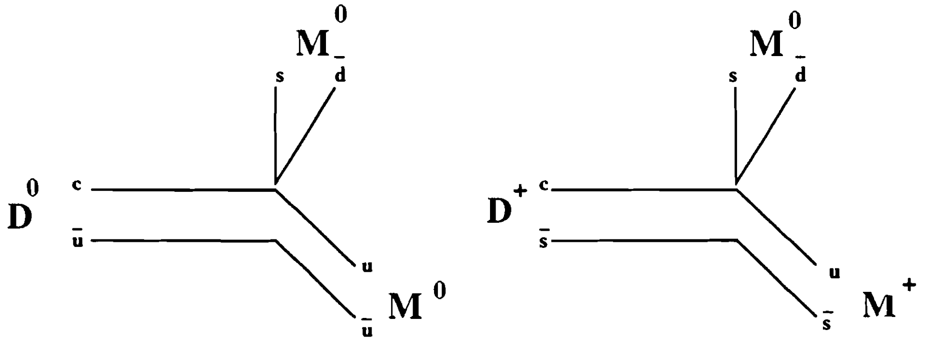

(a) (b)

Figure 1.7: Decays mediated by the effective neutral current

destructive interference possibly resulting from the presence of identical quarks in the final state. Doubly Cabibbo suppressed decays of the D^+ have no such problem (figure 1.8). Therefore, naively one would expect the parameter ρ (equation 1.5) to be greater than 1.

$$\rho = \frac{A(D^+ \to DCSD)}{A(D^+ \to CFD)} \times \frac{1}{\tan^2 \theta_c} \tag{1.5}$$

Bigi has applied the BSW formalism to calculate $\mid \rho \mid^2$ for two body doubly Cabibbo suppressed decays of the D^+ [Bi88b].

$$\mid \rho_{K^+\pi^0} \mid^2 = \frac{Br(D^+ \to K^+\pi^0)}{Br(D^+ \to \overline{K}^0\pi^+)} \times \frac{1}{\tan^4 \theta_c} \sim 3$$

$$\mid \rho_{K^{*0}\pi^+} \mid^2 = \frac{Br(D^+ \to K^{*0}\pi^+)}{Br(D^+ \to \overline{K}^{*0}\pi^+)} \times \frac{1}{\tan^4 \theta_c} \sim 5 - 11$$

$$\mid \rho_{K^{*+}\pi^0} \mid^2 = \frac{Br(D^+ \to K^{*+}\pi^0)}{Br(D^+ \to \overline{K}^{*0}\pi^+)} \times \frac{1}{\tan^4 \theta_c} \sim 12 - 25$$

$$\mid \rho_{K^+\rho^0} \mid^2 = \frac{Br(D^+ \to K^+\rho^0)}{Br(D^+ \to \overline{K}^0\rho^+)} \times \frac{1}{\tan^4 \theta_c} \sim .35$$

Both the numerator and the denominator are from theory. The enhancements of the DCSDs over the Cabibbo favored modes are as large as 25. DCSDs with such large enhancements would be striking signals in our data.

This thesis will present the results of a high sensitivity search for DCSDs of the D^+ into charged daughters. The data are from Fermilab experiment E791, a fixed target experiment in the proton beam line. Our experiment used an open trigger in order to record most pion-nucleon interactions.

$$\pi^- + N \to X$$

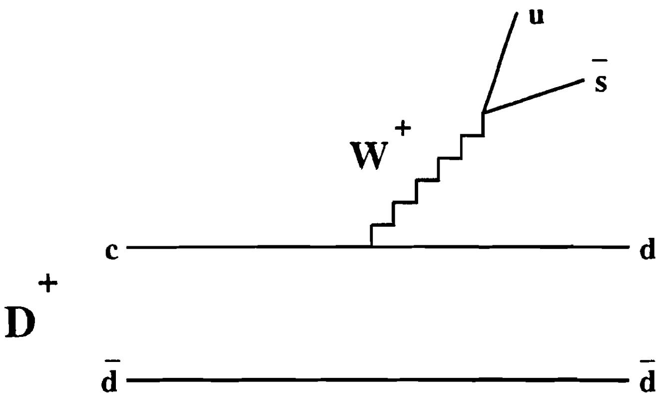

Figure 1.8: Doubly Cabibbo suppressed decay of the D^+

The 20 billion triggers taken in E791 contain approximately 200,000 fully reconstructed charm. This makes our data the highest statistics sample in the world.

Table 1.1: BSW predictions vs Experiment [La92]

Class I:	Experiment	BSW	BSW[a]
$D^0 \rightarrow K^-\pi^+$	$4.2 \pm .4 \pm .4$	6.0	4.7
$D^0 \rightarrow K^-\rho^+$	$10.8 \pm .4 \pm 1.7$	11	11
$D^0 \rightarrow K^{*-}\pi^+$	$5.3 \pm .4 \pm 1.0$	3.1	2.8
$D^0 \rightarrow K^{*-}\rho^+$	$6.2 \pm 2.3 \pm 2.0$	21	17
Class II:			
$D^0 \rightarrow \overline{K}^0\pi^0$	$1.9 \pm .4 \pm 1.7$	.8	.21
$D^0 \rightarrow \overline{K}^0\rho^0$	$.8 \pm .1 \pm .5$	.3	.3
$D^0 \rightarrow \overline{K}^{*0}\pi^0$	$2.6 \pm .3 \pm .7$	1.0	1.3
$D^0 \rightarrow \overline{K}^{*0}\rho^0$	$1.9 \pm .3 \pm .7$	1.9	5.8
Class III:			
$D^+ \rightarrow \overline{K}^0\pi^+$	$3.2 \pm .5 \pm .2$	3.6	3.6
$D^+ \rightarrow \overline{K}^0\rho^+$	$6.9 \pm .8 \pm 2.3$	15.1	15.1
$D^+ \rightarrow \overline{K}^{*0}\pi^+$	$5.9 \pm 1.9 \pm 2.5$	.3	.3
$D^+ \rightarrow \overline{K}^{*0}\rho^+$	$4.8 \pm 1.2 \pm 1.4$	17	17

[a] Corrected for Isospin phase shifts.

Chapter 2

The Beam Line

2.1 The Proton East Area Beamline

The charm particles in our experiment were produced by colliding a π^- beam on platinum and carbon fixed targets. The source of the π^-'s was ultimately the 900 GeV Tevatron proton beam. Protons were extracted from the Tevatron and split into Proton, Meson, and Neutrino beamlines. The proton beam line was further subdivided into PEAST, PCENTER, and PWEST beamlines. Our experiment was located on the PEAST beamline.

The PEAST beamline is represented schematically in figures 2.1 and 2.2. The prisms are shorthand for dipole magnets. The convex and concave lenses represent respectively focusing and defocusing quadrupole magnets.

As shown in figure 2.1, Protons in PEAST were transported down the beamline and focused on a 30cm beryllium target where the secondary π^-'s were created. The π^-'s were then selected by choosing the dipole magnet's field strength and polarity so that particles of the appropriate momentum and charge would pass through the collimators. Then the π^-'s, as shown in figure 2.2, were further focused and eventually directed into our experiment and onto our experimental target.

PEAST received 2×10^{12} protons per 22 second spill on average. This resulted in about 10^7 500 GeV π^-'s incident on our experimental target per spill and about 200,000 events recorded per spill.

2.2 Target Configuration

Our target (figure 2.3) was a platinum cylinder of 1 cm diameter and 0.156 cm thickness, followed by four carbon cylinders of 1 cm diameter and 0.156 cm thickness. The target cylinders were mounted in lexan and separated by about 1.6 cm. This spacing was chosen so that secondary vertices could be fully resolved between targets. The series of 5 targets was approximately 2.5 % of a interaction length. This target assembly was mounted just upstream of the first vertex silicon detector.

Figure 2.4 shows the reconstructed Z positions of primary vertices (interactions in our target foils) in our experiment. The actual distribution of the Z position for each foil is a convolution of a top hat function (representing the physical extension of the foil) and a Gaussian (representing the vertex resolution). The σ of the resolution is plotted next to each foil. E791 has a primary vertex resolution in Z of between 250 and 450 microns. Note the peak in the plot at Z= 0 is our experimental interaction counter.

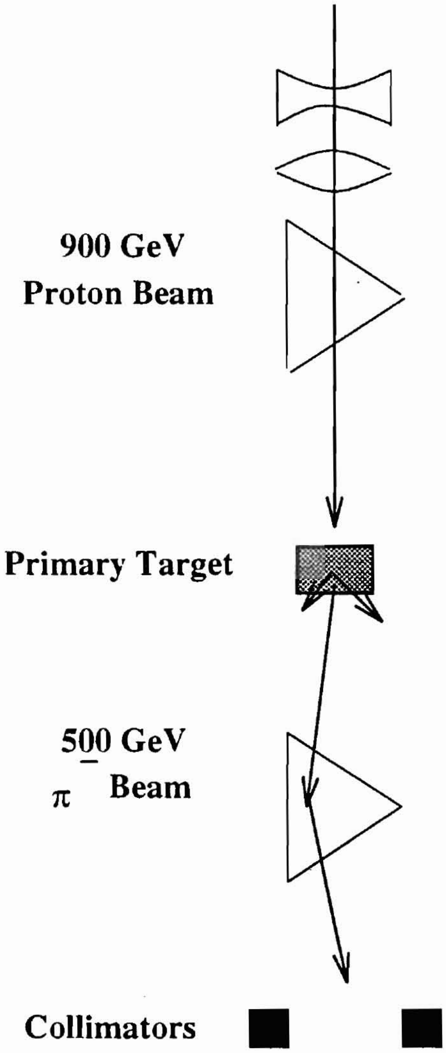

Figure 2.1: The Proton EAST Beamline

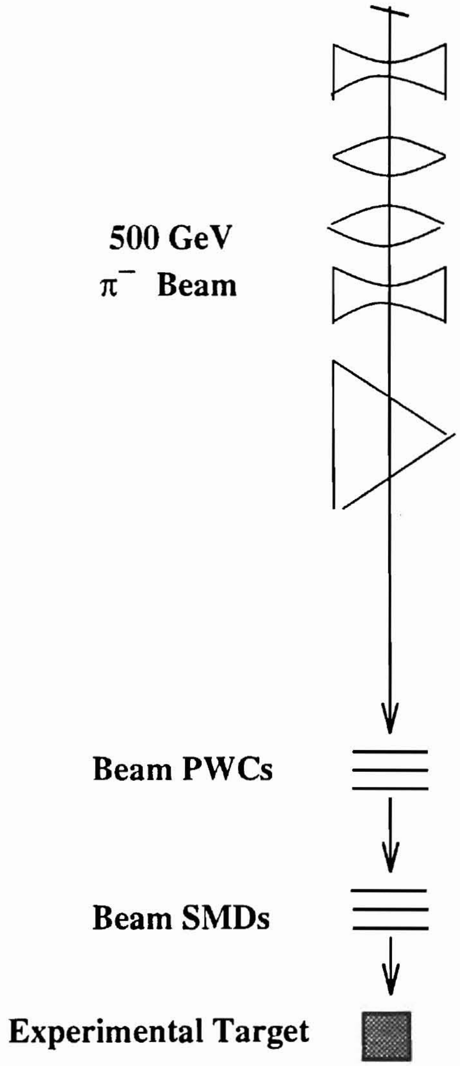

Figure 2.2: The Proton EAST Beamline, continued.

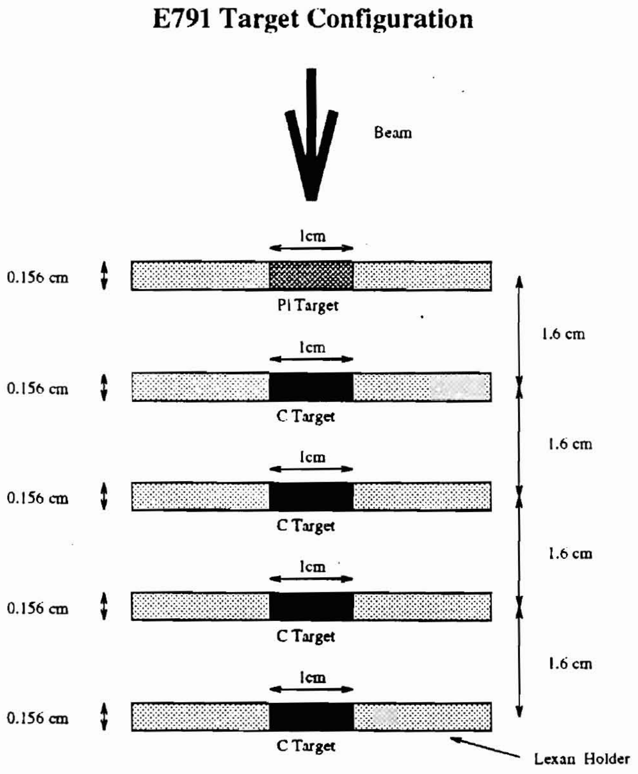

Figure 2.3: E791 Target Configuration

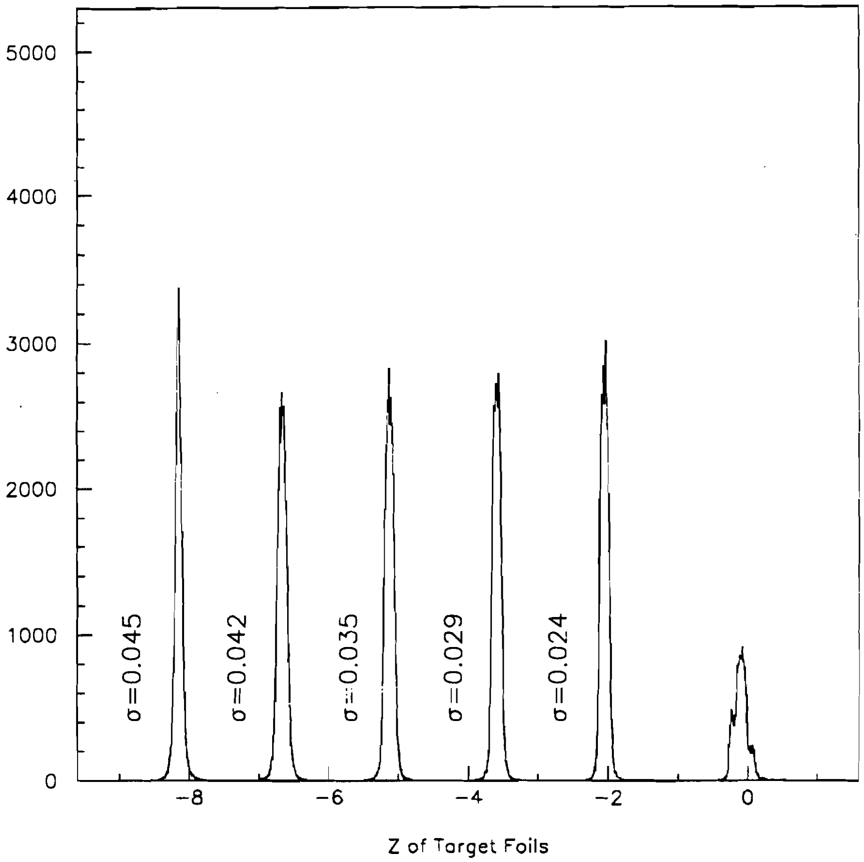

Figure 2.4: Reconstructed Primary Vertices

Chapter 3

The E791 Spectrometer

3.1 Introduction

The Tagged Photon Spectrometer (tagged photons are not used in our experiment, the name is historical) is a two magnet spectrometer. It has twenty three silicon microstrip detectors for high resolution vertexing and beam tracking, thirty five drift chambers for momentum determination, two Čerenkov counters for charged particle identification, an electromagnetic shower calorimeter to detect electrons and photons, a hadronic calorimeter to detect neutral hadrons, and two muon walls.

There were several important upgrades of the Tagged Photon Spectrometer, since the time it was used in E769. More silicon planes were added to both the beam and vertex assemblies for better resolution and tracking efficiency. New readout systems were constructed for all of our detectors in order to meet the specifications of our faster data acquisition system. Finally, a completely new muon Y wall (to measure the Y position of muon tracks) was constructed for E791. The detector is displayed in figure 3.1.

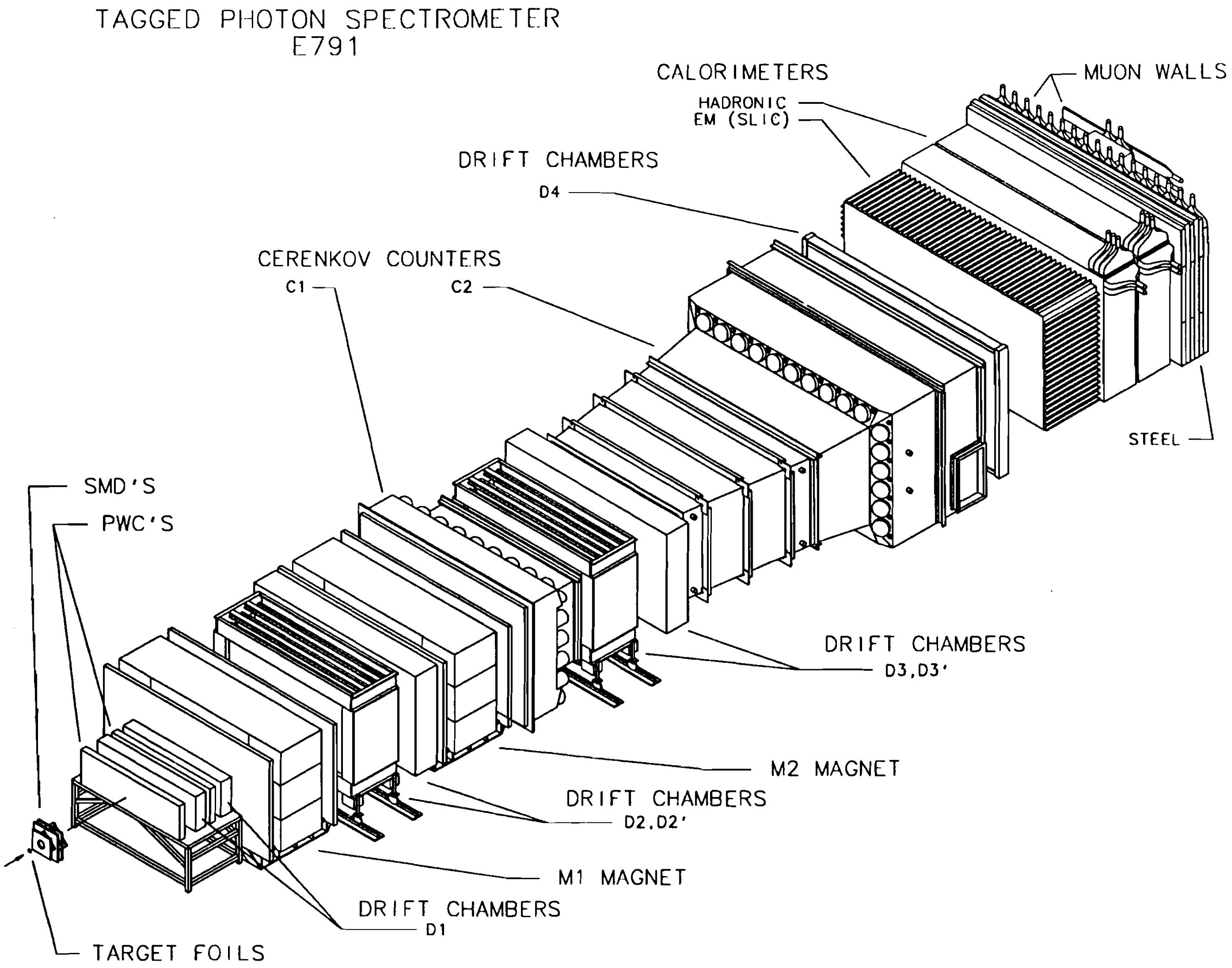

Figure 3.1: The E791 Spectrometer

3.2 The Proportional Wire Chambers

A series of Proportional Wire Chambers consisting of evenly spaced field and sense wires suspended in an Argon, CO_2, and Freon mixture were used for charged particle tracking. In a manner similar to the Drift Chambers (which are described later in the chapter) the charged particles ionize gas molecules and the free electrons are forced to migrate to the sense wire by the electric field set up by the field wires. In regions of high electric field the electron signal becomes amplified as electrons already liberated ionize other molecules. The peak of this signal, determining which sense wire was "hit", is collected within 4 ns.

E791 possessed 8 upstream PWCs for beam tracking with a wire spacing of 1 mm and two downstream PWCs for tracking with a wire spacing of 2mm. Since no time information about the sensed signals was recorded (unlike the drift chambers) the resolution of these detectors was simply the wire spacing divided by $\sqrt{12}$.

3.3 The Silicon Microstrip Detectors

E791's silicon system consists of twenty three planes of silicon microstrip detectors, six planes for beam tracking and seventeen for vertex reconstruction (see Figure 3.2). The angular acceptance of the vertex system is $\approx \pm 200$ mrad and the per plane efficiency was roughly 90 % with about 0.1 % noise.

The silicon microstrip detectors are the heart of the E791 spectrometer. Their ability to separate secondary from primary vertexes substantially reduces our background. A longitudinal resolution of $\sigma_z \approx 400$ microns allows us to make a vertex separation cut of six standard deviations without substantial losses in signal. This resolution also translates into a time resolution of 0.04 ps for a typical D meson in

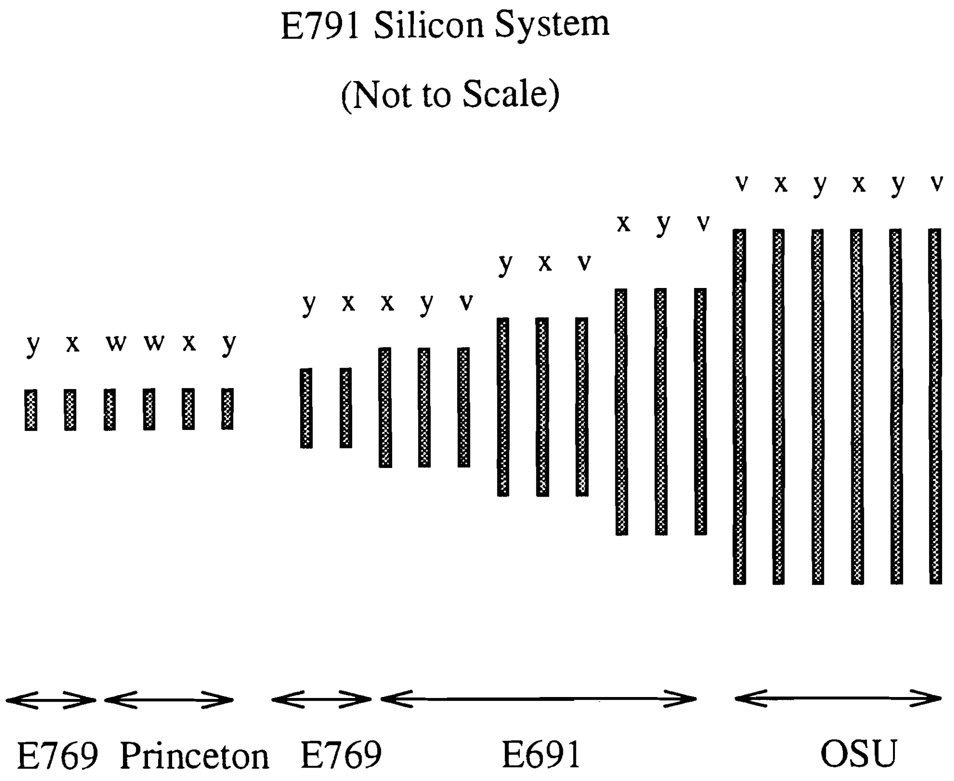

Figure 3.2: The E791 Silicon System

our experiment. Since the characteristic lifetime is of order 1 ps this permits us to investigate the time evolution of the decays.

3.3.1 The E691 Silicon Detectors

The E691 silicon microstrip detectors are called such because they are a group of three X-Y-V detector triplets inherited from experiment E691.

These silicon wafers were about 300 microns thick and were ion implanted on both sides. P-type strips were formed by implanting boron in nearly 50 micron wide strips of silicon spaced 50 microns apart. A layer of aluminum was deposited over the boron doped silicon to serve as an ohmic contact. The opposite side of the wafer was doped with a continuous n-layer of arsenic. Aluminum was deposited over the arsenic for a good ohmic contact. The resulting p-i-n junction diodes were

Table 3.1: E691 Silicon Detectors summary

	Triplet 1	Triplet 2	Triplet 3
area (mm^2)	676	2500	2500
strip spacing (μm)	50	50	50
instrumented strips	512	768	1000

reverse biased at 90 volts.

A charged particle that traversed the silicon strips caused on average 23,000 electron-hole pairs to be excited into the conduction band. Signals the size of 3.5 femtocoulombs were too small to travel more than about a meter without amplification. So they were fanned out on circuits printed in copper, on Kapton tape and G10 to preamplifiers. The first E691 triplet consisted of smaller (676 mm^2) Enertec built wafers and the second and third triplets of larger (2500 mm^2) Micron detectors. The fan-outs for the Enertec detectors were made entirely of Kapton, while the fan-outs for the Micron detectors were made of G10 with Kapton edges for flexibility.

The detectors and fan-outs were mounted as triplets inside light tight rf boxes. Mounted on the rf boxes were 9.5cm long, 3.0cm wide, 3.5 cm deep preamplifier cages. The cages were made of silver plated aluminum for good rf shielding and each contained 32 four-channel Laben MSD2 preamplifier cards. Each amplifier channel had a current gain of 200 and a rise time of 3 nanoseconds. The preamp signals were transmitted to discriminator cards over 4m long flat shielded nine-channel cables, four channels were for signal and five for ground. The cables were shielded with aluminum foil grounded to the detector ground. The discriminators were slightly modified eight-channel Nanosystems' MWPC discriminator cards models S710/810. Appropriate groups of the discriminator cards stacked in cages were read out as one contiguous shift register by the SMD scanners.

3.3.2 The E769 Silicon Detectors

The E769 silicon microstrip detectors were a series of four detectors ,two in the X view and two in the Y view, added to the Tagged Photon Spectrometer during E769. Two of the detectors (an X view and a Y view detector) were mounted upstream of the target in the beam SMD system. The other two were mounted just downstream of the target and were the most upstream of the vertex system SMDs.

The E769 detectors were constructed by Micron Semiconductor. The detectors were mounted in light tight RF boxes on copper plated G-10 with Kapton tape at the edges for flexibility. The beam E769 planes had the 384 strips of their inner region strips instrumented. The strips were of 25 micron pitch. The vertex E769 planes had 304 strips of 50 micron pitch in their wings instrumented, as well as the 384 inner strips.

The planes were fully depleted when reverse biased at 90V. The signals were amplified by 4-channel Laben MSP1 preamplifiers. These had differential outputs in order to lower common mode noise. The signals were fanned out to 8-channel Nanosystem 5710/810 amplifier-discriminator cards. The thresholds on the discriminator cards were adjusted to 40 % of the average pulse height created by a minimum ionizing particle. The discriminators in each box were chained together serially and read out as a large shift register.

The E769 vertex planes were the closest planes to the target. Because of this and their finely pitched inner region they had the potential to greatly improve our vertexing resolution. Unfortunately, their discriminator cards proved to be too noisy to make the planes more than adequate.

Table 3.2: E769 Silicon Detectors summary

	Beam	Vertex
area (mm^2)	100	256
strip spacing (μm)	25	25/50
instrumented strips	384	688

3.3.3 The OSU Silicon Detectors

Ohio State University added six silicon detectors to the Tagged Photon spectrometer for the 1991-92 run of E791. The detectors were cannibalized from experiment E653. As the largest silicon detectors they were located the furthest downstream and greatly improved the acceptance and tracking efficiency of our vertex silicon system.

The detectors consisted of two X-Y-V triplets. Each detector had an inner region of 50 micron pitch strips and an outer region of 200 micron pitch strips. Each detector had 864 instrumented strips.

The detectors were fully depleted at 60V of reverse bias.

3.3.4 The Princeton Silicon Detectors

Princeton University added four new silicon planes to the TPL spectrometer's beam silicon system. Beam tracking improves the accuracy of the primary vertex reconstruction and the additional X, Y, and two W (30° with respect to X) planes greatly improved the efficiency and accuracy of beam tracking.

The Princeton planes were mounted in light tight rf boxes downstream of the existing E769 beam SMDs on the existing beam SMD assembly. The two W planes were placed in separate boxes and the X and Y plane were grouped in another box. On the exterior edges of the rf boxes copper cages were mounted for the preamplifier cards. The wafers in the Princeton Silicon Detectors were 300 μm thick. They had 384 inner strips of 25 μm pitch and 304 outer strips of 50 μm pitch. All of the inner strips were instrumented in all planes. The X and Y planes each had 32 of the outer strips instrumented (16 on each side of the wafer) and each W plane had 64 of the outer strips instrumented (32 on each side of the wafer).

The planes were reverse biased at 70 volts and the signals that resulted when a beam particled traversed a silicon strip were fanned out on circuits printed on Kapton tape to MSP1 preamplifiers. The signals from the preamps were sent over twisted pair ribbon cables to eight-channel Nanometric N339A amplifier-discriminator cards. A crate containing up to 28 of these discriminator cards was read out as one large shift register by the SMD scanners.

3.3.5 The Princeton SMD Scanners (Adapted from $[Pu90]$

)

The approximately 16,000 silicon detector channels described above had to be read out and their information had to be packaged in an usuable format in roughly 20 microseconds. To accomplish this task a specialized SMD readout was built.

The SMD scanners performed this task by reading out approximately 80 sets of 200 silicon strips in parallel. Each Scanner board contained eight individual scanners capable of reading out 256 strips as one large shift register. Exiting each scanner was a CLK OUT cable and entering each scanner was a CLK IN and DATA cable. The scanners sent clocks to the shift registers (groups of amplifier / discriminator cards attached directly to SMD channels) in the experimental hall. Clocks were returned to the scanners with SMD hits represented as high signals on the DATA line in time with the clock number corresponding to that channel in the shift register.

Table 3.3: Magnet Parameters Summary (Adapted from [Ra87])

Magnet	M1	M2
center (cm)	273.5	617.7
length (cm)	165	208
entrance aperture (cm^2)	154 × 73	154 × 69
exit aperture (cm^2)	183 × 91	183 × 86
current (amps)	2500	1800
p_T kick	0.212 GeV	0.320 GeV
$\int Bdl$	-0.71 T-m	-1.07 T-m

The scanner boards themselves were operated in VME crates. Each crate contained at most 8 scanner boards and a controller board. The controller read out all the scanners in its own crate. It then formatted the data and shipped it out to the event FIFO buffer.

3.4 The Magnets

E791 used two large aperture dipole magnets to reconstruct the momentum of charged particle tracks. The upstream magnet M1 was run with a current of 2500 amps which resulted in a P_t kick of 0.212 GeV/c and the downstream magnet M2 was run with a current of 1800 amps which resulted in a P_t kick of 0.320 GeV/c (there are 4 coils in M2 as opposed to 2 in M1 hence a larger kick with a lower current).

The B fields in the dipole approximation pointed in the y (up-down) direction. The total deflection angle of the charged particle track was given by

$$\theta \simeq \frac{\int Bdl}{3.33p}$$

[Fe86]. So

$$\frac{\delta p}{p} = \frac{\delta \theta}{\theta}$$

and since the magnets bend in x

$$\delta \theta = \frac{\delta x}{r}$$

and finally

$$\frac{\delta p}{p} = \frac{3.33(\delta x)p}{r \int Bdl}$$

where r is the lever arm to the drift chambers. Good momentum resolution therefore requires good x position resolution, a long lever arm and a large $\int Bdl$. The spectrometer was designed with all these parameters in mind.

For reconstruction it was determined that the requisite accuracy could be obtained by using a single bend plane approximation instead of a more detailed field map and parameterization. An entire magnet is approximated as imparting a P_t kick in a single bend plane. For M1 the bend was at 274.2 cm in the experimental coordinate system and the kick was measured to be 0.212 GeV and for M2 the bend was at 621.1 cm and the kick was 0.320 GeV.

3.5 The Drift Chambers

The TPL spectrometer used thirty five drift chamber planes for downstream tracking and momentum analysis. The spectrometer had three flavours of sense planes. X planes in which the wires were hung vertically, U planes which had its wires woven at a 20.5° angle with respect to the X planes (but the same rectangular aperture) , and V planes which had its wires rotated -20.5° with respect to X (but again with the same rectangular aperture as the X planes). No sense planes directly measured the Y coordinate since sense wires hung horizontally would have too much sag for accurate measurement.

The drift chambers were separated into four different subsystems. D1 was a group of eight sense planes (four X, two U, and two V) located downstream of the SMDs and the downstream PWCs and upstream of M1. D1 was used to increase the acceptance of the region one tracking. Between M1 and M2 was a group of four X,U,V detector triplets D2 which was used to measure a particle's deflection by M1. Similarly the third drift chamber, D3, another set of four X,U,V detector triplets, was placed downstream of M2 to measure the deflection caused by M2. Finally, a single triplet of sense planes D4, was located just upstream of the calorimeters. Unfortunately, despite its long lever arm D4 was of limited use in reconstruction because of its poor resolution.

The drift chamber assemblies consisted of alternating sense and high-voltage planes in gas tight rf boxes. In turn, the sense planes' wires alternated between field shaping and sense wires. For D1, D2, and D3 the high-voltage planes were held at -2.1kV to -2.6kV and the field shaping wire 0.4kV to 0.6kV higher. This forced liberated electrons to drift toward the grounded sense wires. D4 had its high-voltage planes at ground, a small positive high-voltage on its field shaping wires, and a large positive high-voltage on its sense wires. From the drift time the distance of the particle's trajectory from the sense wire could be determined by the relation $d = \Delta t\, v_d$, where v_d was the electron's drift velocity.

A chamber's drift velocity is determined by the gas used and the electric field. For E791 we used a mixture of argon (90 %), CO_2 (10 %), and a fraction of CF_4 (1 %). The chambers were operated with electric fields in the plateau region. This prevents small changes in voltages from altering the drift velocity and hence

Table 3.4: Drift Chamber Parameters Adapted From [Ra87, Th94]

	D1	D2	D3	D4
physical size (X $\times$ Y cm^2)	126 $\times$ 71	285 $\times$ 143	323 $\times$ 143	511 $\times$ 259
# of Planes	8	12	12	3
# of channels	1536	2400	1952	416
X cell size (cm)	0.476	0.953	1.588	3.18
resolution (μm)	400	300	300	450

degrading the spatial resolution. Although some non-linearities existed and we corrected for them. The gas and field strength in our detectors resulted in a drift velocity of 50 μm/ns.

The signals from the sense wire were read out with Lecroy DC201 Nanomaker N-277C amplifier/discriminators. Twisted pair cables transmitted the signals to the Fastbus based Philips 10C6 TDCs which were read out by Fastbus Smart Crate Controllers to the DA system.

The TDCs were operated in the common stop mode. Meaning the the trigger was delayed and stopped the counting of all channels at the same time. This clearly was not the drift time of the electrons. Therefore, a calibration procedure was needed to determine the drift time given this raw Δt for each sense wire. The raw Δt for each sense wire was decomposed into three parts.

$$\Delta t = Constant - (t_{abs} + t_{rel} + t_{drift})$$

The absolute time offset, t_{abs}, was due to the fact that the drift chambers were downstream of the trigger paddles and due to detector offsets. Therefore, charged particles arrived at the chambers a constant time after the detector was triggered. The relative time offsets, t_{rel}, resulted from differences in cable lengths and electronic responses for each sense wire channel. These relative offsets were measured by pulsing individual sense wire channels. A standard programmable timing generator was used to generate both the signal for the sense wires and later the stop for the TDCs as well as opening the gate to the TDCs. The offsets were averaged for all channels in a plane, and then the differences from the averages were loaded into the pedestal memories in the TDCs. These relative offsets were redone when we changed discriminator cards. These relative time offsets were automatically subtracted from the TDC count.

The TDC counts after this subtraction involved only the electron's drift time and the absolute time offset. The absolute t_0s and other drift chamber alignment parameters were determined by doing offline tracking studies. Data from muon calibration runs, where clean muons tracks traverse the drift chambers in the absence of a magnetic field were used for the first pass of the alignment. For the final iterations, reconstruction of E_t data with the magnets on was used.

3.6 The Čerenkov Counters

Charged particles traveling faster than the speed of light in the medium they are traversing, radiate light (the Čerenkov effect). We used the Čerenkov effect to identify electrons, muons, pions, kaons, and protons. The number of photons N emitted per unit wavelength per unit length is [Fe86]

$$\frac{dN}{dl d\lambda} = \frac{2\pi\alpha}{\lambda^2}(1 - \frac{p_{th}^2}{p^2})$$

and

$$p_{th} \simeq \frac{mc}{\sqrt{2(n-1)}}$$

where n is the refractive index of the medium. Therefore, given an index of refraction, a momentum measurement, and a mass hypothesis an amount of Čerenkov light can be predicted. This information when combined with the measured amount of Čerenkov light can be used to form a probability of the correctness of the mass hypothesis.

E791 used two gas radiator Čerenkov counters for charged particle mass identification. They are illustrated in figure 3.3 C1, the upstream counter, was located just downstream of M2, partially inset in the magnet because of space constraints, and C2 was placed between D3 and D4. The Čerenkov counters had different gas mixtures with different indices of refraction, in order to identify the particle's masses in different momentum ranges. C1 had an assembly of twenty-eight mirrors and C2 had thirty-two mirrors to reflect light into the Winston cones and onto the phototubes' photocathodes. The sizes of the mirrors ranged between 300 cm^2 and 6,650 cm^2 in area, with the smaller mirrors placed in the centers of the detectors for greater segmentation in the region of greater particle density. C1 employed two bounce optics because of space constraints. That is, Čerenkov light was reflected from the twenty-eight mirrors of the primary mirror plane onto a secondary mirror plane and then into the Winston cones. C2 had more straightforward optics in which light was reflected directly from the primary mirror plane into the Winston cones. The optics are illustrated in figure 3.4.

In order to efficiently collect Čerenkov light and to prevent stray light from being collected a conical surface structure called a Winston cone was used. Both Čerenkov counters used 20° Winston cones. Which meant that light incident on a Winston cone with less than a 20° angle of incidence reached the photocathode in one reflection or less and light incident at greater than 20° would be eventually reflected out of the entrance aperture after multiple bounces. The collected light was detected

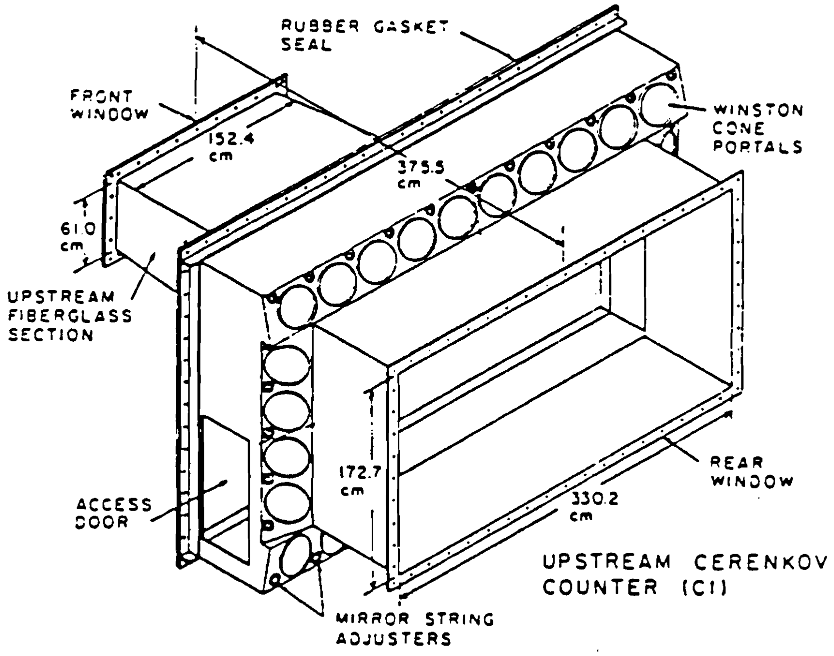

UPSTREAM CERENKOV COUNTER (C1)

DOWNSTREAM CERENKOV COUNTER (C2)

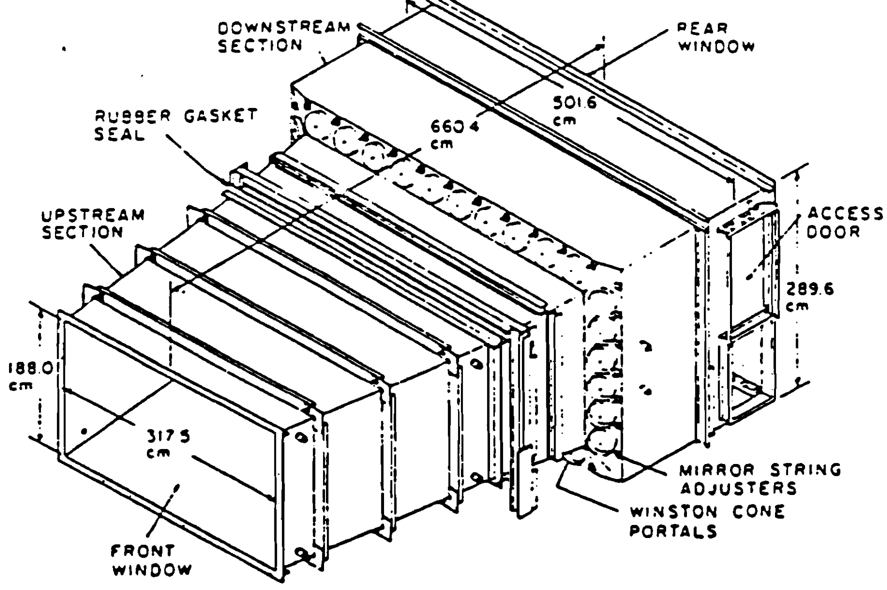

Figure 3.3: The Čerenkov Counters

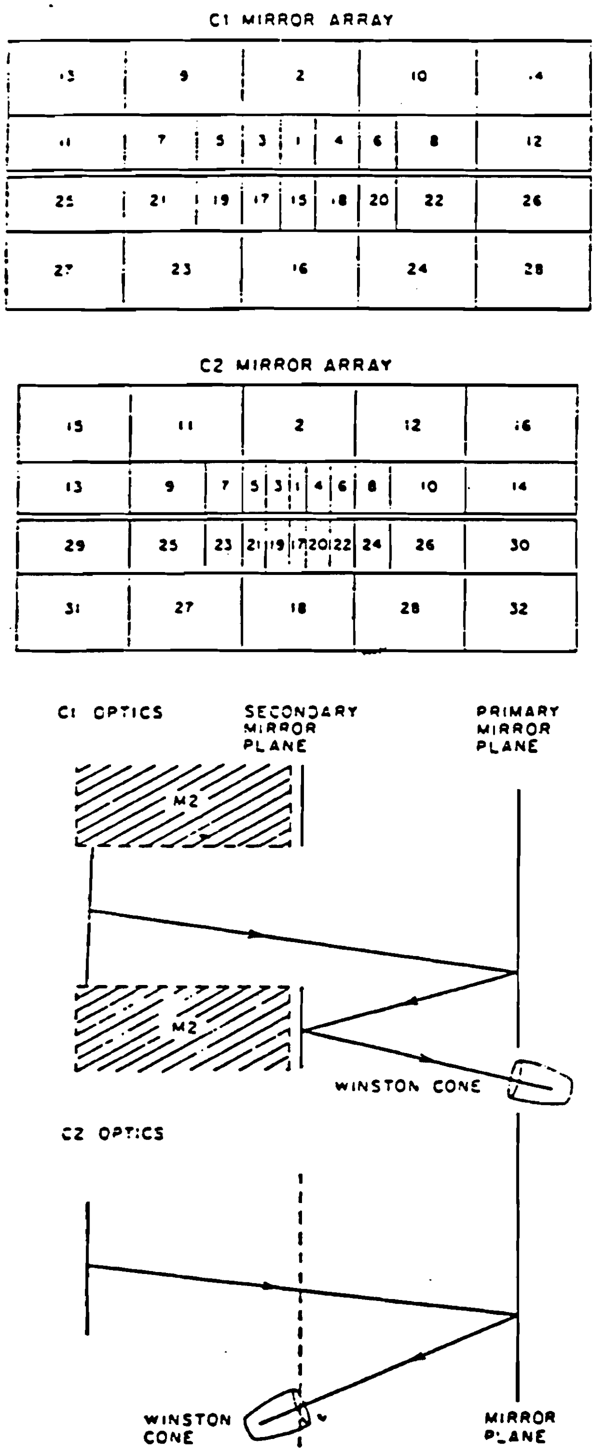

Figure 3.4: (a) Mirror Segmentation in C1 and C2 (b) Light Paths in C1 and C2

by RCA 8854 5 inch phototubes. Their very high gain cesiated gallium-phosphide first dynode produced an output signal linear in the number of photoelectrons. This linearity was essential to the accurate operation of the Čerenkov counters, since the counters were calibrated using the single photoelectron peak.

In order to calibrate each phototube it was necessary to know the average response of the phototube to a single photoelectron. The phototubes were illuminated with highly attenuated laser light. The output was digitized by LRS 2249 ADCs and a single electron photopeak was clearly visible. Since the double and triple photoelectron peaks were observed at the expected number of ADC counts (twice and three times, the singles peak minus the pedestal) the response of the phototubes was assumed to be linear. Therefore, the measured number of photoelectrons could be expressed in terms of the measured ADC counts.

$$N_{measured} = \frac{(ADC - PED)}{SPEP}$$

Where ADC is the raw ADC counts for that channel, the pedestal is the minimum ADC count observed in the spectrum, and SPEP is the number of ADC counts of the single photoelectron peak corrected for the pedestals.

The other component in the calibration of the Čerenkov counters was the efficiency of each mirror-cone-phototube unit. The efficiency was measured by observing the response of each unit to very high momentum isolated tracks whose Čerenkov light should be centered within a single mirror. The momentum of these tracks was above all thresholds in the regime where $\frac{dN}{dl}$ is nearly constant. Therefore, the predicted amount of light depended only on the path length of each unit. These measured efficiencies (or gains depending on your perspective) were then used along with $N_{measured}$ to reconstruct the light emitted by a track.

The Čerenkov probability reconstruction proceeded as follows. For each track

Table 3.5: Čerenkov Counters adapted from [Ra87]

	C1	C2
Length	3.7 m	6.6 m
# of Mirrors	28	32
Gas Mixture	N_2	80 % He - 20 % N_2

and mass hypothesis a Poisson distribution with the predicted amount of light as it's mean was formed. The probability of the hypothesis was then

$$pc_j = \frac{N_{pred}^{N_{meas}}}{N_{meas}!} e^{-N_{pred}}$$

Where j=1,2 refers to counters C1 and C2. A joint probability for each track and mass hypothesis was formed and the a priori mass probabilities were folded in to form the final Čerenkov probability, as per Bayes's theorem:

$$CPRB2(trk, i) = \frac{pc_1(trk, i) pc_2(trk, i) A(i)}{\sum_k pc_1(trk, k) pc_2(trk, k) A(k)}$$

where the As were the a priori probabilities (A(e) = 0.02, A(μ) = 0.01, A(π) =0 .81, A(K) = 0.12, and A(p) = 0.04) as measured in the experiment. This Čerenkov probability variable worked quite well in our analysis. For instance a cut on the Kaon probability just above the K/π/p indefinite peak was 80 % efficient for signal and reduced background by a factor of five in our more copious charm decays.

3.7 Calorimetry

The TPS contained both electromagnetic and hadronic calorimeters. These were used to both enhance the particle identification capabilities of the detector for charged tracks, and to identify possible photon and neutral hadron candidates.

Perhaps the most important use of the calorimetry was in our physics triggering. The majority of our experimental triggers were transverse energy, E_t, triggers. These triggers required that a certain amount of energy be present in the outer regions of the calorimeters in conjunction with the interaction counter being above threshold.

3.7.1 The SLIC

The Segmented Liquid Ionization Calorimeter (SLIC), was a large liquid scintillator calorimeter used to reconstruct electromagnetic showers from photons and electrons. The SLIC was used to discriminate the relatively narrow electron showers from the wider charged hadron showers. Also the photon showers from π^0's and η's were reconstructed in the SLIC.

Electrons in matter can emit bremsstrahlung and photons near nuclei may produce e^+ e^- pairs. These two processes are responsible for the propagation of electromagnetic showers. Electrons initially emit bremsstrahlung which in turn produce e^+ e^- pairs, which then emit bremsstrahlung and so on. While photons initially convert to e^+ e^- pairs which then emit bremsstrahlung etc. During the showering process photons and electrons lose energy to the scintillator via ionization and Compton scattering. This scintillation light is proportional to the energy of the incident particle.

The SLIC consisted of sixty scintillation layers. Each scintillation layer was made of corrugated aluminum and filled with a mineral oil based liquid scintillator (NE235H). The corrugations were 1.27 cm thick and 3.17 cm wide. The first layer had it s corrugations at an angle of 20.5° with respect to the vertical (the U view), the second layer's corrugations were at an angle of -20.5° with respect to the vertical (the V view), and the third scintillation layer's corrugations were horizontal (the Y view). The following layers were a repeat of this U, V, Y sequence. The SLIC contained 334 active channels, 109 U channels, 109 V channels, and 116 Y channels. Alternating between each scintillation layer were radiator sheets made of 0.63 cm of lead which was laminated on both sides with aluminum in order to prevent poisoning of the scintillator. Lead's high Z made it ideal for initiating and maintaining the showers. The construction of the SLIC is shown in figure 3.5.

The 3.17 cm wide corrugated channels of the scintillation layers were read out individually in the congested central region and in groups of two in the outer region. Each aluminum surface was coated with teflon (which has a lower index of refraction than the liquid scintillator), this made each SLIC channel a totally internally reflecting light pipe to light incident on the scintillator-teflon interface at less than about 20°. At one end of a channel was a mirror with a reflectivity of about 80 %. At the other end was a lucite window. Light exiting the window was collected by a waveshifter bar doped with BBQ. The ultraviolet light emitted by the scintillator was absorbed by the waveshifter and green light was remitted isotropically. The light was collected by a 2 inch RCA 4902 photomultiplier tube attached to the end of the waveshifter and converted into linear pulses. The pulses were digitized by Fast Encoding and Readout ADCs (FERAs).

The SLIC was calibrated during the run periodically using muon and electron runs.

The SLIC reconstruction algorithm consisted of two major parts, sector finding and particle candidate triplet finding. A search was made in each view for energy "cells", where a cell was defined as a cluster of counters above an energy threshold. Within each cell it was possible to have more than one particle and therefore the cells were subdivided into multiple sectors, when it appeared there were multiple peaks within a cell. It was also determined if a particular sector was associated

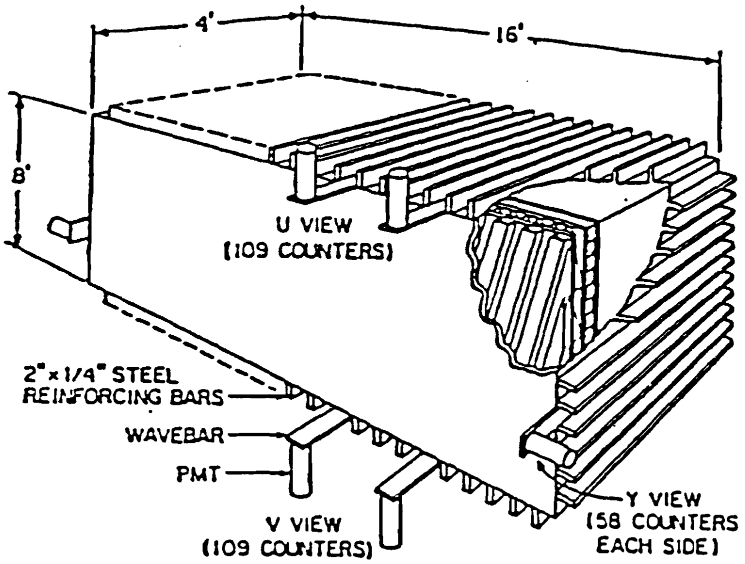

LEAD/LIQUID SCINTILLATOR SHOWER COUNTER (SLIC)
(SCHEMATIC)

Cutaway view of the SLIC.

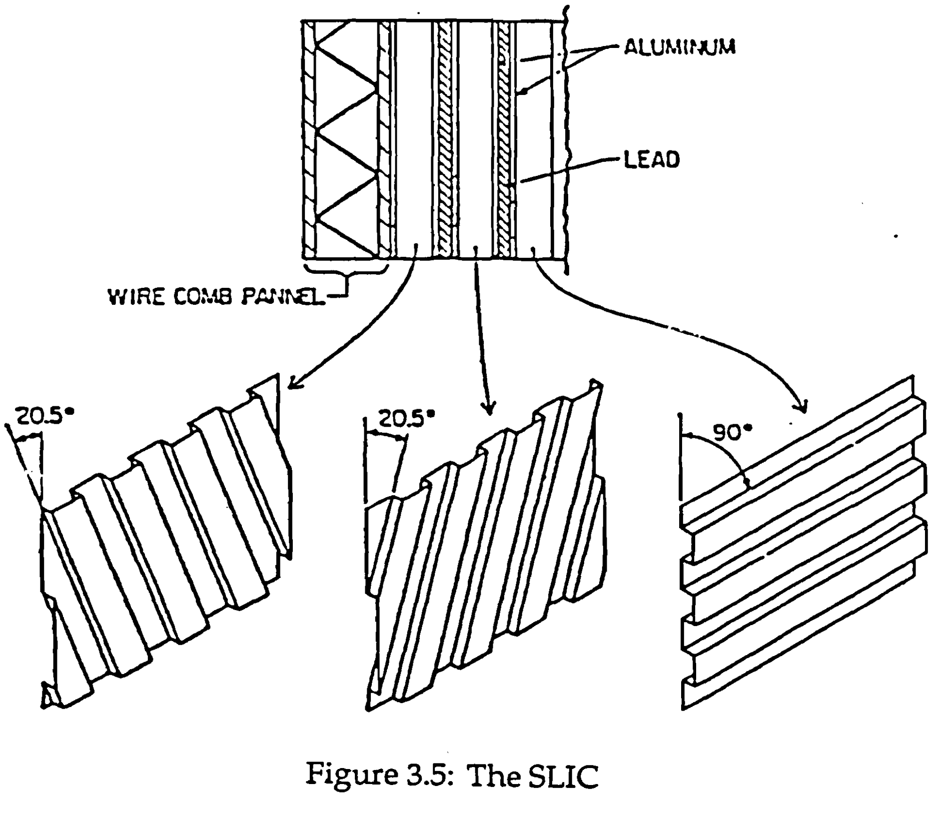

Figure 3.5: The SLIC

with a charged drift chamber track.

Next a candidate particle list of all UVY sector triplets, whose V and Y sector positions predicted the U sector position, was formed. The candidate particle energies were then fit to the measured sector energies, by minimizing,

$$\chi^2 = \Sigma_i(e_i - \Sigma_j \alpha_{ij}\epsilon_j)^2 \frac{1}{\sigma_i^2}$$

where the e_i's were the measured sector energies, the σ_i's were the errors on these measurements, the α_{ij}'s were position dependent energy correction factors. The candidate particle energies, ϵ_j's, are the parameters to be fit. A stepwise regression method was used for the fit so that candidates could be added and subtracted without having to invert the entire correlation matrix each time.

The SLIC performed well in E791. We were able to reconstruct electromagnetic showers with an energy resolution of about $(\frac{\Delta E}{E})^2 \approx (11.5\%)^2 + (\frac{17.4}{E})^2$ and a position resolution of 7mm [Ga93].

3.7.2 The Hadrometer

The Hadrometer was a steel-acrylic scintillator calorimeter located downstream of the SLIC. It was used to reconstruct the energy of hadronic showers. Less than 1% of the energy of electromagnetic showers reached the hadron calorimeter. Therefore, charged hadrons could be identified as wide SLIC showers with significant hadronic energy behind them. Neutral hadrons were also identified after the hadronic energy associated with charged tracks was subtracted.

The processes that sustain a hadronic shower are quite different from those in an electromagnetic shower. In the E791 hadron calorimeter the showering is sustained by interactions in steel plates. About half of the incident hadron energy is passed on to fast secondaries and most of the remainder is used in the production of slow pions and other particles [Fe86]. The charged particles in the hadronic shower then produce light in the scintillators.

The Hadrometer contained 36 layers of 2.5 cm thick steel plates and 0.95 cm thick acrylic scintillator. The steel and acrylic together totaled 6 absorption lengths. The scintillator layers consisted of 14.5 cm wide plastic strips and alternated between the x-view, in which the strips ran vertically, and the y-view, in which the strips ran horizontally. The hadron calorimeter was divided into two modules, separated by a small gap, which each contained 18 layers. In the upstream module, the light from a set of nine horizontal plastic strips, which corresponded to the same y position in each successive y layer, was collected into a single phototube. Similarly, nine vertical strips which corresponded to the same x position in each successive x layer had their light summed together. The downstream module was read out in the same manner. The anode signals from the 5 inch EMI 9791KB phototubes were digitized by FERAs. The Hadrometer construction is shown in figure 3.6.

The relative calibration of the Hadrometer channels was measured using special muon runs. The muons were due to decay of our pion beam upstream of the experiment. Each muon deposited on average 2.4 GeV hadron equivalent energy in the calorimeter. This fact when folded in with the attenuation of the scintillator (energy measurements were a function of the distance from the phototube at which the shower intercepted the scintillator) was used to calibrate the hadrometer. The absolute calibration was obtained by minimizing the energy resolution of charged hadrons subject to the constraint that energy in the SLIC plus the energy in the Hadrometer equaled the measured momentum.

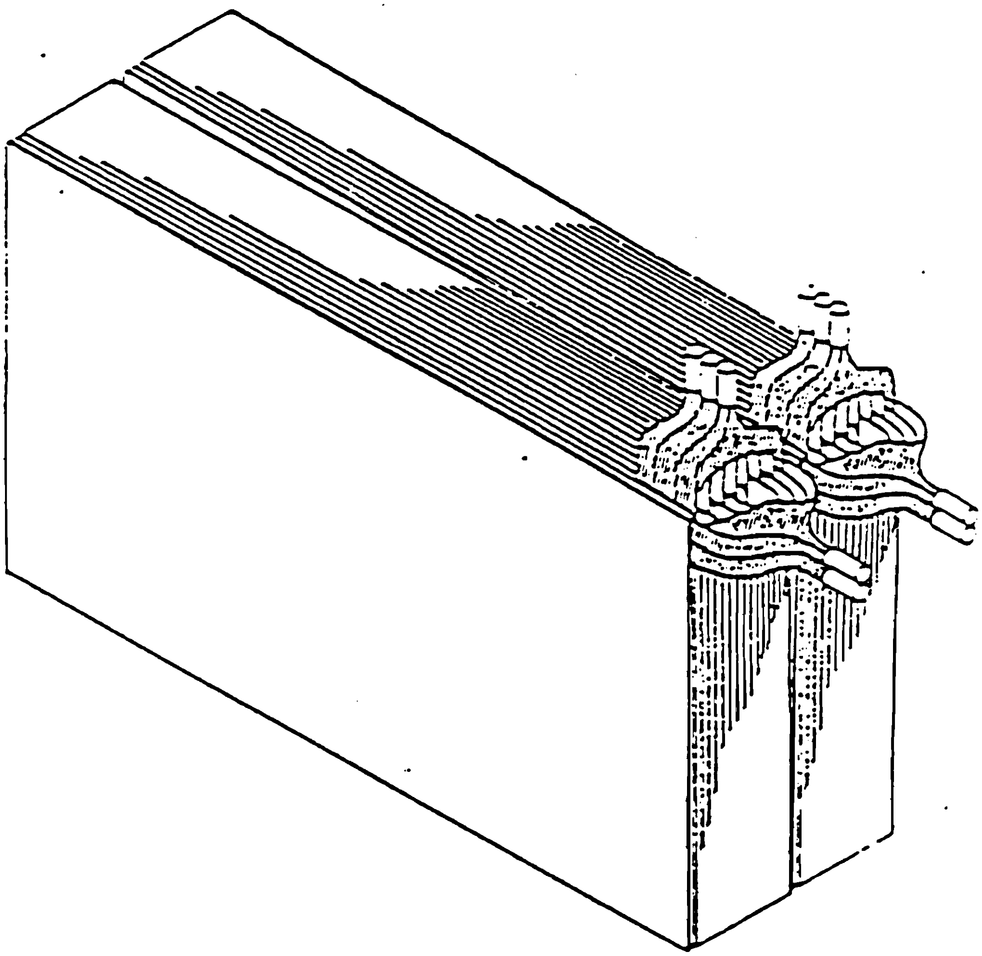

Figure 3.6: The Hadrometer

3.8 The Muon Walls

The muon walls were four sets of scintillation counters, one set located upstream of the target and the other three sets located downstream of the hadrometer. The vast majority of secondary particles, except for muons, deposited all of their energy in the SLIC and Hadrometer. Therefore, any particles detected downstream of the calorimeters were a priori assumed to be muons.

The most upstream muon wall was a set of 8 plastic scintillator panels. Light from the scintillators was collected by EMI 9791KB phototubes and the information from these phototubes was simply latched either on or off depending on the size of the light signals. The second set of muon detectors, the Back Muon X Wall, was a set of 15 plastic scintillator panels, the 12 paddles in the outer portion of the X wall were 41 cm wide, while the three central paddles were 61 cm wide. Light collected on their phototubes generated stops for TDCs with which the y coordinated could be measured. In addition, hits on these X wall panels were latched. The X wall paddles were 70 % [Wi94] efficient. The third set of muon scintillators were a two groups of two panels located downstream of the Back Muon X Wall. Two panels were mounted on the upstream face of a meter thick concrete block and the other two were mounted on the downstream face of that block. The information from these panels was latched. Finally, the most downstream detector in the experiment was the Back Muon Y Wall which was constructed by the University of Mississippi for E791. It consisted of 16 plastic scintillator strips that were 3 meters wide and 14.5 cm high. The signals from these detectors were latched and generated TDC stops which allowed measurement of the X coordinate as well. The Y wall was approximately 100 % [Wi94] efficient. The back muon Y wall is shown in figure 3.7.

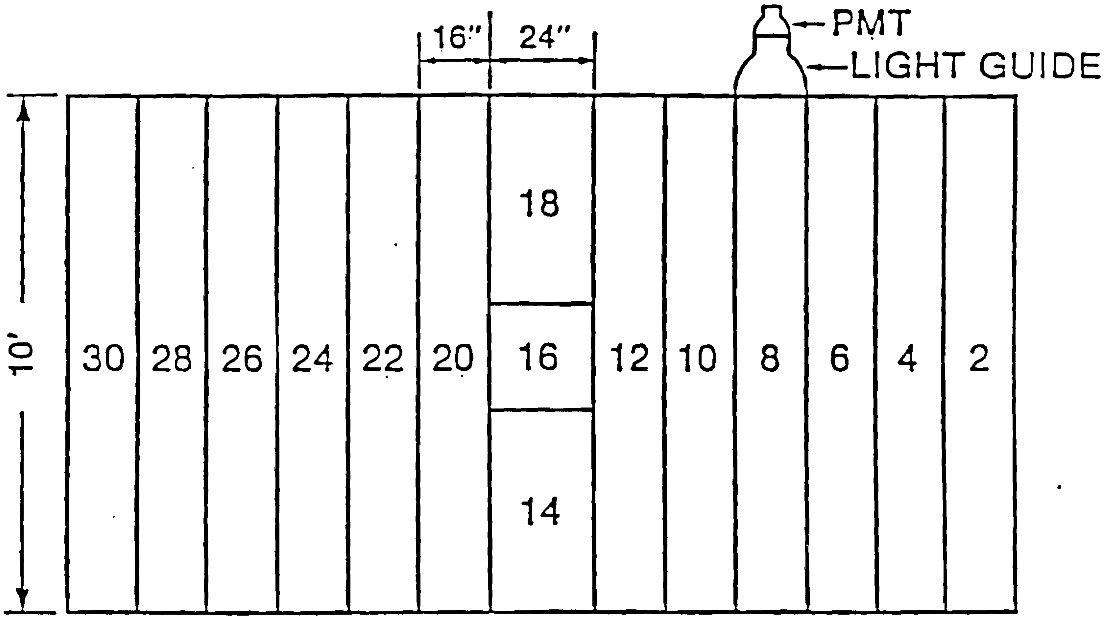

Figure 3.7: The Back Muon Y Wall

Chapter 4

Triggering

4.1 Introduction

E791's Experimental philosophy was to take data with a very open trigger and to prune events offline in software. Because of this, our trigger used a simple set of information to make trigger decisions. All the trigger decisions were made contingent on the states of three scintillator paddles, SLIC energy information, and accelerator timing information.

4.2 E_t triggers

The predominant type of triggers recorded for analysis were E_t triggers. They were called such because they made a cut on the amount of transverse energy in the calorimeters. Other types of triggers were taken for calibration and alignment and they will not be discussed here.

The E_t trigger decision was made based on the state of three scintillator paddles and calorimetry information. The paddles upstream of the target were the beam spot and beam halo counters. The purpose of these counters was to determine if a single beam particle had passed through the center of the target. The halo counter was a paddle with a 1 cm hole drilled in it. This made its active crossection the NOT of where the beam was supposed to be. The last trigger paddle was the Interaction counter. It provided information on whether a beam particle had interacted in the target. The final piece of trigger information was the energy in the SLIC and the Hadrometer. The outputs of the PMT dynodes from these detectors were summed together and weighted according to the distance of the channel from the center of the detector.

The outputs of these detectors were discriminated and the information was sent to a Programmable Logic Unit (PLU). The PLU made a trigger decision based on the states of it's inputs. For E_t triggers the relevant inputs were E_t Low, E_t too High, Good Beam, Multibeam Veto, and Raw Interaction. The E_t low signal is generated by discriminating the raw summed calorimetry information. The threshold was set so that a TRUE indicated a sufficient amount of energy in the calorimeters. The E_t too High signal was true when it appeared that the summed energy in the calorimeters was too large (indicative of multiple interactions). The Good Beam signal was true when the signal from the beam spot counter was above threshold and the signal from beam halo counter was below threshold. The Multibeam veto was TRUE when the beam spot counter signal was above a much larger threshold than that to generate a good beam signal. Finally, the Raw Interaction signal was true when the interaction counter was above threshold. The PLU defined the E_t trigger as

$$\begin{gathered} E_t = E_t \text{ Low .AND. Raw Interaction .AND. .NOT. Dirty Beam} \\ \text{.AND. .NOT. Multi Beam Veto .AND. NOT. } E_t \text{ too High} \end{gathered}$$

A trigger decision was only signaled when the PLU was strobed by Good Beam.

Chapter 5

The Data Acquisition System

Adapted from [Am93]

5.1 Introduction

E791's experimental philosophy was to impose only loose online triggering constraints on our data and to select charm events by offline filtering and reconstruction. In keeping with this philosophy our data acquisition system was designed to collect and record data very quickly. The DA system read out approximately 2500 bytes per event, characterizing the 24,000 channels of our spectrometer, with 50 micro-seconds of deadtime. This resulted in a data collection rate of 9.6 Mb/second, which corresponded to our 42 Exabyte tape drives being continually busy.

Schematically the DA system consisted of 5 basic components, Event FIFO Buffers (EFB), Event Buffer Interfaces (EBI), VME based CPUs, Exabyte Tape Controllers and Drives, and a VAX-11/780. The EFB's collected and buffered data from the detector digitizers, the EBI's served as interfaces between the FIFOs and the CPUs, the CPUs packaged data from various EFBs into event records and wrote

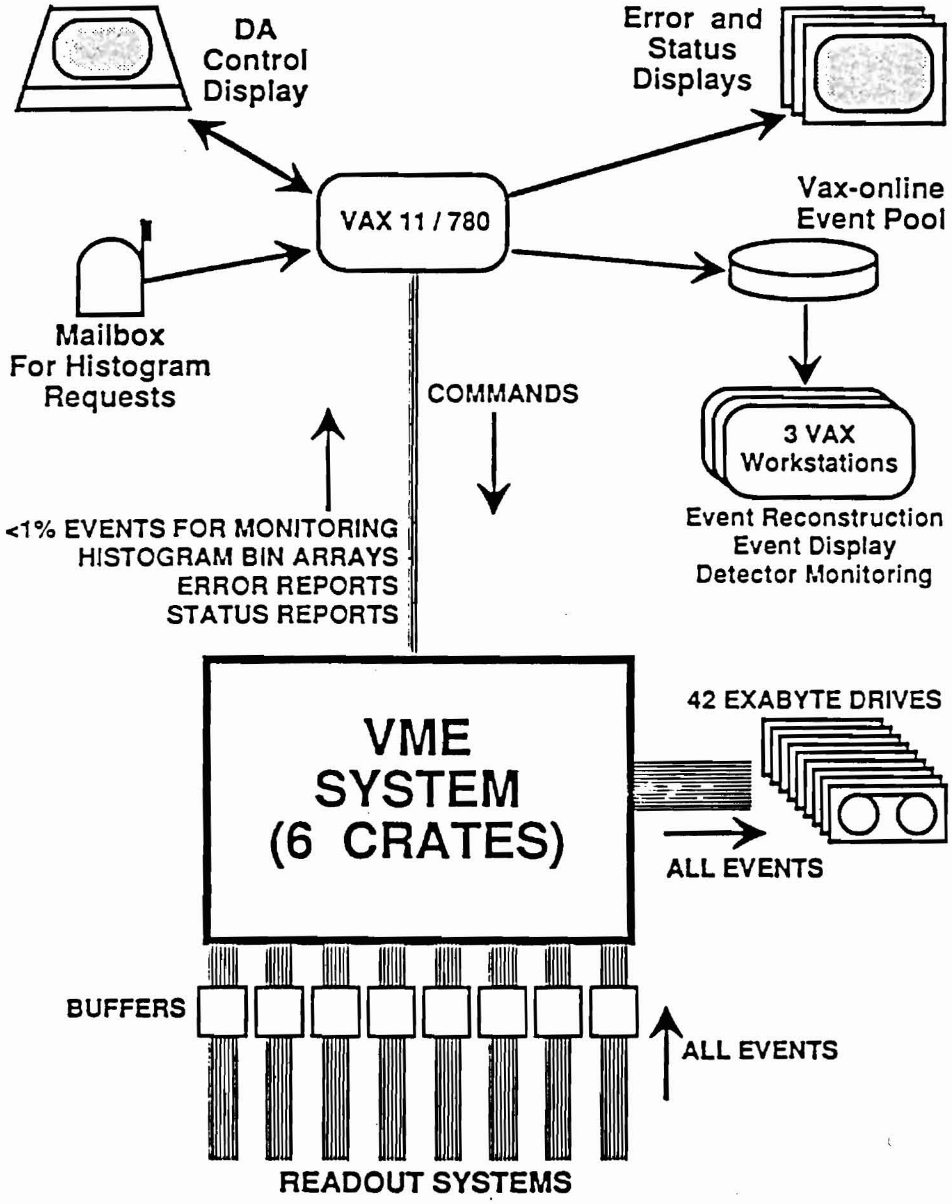

Figure 5.1: The Data Acquisition System

the records on the Exabyte tape drives, and the VAX-11/780 provided monitoring and user control.

5.2 Event FIFO Buffers

The Event FIFO buffers each consisted of five 16MB memory cards, an I/O card and a controller card. Data from the detector digitizers was placed in the FIFO's over a 32-bit wide RS-485 port accompanied by a strobe to latch the data. Similarly, an output RS-485 port was used to pull data from the EFBs to the EBIs. Also, the EFBs provided four status lines: full, near full, near empty, empty. The near full lines were used to inhibit triggering when any EFB was in danger of overflowing.

5.3 VME CPUs

The VME CPUs were Fermilab ACP I computers. They consisted of a 16 Mhz 60820 CPU, a 68881 coprocessor, and 2 Mb of Memory. It was their function to assemble events from the EFB longwords. In each VME crate there were nine CPUs: eight Event Handlers and one Boss CPU.

5.4 Event Buffer Interfaces

VME CPUs built events by extracting data from the EFBs through the EBIs. Each EFB was connected to six EBIs, one in each VME crate. Each VME crate held 8 EBIs, one for each EFB. Thus each CPU in each crate had access to data in every EFB. At any time, each EFB belonged to a single CPU; when the CPU was done reading data from the EFB, it passed a token granting control of the EFB to the next CPU in line. While one CPU was reading out one EFB, other CPUs in other VME crates could be reading out other EFBs.

The CPUs functioned alternately as Munchers or Grabbers. CPUs in the grabber state read data from the EFBs. While, Munchers took data from their internal event arrays and prepared them for output to tape. Only one CPU per crate could be in the grabber state so when a boss noticed a grabber was becoming full, it changed that Grabber to a munching state, and appointed a new Grabber.

5.5 Exabyte Tape Drives and Controllers

Forty two Exabyte-8200s writing single-density, 2.3 Gb 8mm tapes were necessary to sustain our data recording rate of 9.6 Mb/second. Each of the six VME crates was connected to 7 drives via two Ciprico RF-3513 VME to SCSI interfaces and each controller was connected to 3 and 4 tape drives respectively (this was necessary to prevent saturation of the SCSI buses).

5.6 The VAX-11/780

The VAX-11/780 was used to download and start the DA system, request and report status of the DA components, fetch a small number of events for online monitoring, and provide operator control of the DA system. The link between the VAX and the VME crates was provided by a DR11-W on the VAX Unibus, a QBBC branch bus controller, and branchbus to VME interfaces in each VME crate.

5.7 Operation

The VAX provided DA monitoring and user control. Eight DA control commands were available to the operator. The operator could LOAD and UNLOAD Exabyte tapes in their drives, START and END a DA run, PAUSE and RESUME a DA run, Clear the EFBs (CLEAR BUFFER was useful when DA errors were reported), or Print the error logs (PRINT ERROR). Also, the VAX console provided information continuously on the basic status of the run, such as the run number, total time of the run, events munched, and the percentage of tape used. Finally, the VAX received error reports from the Bosses and the Munchers.

At the beginning of a run a set of 42 8mm tapes were loaded into the Exabyte tape drives and a LOAD command was issued at the DA VAX console. After a BEGIN RUN command was issued at the console, data acquisition commenced.

Immediately, the detector digitizers began filling their EFBs. When the first EFB Empty line was no longer asserted, the Grabber in the first crate began reading the first EFB through it's corresponding EBI. When the Grabber in the first VME crate had finished reading an event segment from the first EFB it passed that EFB's token to the next crate. This process continued with each crate passing tokens to EFBs it had just read to the next crate. The Grabber's only function was to read event segments from the EFBs and place them in a large internal event array. As Grabbers read data from the EFBs they checked to make sure all event segments being concatenated had the same event synchronization number (a number provided with each event segment from a four digit scaler). This insured that event segments from different events were not joined together. When the BOSS CPU noticed a Grabber's internal event array was close to being full it converted that CPU to a Muncher and recruited another Grabber for the crate.

A CPU in the Munching state was responsible for assembling events in it's internal event array into tape records. Munchers also binned internal DA histograms and responded to status requests. When a tape record was ready for writing, the Munchers submitted their requests to BOSS CPU which handled tape writing.

Besides scheduling Event Handlers as either Grabbers or Munchers, the Boss CPU managed tape writing. The Boss periodically polled Event Handlers for a list of tape buffers ready to be written. The Event Handlers gave the Boss the VME address and length of these buffers. The Boss then constructed commands for the tape controllers based on this information. After a tape buffer was written the controller notified the Boss, which in turn informed the Event Handler that the tape buffer was again free to be used.

A run ended when either the operator issued an END RUN command or when 20% of the tape drives were 95% full. Once the run ended, an end of file mark was written on the tapes and they were rewound and unloaded. The 42 tapes were then collected, the run was labeled and stored for offline analysis.

5.8 System Performance

The E791 Data Acquisition System successfully collected 20 billion physics events and 200,000 charm events on 24,000 8mm tapes. The DA was fast enough to saturate 42 Exabyte tape drives continuously. In addition, the DA proved to be fault tolerant and easy to operate. In general it performed well.

Chapter 6

Event Reconstruction and Selection

6.1 Introduction

During the 1991 run, we accumulated approximately 25,000 2.2 GB 8mm tapes of raw data. Therefore, a large portion of the technical challenge in E791 was to reduce this sample efficiently and effectively to a more usable amount of data.

Our reconstruction procedure is illustrated schematically in figure 6.1.

6.2 Event Reconstruction

E791 required a formidable amount of computing to reconstruct, filter, strip and substrip our dataset.

Reconstruction and filtering were performed on large computing farms at Kansas State University , The University of Mississippi, The Centro Brasileiro de Pequisas Fisicas (CBPF), and Fermilab. At KSU about 2500 MIPS of DEC Risc workstations were combined into four computing farms. Events were farmed out to processors, partially reconstructed, and then filtered. Those that passed the filter

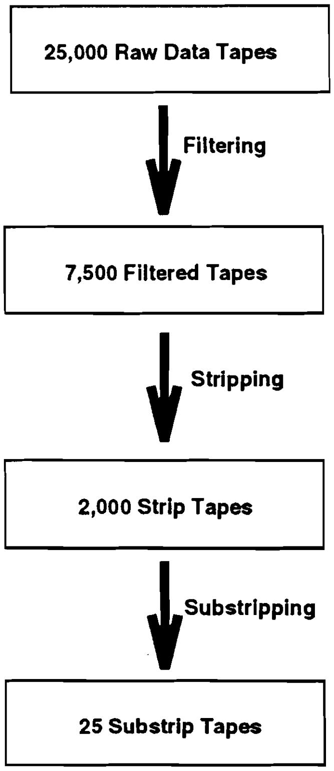

Figure 6.1: E791 Event Selection

cuts were fully reconstructed and written to tape (the filter tapes). Reconstruction and filtering proceeded identically at Mississippi and Fermilab except that Mississippi had about 2900 MIPS of computing, CBPF has approximately 1000 MIPS of computing, and Fermilab had about 1000 MIPS of computing.

The stripping job was I/O rather than CPU bound so stripping was performed on single workstations.

Finally substripping for this thesis was performed at Princeton on our SGI 4D/480S.

6.3 Physics Cuts

The cuts used for filtering, stripping, substripping, and analysis were specific to E791. As such they need some explanation. Values of the cuts used are summarized in tables 6.1 - 6.5.

6.3.1 SDZ

Perhaps the most effective cut, in terms of enhancing signals relative to noise was the SDZ cut. SDZ characterized the statistical significance of the Z separation between the primary and the secondary vertices. It is defined as SDZ $\equiv \frac{\Delta Z}{\sigma_z}$ ($\sigma_z = \sqrt{\sigma^2_{Zprimary} + \sigma^2_{Zsecondary}}$). A reasonable cut on SDZ eliminated the secondary vertices formed from primary vertex tracks, which dominate at low SDZ, close to the primary vertex.

6.3.2 P_t Balance

Another useful cut, P_t balance, is illustrated in figure 6.2.

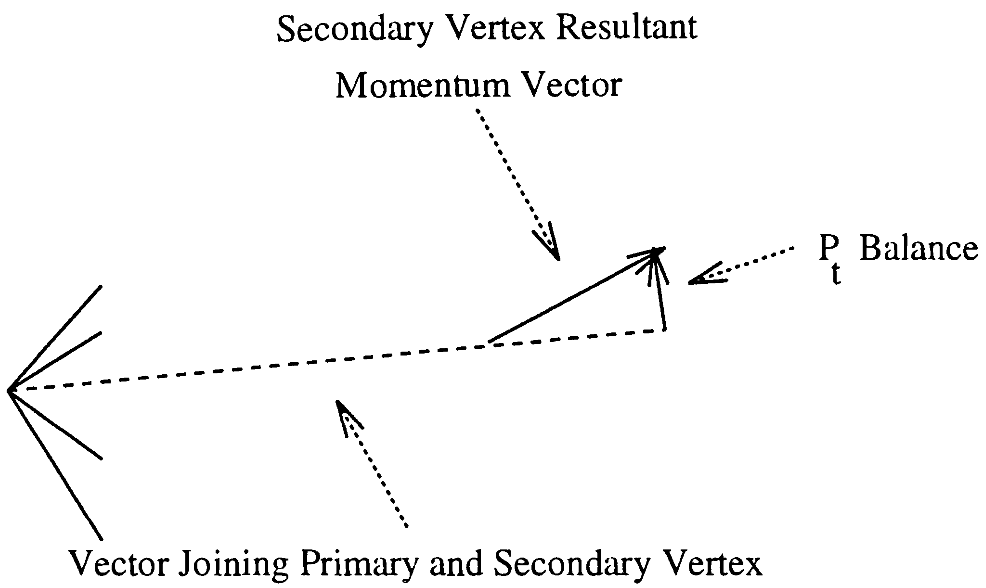

Figure 6.2: P_t balance

The P_t balance cut was a limit on the p_t of the secondary vertex tracks relative to the vector joining the primary and secondary vertices. In principle, for a real particle decay into all charged daughters, P_t balance should have been zero.

6.3.3 *D* Impact Parameter

The *D* Impact Parameter cut is illustrated in figure 6.3.

The DIP cut was made by forming the *D* trajectory from its decay products and projecting back to the primary vertex. A cut was made on the impact parameter in the X-Y plane at the primary vertex Z. *D* decays of interest, where all decay particles are reconstructed should have zero DIP. Random combinatoric backgrounds should also have low DIP , however higher mass charm backgrounds, where one or two decay particles go undetected should be severely reduced by this cut.

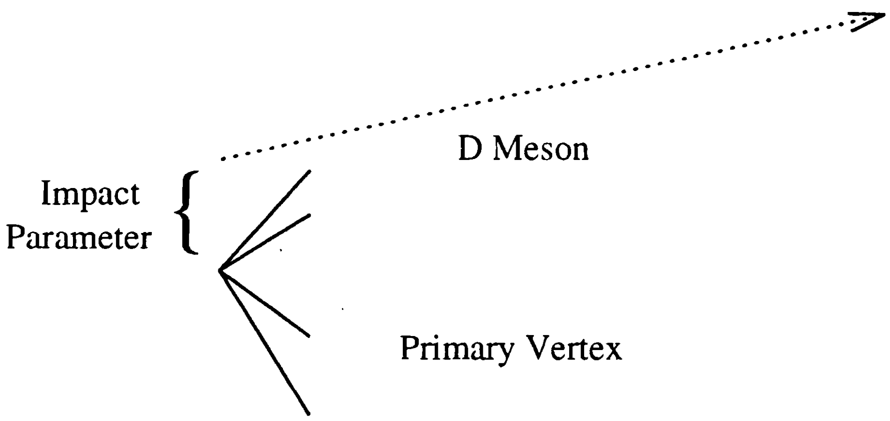

Figure 6.3: DIP cut

6.3.4 Čerenkov Probability

Information from our Čerenkov detectors was used to form (in a manner described in Chapter 3) a probability for each track to be either an e,μ, π, K, or p. In the substripping and analysis stages particularly tight cuts on the kaon Čerenkov probability were made. The efficiency for the kaon probability cuts (integrated over all momenta) was typically 60 % [Pu93].

6.3.5 χ^2 / Degree of Freedom

χ^2's were calculated for charged track fits. In general, tracks with large χ^2's were removed.

6.3.6 Target Sigma Cut

One large source of background was secondary interactions in target foils downstream of the primary vertex. Therefore, all secondary vertex candidates were required to be at least two standard deviations in z outside of the target foils or the interaction counter. This cut removed 10 % of the signal (for $D^+ \rightarrow K^-\pi^+\pi^+$) and 75 % of the background.

6.3.7 Track Category

A requirement was made that all the tracks in a vertex pass through both analysis magnets or that they passed through one magnet and satisfied the requirments of a neural net trained by to eliminate ghosts. In the parlance of E791 this was a requirement that that the tracks be either category 7 or category 15 or have newcatsg equal to 3.

6.3.8 Isolation

A cut was made requiring the candidate secondary vertexes to be isolated. That is there was no more than one track within a 50 micron radius of the vertex in the X-Y plane at the vertex's z position. This requirement eliminated many vertices formed because of poor reconstruction i.e., a vertex that was in reality a five prong is reconstructed as a two and a three prong. It also eliminated many vertices formed by combinatorics which is more common in regions with a high track density.

6.3.9 CHVXTK

A variable called CHVXTK was calculated for each track. It measured the amount of χ^2 a track would add to the primary vertex fit if it were included in the fit. Tracks with small CHVXTK were most likely primary vertex tracks missed by the reconstruction algorithm. Therefore, it was required that all tracks in a secondary vertex have a CHVXTK greater than 25.

6.3.10 Ratio

The RATIO is another quantity that parameterizes the likelihood that the secondary vertex does not contain any tracks originating from the primary interaction point. For each track, the impact parameter with respect to the secondary vertex and with respect to the primary vertex is calculated. The product of the ratios of the secondary vertex impact parameter to the primary vertex impact parameter for each track in the secondary vertex is assigned to the variable RATIO. The smaller the RATIO the more likely it is that none of the tracks in the vertex are from the primary vertex.

6.4 Filtering

The first step in the reduction of our raw data was filtering. The beam track, vertex silicon tracks, track momentum, and vertices were reconstructed at this point. If a primary vertex was found the filter then performed the Čerenkov and ESTR reconstruction. ESTR is the acronym for the portion of our charged particle tracking code that reconstructed tracks formed only from drift chamber hits. The remainder of the filtering process was separated into several distinct parts which had several physics goals. The majority of the physics done by E791 was filtered with a selection on secondary vertices in the silicon (the filter selection for the physics of this thesis), or a selection on two prong V's formed from drift chamber only tracks. In addition, other filters were included for special decay modes (B decays, diffractive jets, candidate driven baryon searches, and others).

Charm particle lifetimes are such that those produced in our target foils decay mostly before the silicon assembly. Therefore, those that decay into at least two charged tracks are identified by looking for secondary vertices (vertices downstream of the primary vertex) in the fiducial volume upstream of our silicon system.

The secondary vertex selection was performed by requiring events to have at least two vertices (a primary plus at least one downstream vertex). If any of the downstream vertices were two prongs with an SDZ > 6 or three or greater prongs with an SDZ > 4 then the event was selected.

Because of the long lifetime of strange particles, a substantial fraction of strange neutral particles such as the K_s's and Λ's were not likely to be detected in our silicon system. Since these particles were excellent tags of charm it was necessary to make an ESTR V selection for them. We made various cuts to search for the two prong (hence V) decays of these particles.

The ESTR V selection was made by combining ESTR tracks. The tracks were required to have a χ^2 per degree of freedom < 5, momentum between 0.5 and 500 GeV, and to have opposite charge. To select K_s's the daughters were assumed to pions. If the invariant mass formed with this assumption was between 0.47 and 0.52 GeV and the distance of closest approach between the two tracks was less than 0.5 cm the event was selected. Λ's were selected by making similar cuts (the DCA cut was relaxed to 0.7 cm), except that the invariant mass formed by assuming one daughter was a proton and the other a pion was was required to be between 1.101 and 1.127 GeV.

Another major component of our filter was a candidate driven search for Φ's using SMD tracks. The Φ's were selected by looking for two tracks with a joint Čerenkov Kaon probability greater than 0.05. If the invariant mass formed by assuming both daughters were Kaons was within 10 MeV of the Φ mass, then the event was selected.

Events that passed these criteria were fully reconstructed and the information was placed in a data summary common block. Approximately, 16 % of raw data events passed these selection criteria. However, the size of the data summary information was approximately equal to the size of the raw data, hence the physical number of tapes was reduced to only one-third of the number of raw data tapes.

The filter cuts are summarized in table 6.1.

6.4.1 Silicon Track Reconstruction

The reconstruction of charged particle tracks in our silicon system was performed by a software package called STR. Schematically, the silicon track reconstruction proceeds by first performing one dimensional tracking in each SMD view. Seed tracks in each view are straight lines that pass through at least two hits. The algorithm then attempts to find additional hits on these seed tracks. Four hits are required in X and Y view and three in the V view in order to form a good one dimensional track candidate. Finally, the program combines individual one dimensional tracks from different views into a full three dimensional track. A full three dimensional straight line fit is done to the hits on these tracks. A Neural Net has been trained to discard ghost tracks based on certain characteristics of the tracks.

6.4.2 Vertex Reconstruction

The reconstruction of vertices in our silicon system was performed by software package called VTXSTR designed by Ron Sidwell and partly based on the work of Noel Stanton. VTXSTR finds both the primary vertex and secondary vertex tracks.

To locate the primary vertex it takes good tracks that intercept the beam and attempts to fit a vertex them. Once a good two prong vertex that intercepts the beam is found, additional tracks are added to the primary if they do not add too much χ^2 to the primary vertex fit.

VTXSTR then attempts to vertex the good silicon tracks that are not in the primary vertex. It starts by looking for two tracks with a small distance of closest approach. If they successfully fit to a vertex additional tracks are added in provided they do not add to much χ^2 to the fit.

6.5 Stripping

The next set of selection criteria were made on the fully reconstructed events that passed the filter. These stripping cuts were used to reduce the data to manageable datasets targeted for specific physics analyses. E791's ability to do a large variety of charm physics meant a large number of tagging procedures were necessary at the strip level. In addition, to the silicon secondary vertex stripping tag used in this thesis there were many tagging procedures at the strip level. Events were tagged by a multi-lepton tag, a K_s and Λ tag, a Φ tag, a pentaquark tag, and many others.

For this thesis, the stripping routine that tagged secondary three prong vertices was used. Three prong secondary SMD vertices were tagged if their net charge was ± 1, their SDZ was > 5, the vertex's P_t balance was < 1 GeV, and the vertex's lifetime was between 0 and 5 picoseconds.

The strip cuts for three prong vertices are summarized in table 6.2

6.6 Substripping

The final step before tighter analysis cuts were applied was substripping. Because the topic of this thesis is rare decays tight cuts were used in substripping to produce

Table 6.1: Summary of Filter Cuts

	Filter	Name of Cut	Cut made
SMD Vertex			
	2 prongs	SDZ	> 6
	3 or more prongs	SDZ	> 4
ESTR V's			
	Select K_s	Tracks' χ^2/DOF	< 5
		Tracks' Momentum	$0.5 < \mathrm{P} < 500$
		DCA	< 0.5 cm
		Mass Window	50 MeV
	Select Λ	Tracks' χ^2/DOF	< 5
		Tracks' Momentum	$0.5 < \mathrm{P} < 500$
		DCA	< 0.7 cm
		Mass Window	16 MeV
	Select Φ	Tracks' χ^2/DOF	< 5
		Tracks' Momentum	$0.5 < \mathrm{P} < 500$
		DCA	< 0.5 cm
		Joint Kaon Čerenkov Prob.	> 0.05
		Mass Window	10 MeV

Table 6.2: Summary of Three prong Strip Cuts

Name of Cut	Cut Made
SDZ	> 5
P_t Balance	< 1 GeV
Lifetime	$0 < \tau < 5$ picoseconds

Table 6.3: Summary of $D \rightarrow K\pi\pi$ Substrip Cuts

Name of Cut	Cut Made
SDZ	> 8
P_t Balance	< 0.35 GeV
DIP	< 60 microns
K Čerenkov Prob	> 0.14
Track χ^2 /DOF	< 6
Mass Window	$1.7 <$ MASS < 2.0 GeV

very clean signals.

6.6.1 $D^+ \rightarrow K\pi\pi$

For substripping of the $D^+ \rightarrow K^-\pi^+\pi^+$ and $D^+ \rightarrow K^+\pi^-\pi^+$ modes, cuts of SDZ $>$ 8, DIP $<$ 60 microns, P_t Balance $<$ 0.35 GeV, kaon Čerenkov probability $>$ 0.14, and Track χ^2 / Degree of Freedom $<$ 6 were made on three prong vertices. Also events were only selected if they were within a mass window between 1.7 and 2.0 GeV.

The cuts for this substrip are summarized in table 6.3.

6.6.2 $D^+ \rightarrow K^+K^+K^-$

The substripping of $D^+ \rightarrow K^+K^+K^-$ events was nearly identical to the substripping of $D \rightarrow K\pi\pi$ events. Cuts of SDZ $>$ 8, DIP $<$ 60 microns, P_t Balance $<$ 0.35 GeV were made on three prong vertices. Also it was required that at least one of the tracks in the vertex have a kaon Čerenkov probability $>$ 0.14. Finally, the invariant mass of the vertex (assuming all the particles were kaons) was required to be between 1.7 and 2.0 GeV.

The cuts for this substrip are summarized in table 6.4.

Table 6.4: Summary of $D \rightarrow KKK$ Substrip Cuts

Name of Cut	Cut Made
SDZ	> 8
P$_t$ Balance	< 0.35 GeV
DIP	< 60 microns
Any Track K Čerenkov Prob	> 0.14
Track χ^2 /DOF	< 6
Mass Window	$1.7 <$ MASS < 2.0 GeV

Table 6.5: Summary of $D \rightarrow KK\pi$ Substrip Cuts

Name of Cut	Cut Made
SDZ	> 8
P$_t$ Balance	< 0.35 GeV
DIP	< 60 microns
K Čerenkov Prob	> 0.14
Track χ^2 /DOF	< 6
Mass Window	$1.7 <$ MASS < 2.2 GeV

6.6.3 $D^+, D_s^+ \rightarrow K^+K^-\pi^+$

The substripping of $D^+, D_s^+ \rightarrow K^-K^+\pi^+$ events was very similar to the substripping of $D^+ \rightarrow K^+K^+K^-$ and $D^+ \rightarrow K^{\pm}\pi\pi$ events. Three prongs vertices with a net charge of ±1 were considered. They were required to have SDZ >8, DIP < 60 microns, P$_t$ Balance < 0.35 GeV, and track χ^2's < 6. The particle with sign opposite that of the D was required to have a kaon Čerenkov probability greater then 0.14. Finally the invariant mass of the vertex assuming two kaons and one pion was required to be between 1.7 and 2.2 GeV.

The substrip cuts are summarized in table 6.5.

Chapter 7

Search for $D^+ \to K^+\pi^+\pi^-$

7.1 Introduction

It is naively expected that the doubly Cabibbo suppressed decays (DCSDs) of the D^+ are suppressed by a factor of order $\frac{1}{\tan^4\theta_c} \approx 400$. Therefore, in order to measure the branching fraction of $D^+ \to K^+\pi^+\pi^-$ (a doubly Cabibbo suppressed decay) one needs a sample of at least several thousand D^+'s. E791's total data sample contains approximately 200,000 fully reconstructed charm decays and will therefore have the statistical power to investigate these decays.

In this chapter, a high sensitivity search for the decay $D^+ \to K^+\pi^+\pi^-$ is described. It proceeds by analyzing the output of the $D^+ \to K^+\pi^+\pi^-$ substrip, which is described in the previous chapter. Since, the observation of rare decay modes requires that the amount of background be small, a series of tighter analysis cuts, as well as several mass reflection cuts are applied to both the Cabibbo favored (CFDs) and the doubly Cabibbo suppressed (DCSDs) candidates. The resulting invariant mass distributions are fit to Gaussians plus linear backgrounds and Gaussians plus simulated background shapes in the case of DCSD. The uncorrected amount of

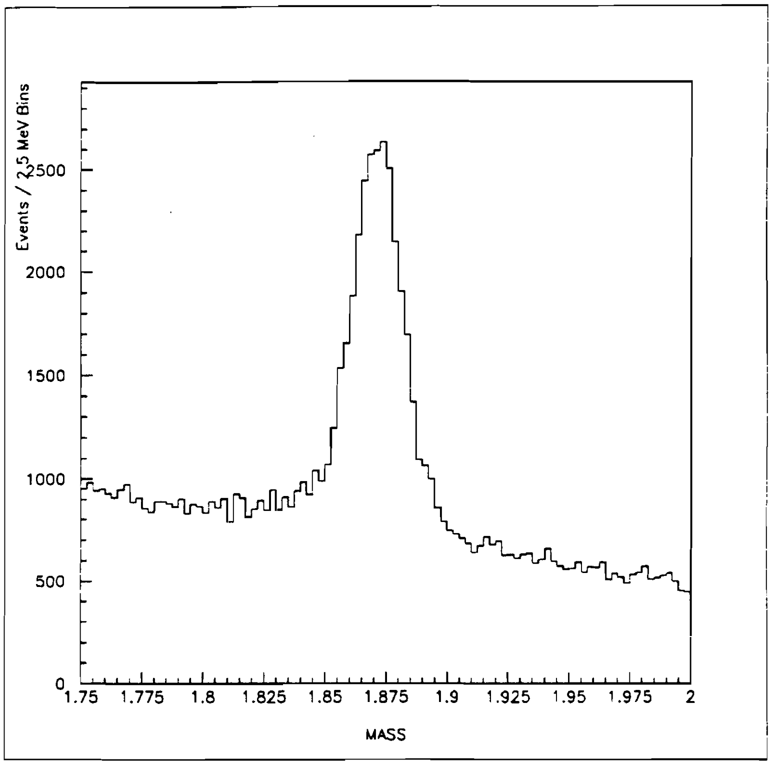

Figure 7.1: $D^+ \rightarrow K^-\pi^+\pi^+$ candidates after substripping and requiring that tracks pass through both analysis magnets

doubly Cabibbo suppressed decays and Cabibbo favored decays are determined from the fits. The major source of systematic difference between the CFD and DCSD samples is particle identification. For the Cabibbo favored mode the kaon is identified solely by charge, while for the doubly Cabibbo suppressed mode it is identified by charge and Čerenkov probability. After correcting for this difference a measurement of the relative branching fraction $\frac{\Gamma(D^+\rightarrow K^+\pi^+\pi^-)}{\Gamma(D^+\rightarrow K^-\pi^+\pi^+)}$ is obtained.

The analysis proceeds by distilling the raw E791 dataset of 20 billion events into a more manageable sample of $D^+ \rightarrow K^\pm\pi\pi$ candidates. This process is described in detail in the previous chapter. The results of reconstructing, filtering, stripping, and substripping 194 runs, about $\frac{1}{3}$ of our data, is presented in figure 7.1.

The entries in the histogram in figure 7.1 are the invariant masses of all three

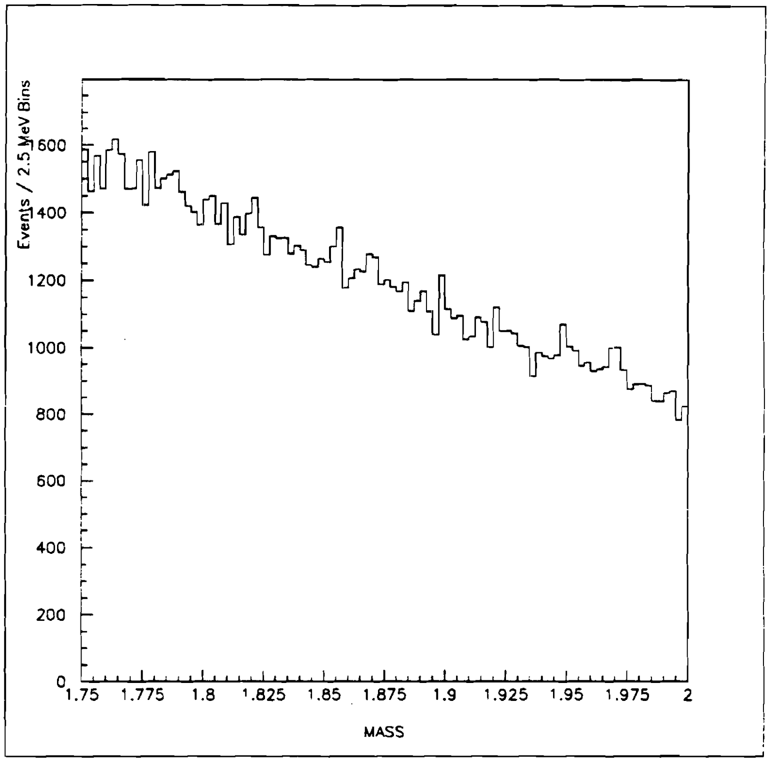

Figure 7.2: $D^+ \rightarrow K^+\pi^+\pi^-$ after substripping
and requiring that tracks pass through both analysis magnets

prong candidates with a charge of ± 1. The particle that has charge opposite to the D^+ candidate is called the kaon. The events in this histogram have passed the substrip.

A similar sample of $D^+ \rightarrow K^+\pi^+\pi^-$ candidates is formed by making the same track quality cuts on the substripped data. The results are shown in figure 7.2. In this case the particle called the kaon is the particle of the same sign as the D^+ with the largest kaon Čerenkov probability. Note that this is different than the way the kaon is identified in the Cabibbo favored case which is simply by charge. This is a difference which must be studied if the branching ratio is to be properly measured.

7.2 Analysis Cuts

The samples of $D^+ \rightarrow K^-\pi^+\pi^+$ and $D^+ \rightarrow K^+\pi^+\pi^-$ candidates (the charge conjugate modes are included implicitly) shown in figures 7.1 and 7.2 are the starting points for this analysis. At the analysis level further cuts must be placed on the candidate events in order to enhance the statistical significance $(\frac{\text{Signal}}{\sqrt{\text{Signal+Background}}})$ of the DCSD signal. At all costs one wishes to avoid tuning the analysis cuts on the DCSD sample. Therefore, the cuts have been chosen by tuning on the Cabibbo favored sample. Since this dataset is completely uncorrelated with the DCSD candidates doing this will not bias the DCSD analysis. The analysis cuts were chosen to maximize the statistical significance of the Cabibbo favored signal assuming that the size of the signal was suppressed by a factor of $5 \times \tan^4\theta_c$ and the background was unchanged. The initial values of the cuts were chosen by a trial and error method. An attempt was made to improve upon the cuts produced by trial and error by using Fisher linear discriminant techniques (see appendix A), the imputed statistical significance of the DCSD signal (again assuming the background was the same and the DCSD signal was suppressed by a factor of $5 \times \tan^4\theta_c$) wasn't significantly improved by this technique. Therefore, the cuts produced by trial and error were used. The optimal analysis cuts are listed in table 7.1. The meanings of these selection criteria were discussed in the previous chapter. The effects of these cuts (their efficiency on signal and background) is summarized in table 7.2. The efficiencies were obtained by applying each cut individually to substripped data. The $D^+ \rightarrow K^-\pi^+\pi^+$ signal after all of these analysis cuts is shown in figure 7.3. The background height is 8 events per 5 MeV bin in the bin at 1.871 GeV.

Later in this chapter, a measurement of the relative branching ratio $\frac{\Gamma(D^+\rightarrow K^+\pi^+\pi^-)}{\Gamma(D^+\rightarrow K^-\pi^+\pi^+)}$ will be made. Although, the analysis cuts haven't been tuned on the numerator,

Table 7.1: Analysis Cuts

Name	Cut
Track Category	New Cat 3,7, or 15
Track χ^2	< 5
SDZ	>20
P_t Balance	$< .25$ GeV
Kaon $\check{C}$ Probability	$> .3$
DIP	$< 30\ \mu$
Isolation	< 2
σ outside of target	> 2
CHVXTK	$>25.$
Pion $\check{C}$ Probability	$> .55$
Ratio	$< .001$
Z Secondary	$< -.28$ cm

Table 7.2: Summary of Cut Effects

Name	Signal Efficiency	Background Efficiency
Track Category 7 or 15	85 %	60 %
Track $\chi^2 < 5$	96 %	89 %
SDZ >20	92 %	62 %
P_t Balance $< .25$	91 %	65 %
Kaon $\check{C}$ Probability $> .3$	84 %	48 %
DIP $< 30\ \mu$	92 %	65 %
Isolation < 2	91 %	58 %
σ outside of target > 2	88 %	58 %
CHVXTK $>25.$	100 %	74 %
Pion $\check{C}$ Probability $> .55$	93 %	78 %
Ratio $< .001$	89 %	57 %
Z Secondary $< -.28$ cm	85 %	70 %

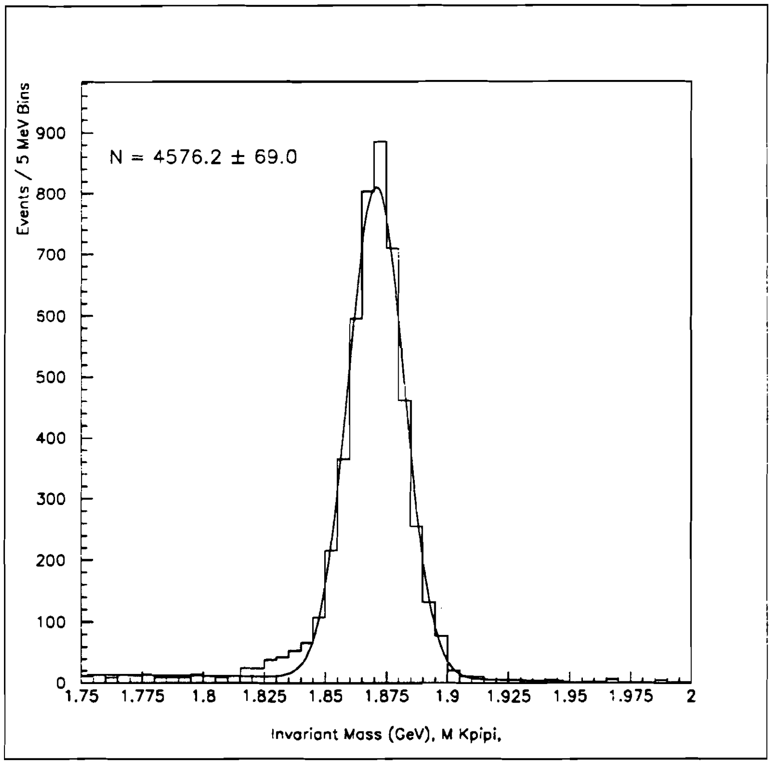

Figure 7.3: Invariant Mass of $D^+ \rightarrow K^-\pi^+\pi^+$ candidates
After all analysis Cuts

one may object that they have been tuned on the denominator. However, given the large number of $D^+ \rightarrow K^-\pi^+\pi^+$ events and the relatively small number of analysis cuts it is unlikely we are fooling ourselves as to the actual number of $D^+ \rightarrow K^-\pi^+\pi^+$ events.

The analysis cuts significantly reduce the background of both the Cabibbo favored and doubly Cabibbo suppressed events while being 40 % efficient on $D^+ \rightarrow K^-\pi^+\pi^+$ candidates that have passed the substrip cuts. In fact, because the background is reduced so much, the statistical significance of the $D^+ \rightarrow K^-\pi^+\pi^+$ signal is essentially unchanged.

7.3 DCSD Background

The measurement of $D^+ \rightarrow K^+\pi^+\pi^-$ is dependent on the assumed background shape. It is important to study possible backgrounds in order to better understand the background shape and also to make sure no known decays are faking a signal. It is assumed that the significant contribution to DCSD backgrounds from charm decay modes are from those modes that can be misconstrued as $D^+ \rightarrow K^+\pi^+\pi^-$ after a small number of reconstruction errors. Table 7.3 lists the most probable charm backgrounds and the reconstruction errors that would allow them to be interpreted as $D^+ \rightarrow K^+\pi^+\pi^-$ events.

One source of charm background to $D^+ \rightarrow K^+\pi^+\pi^-$ is $D^+ \rightarrow K^-\pi^+\pi^+$. The invariant mass of the the DCSD candidates when it is assumed they are CFD is shown in figure 7.4. The large peak (200 ± 15 events) in this "reflected" mass spectrum is due to CFD which also satisfy the DCSD analysis cuts. Therefore, a reflected mass cut is made when the right sign particle (the particle with sign opposite to the D^+) in the $D^+ \rightarrow K^+\pi^-\pi^+$ candidates is assumed to be the kaon

Table 7.3: Major Charm Backgrounds to $D^+ \rightarrow K^+\pi^+\pi^-$

Mode	Problem
$\overline{D}^0 \rightarrow K^+\pi^+\pi^-\pi^-$	Missing pion
$\overline{D}^0 \rightarrow K^+\pi^-$	Erroneous Added Pion
$\overline{D}^0 \rightarrow K^+\pi^-\pi^0$	Erroneous Added Pion
$D^+ \rightarrow \pi^+\pi^+\pi^-$	Single Misidentification
$D^+ \rightarrow K^+K^-\pi^+$	Single Misidentification
$D^+ \rightarrow K^-\pi^+\pi^+$	Double Misidentification
$D^+ \rightarrow K^-\pi^+\pi^+\pi^0$	Double Misidentification
$D_s \rightarrow K^+K^-\pi^+$	Single Misidentification
$D_s \rightarrow \phi e\nu$	Double Misidentification
$\Lambda_c^+ \rightarrow p^+K^-\pi^+$	Double Misidentification

and the other particles are assumed to be pions. The cut is placed between 1.84 and 1.90 GeV (the shaded region in figure 7.4) in order to remove Cabibbo favored decays that are misinterpreted as doubly Cabibbo suppressed decays because of a double misidentification.

Other possible significant sources of background to $D^+ \rightarrow K^+\pi^-\pi^+$ decays are $D^+, D_s \rightarrow K^+K^-\pi^+$ decays (including the resonances $D^+, D_s \rightarrow \phi\pi^+$, $D^+, D_s \rightarrow K^{*0}K^+$) in which the K^- is misinterpreted as a pion. The invariant mass spectrum for the DCSD candidates when the π^- is assumed to be a kaon is shown in figure 7.5. (The reflected mass cut to remove $D^+ \rightarrow K^+\pi^+\pi^-$ events has already been made.) A clear peak (83 ± 12 events) , at 1.97 GeV, can be seen in this "reflected" mass spectrum. Obviously the majority of events in the shaded region are not $D^+ \rightarrow K^+\pi^+\pi^-$ events and therefore candidates in this region of the reflected mass spectrum are discarded. A much smaller peak at 1.89 GeV (it is not as obvious because the rapidly rising background in that mass region makes the peak appear to be part of the flat background at higher masses) due to $D^+ \rightarrow K^+K^-\pi^+$ is visible. These backgrounds are removed by cutting out the shaded regions in

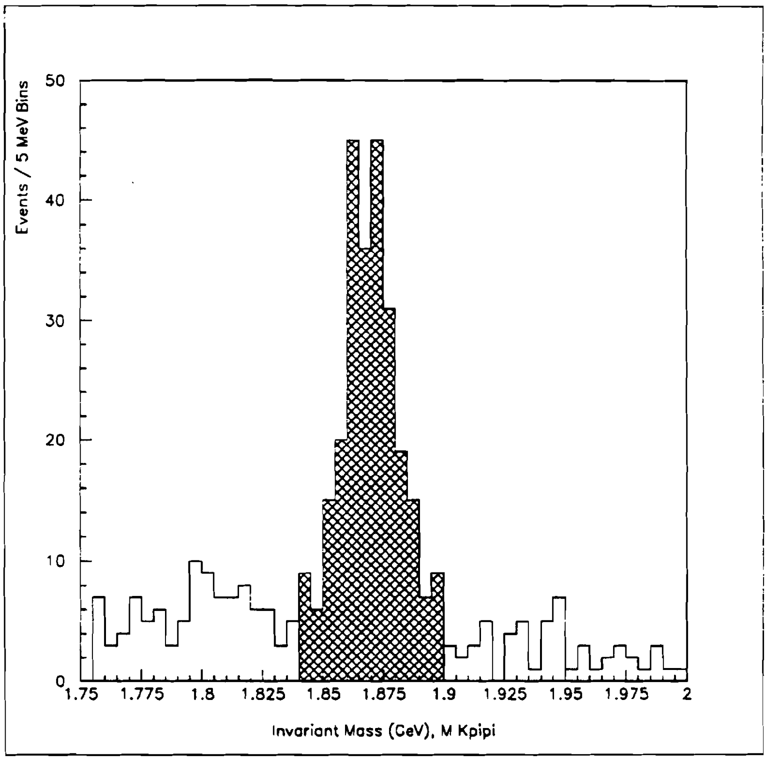

Figure 7.4: Invariant mass of the $D^+ \to K^+\pi^-\pi^+$ candidates When the π^- is assumed to be a K^-

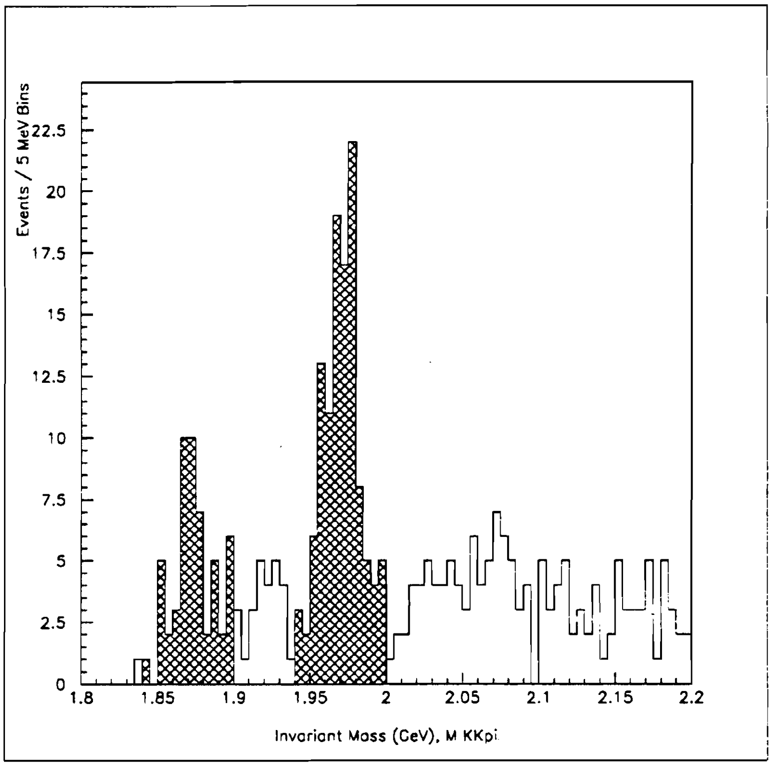

Figure 7.5: Invariant mass of the $D^+ \to K^+\pi^-\pi^+$ candidates reflected into $D^+ \to K^+K^-\pi^+$

figure 7.5 (between 1.84 and 1.90 GeV and between 1.94 and 2.0 GeV).

The same reflected mass cuts are also applied to the $D^+ \to K^-\pi^+\pi^+$ events so that CFD and DCSD samples are directly comparable.

The decays $D^+ \to K^-\pi^+\pi^+$, $D^+ \to K^+K^-\pi^+$, and $D_s \to K^+K^-\pi^+$ as well as their resonances have been removed by explicit mass reflection cuts. The remaining modes listed in table 7.3 can be studied with Monte Carlo.

In order to study backgrounds from $D^+ \to \pi^+\pi^+\pi^-$, $D^+ \to K^-\pi^+\pi^-\pi^0$, $\overline{D}^0 \to K^+\pi^+\pi^-\pi^-$, $\overline{D}^0 \to K^+\pi^-\pi^0$, $\overline{D}^0 \to K^+\pi^-$, and $\Lambda_c \to p^+K^-\pi^+$ 100,000 Monte Carlo events of each mode were generated, filtered, stripped, and substripped. The analysis and mass reflection cuts were then applied to each mode and the overall number of events in each Mode was then scaled by $\frac{N_{D^+\to K^-\pi^+\pi^+}(\text{Data})}{N_{D^+\to K^-\pi^+\pi^+}(\text{MonteCarlo})}$.

Table 7.4: DCSD Backgrounds

		Production	Ratio of	
Mode	MC Events	Ratio	Branching Ratios	Events
$\overline{D}^0 \to K^+\pi^+\pi^-\pi^-$	32	2.20	1.00	70
$\overline{D}^0 \to K^+\pi^-$	9	2.20	0.46	9
$D^+ \to \pi^+\pi^+\pi^-$	1	1.00	0.04	0
$D^0 \to K^+\pi^-\pi^0$	4	2.2	1.4	12
$D_s^+ \to \phi e\nu$	16	.2	.2	1
$\Lambda_c \to p^+K^-$	28	.1	.5	1
TOTAL				93

The number of events from each mode is then further scaled by the production ratios (the ratio of the production cross-section of the relevant particle relative to the D^+ production cross-section) and and the branching fraction relative to the $D^+ \to K^-\pi^+\pi^+$ branching fraction. The charm backgrounds that have been Monte Carloed are shown in figures 7.6 and 7.7. The statistics are low but none of these backgrounds appear to peak in the signal region.

7.3.1 Comments on the Background $D_s^+ \to K^+K^-\pi$

The background $D_s^+ \to K^+K^-\pi^+$ is of particular importance. Figure 7.8 shows $\mathrm{M}_{KK\pi}$ plotted along the vertical axis vs. $\mathrm{M}_{K\pi\pi}$ plotted along the horizontal axis. The horizontal lines at 1.94 and 2.00 GeV indicate the D_s^+ mass range. One can see in this region a substantial enchancement over the combinatoric background. These events are particularly pernicious since they have a sharp kinematic limit along the $\mathrm{M}_{K\pi\pi}$ axis just under 1.9 GeV . This is just where the edge of any $D^+ \to K^+\pi^+\pi^-$ signal should fall. This background sharply falling away just below 1.9 GeV creates the illusion of a peak.

The effects of applying successive reflected mass cuts are illustrated in figure

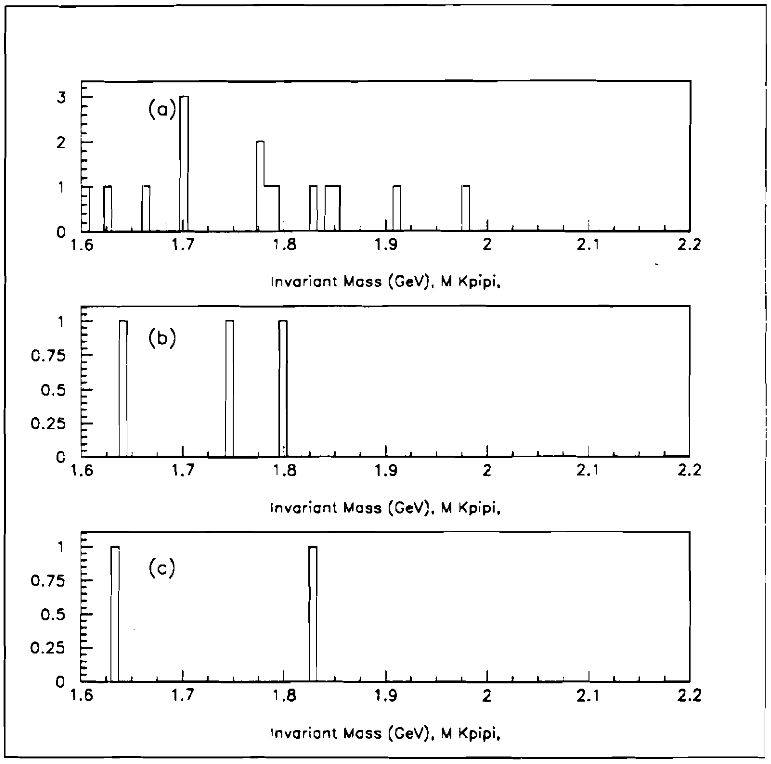

Figure 7.6: Backgrounds from Monte Carlo
a) From $\overline{D^0} \rightarrow K^+\pi^+\pi^-\pi^-$
b) From $\overline{D^0} \rightarrow K^+\pi^-$
c) From $\overline{D^0} \rightarrow K^+\pi^-\pi^0$

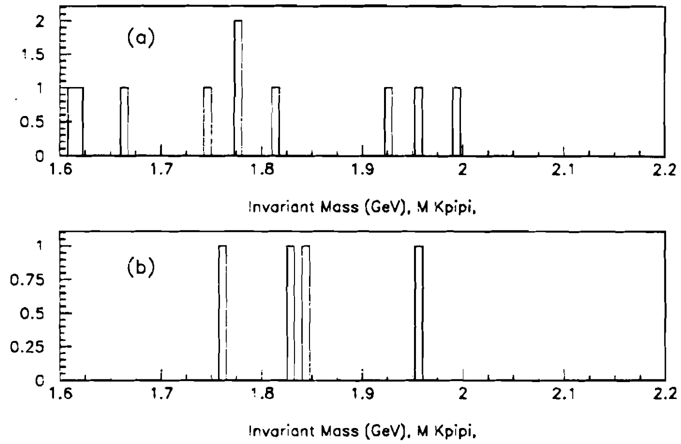

Figure 7.7: Backgrounds from Monte Carlo
a) From $\Lambda_c \rightarrow pK\pi$
b) From $D_s \rightarrow \phi e\nu$

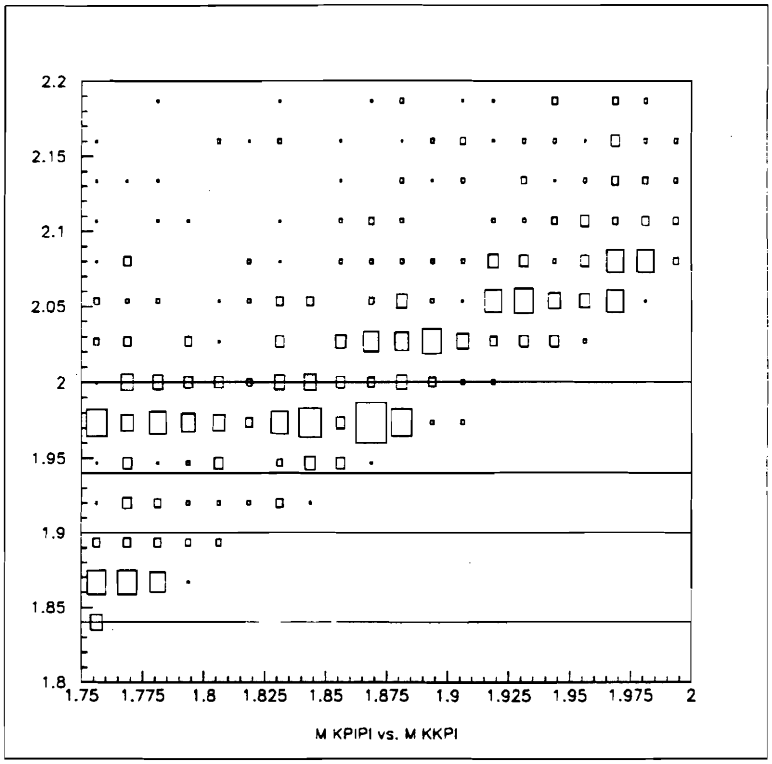

Figure 7.8: M$_{KK\pi}$ (vertically) vs. M$_{K\pi\pi}$ (horizontally)
Horizontal Lines indicate the D_s^+ mass region

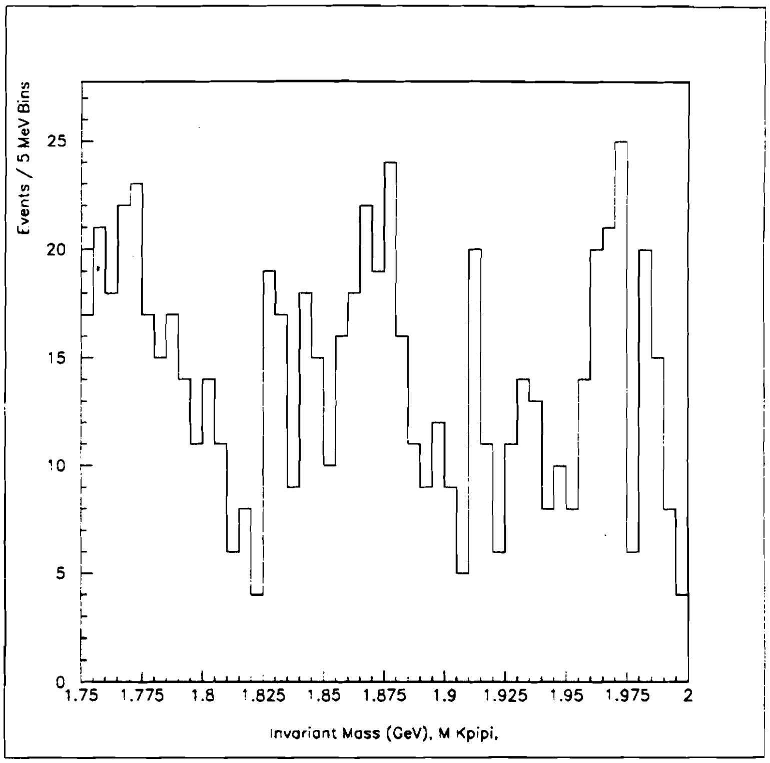

Figure 7.9: $D^+ \to K^+\pi^+\pi^-$ with no mass reflection cuts

7.9 (701 entries in this histogram), figure 7.10 (444 entries), figure 7.11 (391 entries), and figure 7.12 (277 entries).

Figures 7.13 and 7.14 show the efficiency (the ratio of the number of events before and after the D_s^+ mass cut) of the mass reflection cut made to remove $D_s^+ \to K^+K^-\pi^+$. Both the $D^+ \to K^+\pi^+\pi^-$ Monte Carlo figure (7.13) and the $D^+ \to K^-\pi^+\pi^-$ data figure (7.14) predict the efficiency of the $D_s^+ \to K^+K^-\pi^+$ mass reflection cut to be about 75 %.

7.4 The Decay $D_s^+ \to K^+\pi^+\pi^-$

It is prudent to further investigate the peak at the D_s^+ mass in the $K^+\pi^+\pi^-$ mass spectrum in order to make sure it is not the result of charm reflections.

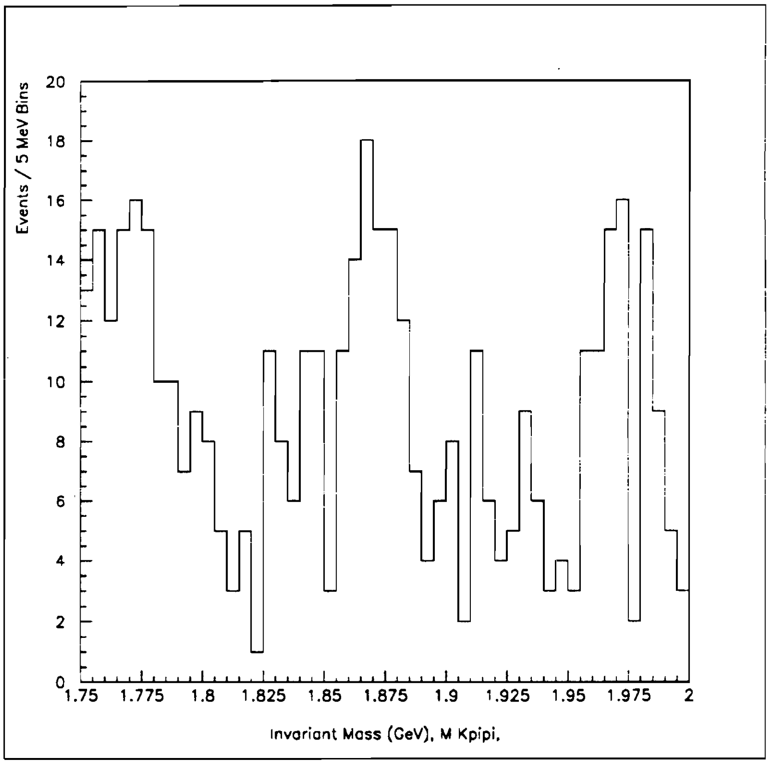

Figure 7.10: $D^+ \rightarrow K^+\pi^+\pi^-$ with one mass reflection cut
$D^+ \rightarrow K^-\pi^+\pi^+$ is removed by mass reflection cut

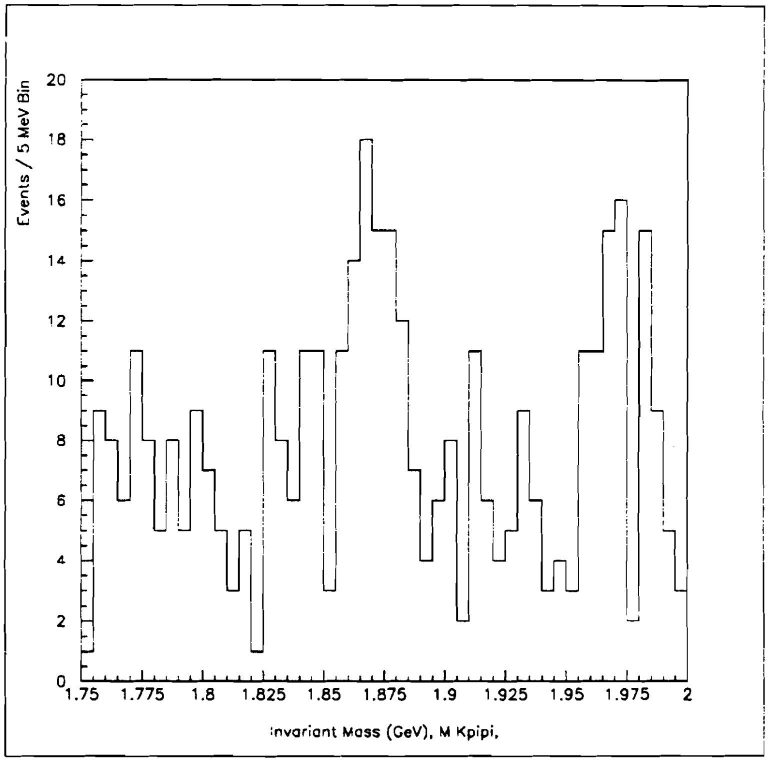

Figure 7.11: $D^+ \rightarrow K^+\pi^+\pi^-$ with two mass reflection cuts
$D^+ \rightarrow K^-\pi^+\pi^+$ and $D^+ \rightarrow K^+K^-\pi^+$
are removed by mass reflection cut

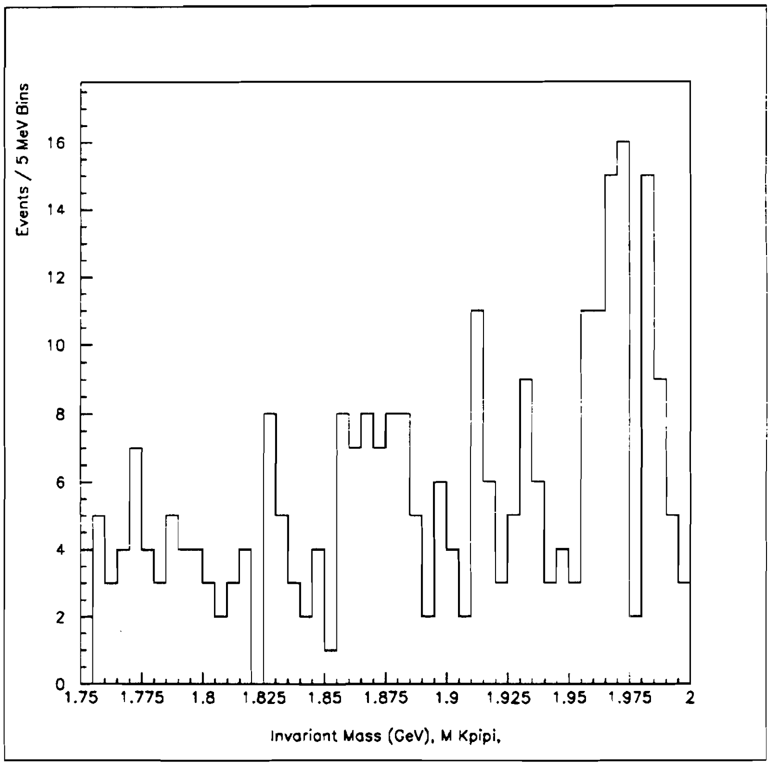

Figure 7.12: $D^+ \rightarrow K^+\pi^+\pi^-$ with three mass reflection cuts
$D^+ \rightarrow K^-\pi^+\pi^+$, $D^+ \rightarrow K^+K^-\pi^+$, $D_s^+ \rightarrow K^-\pi^+\pi^+$
are removed by mass reflection cut

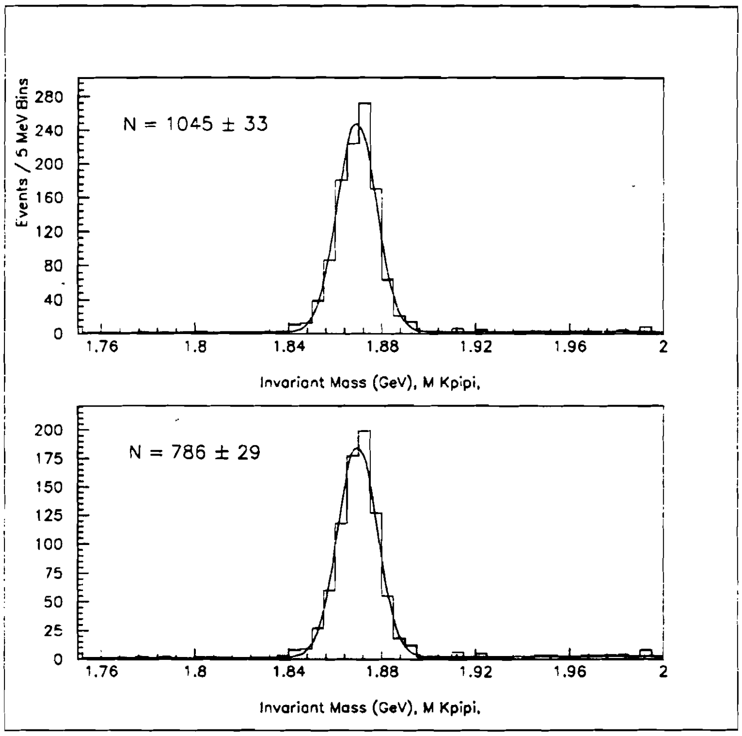

Figure 7.13: $D^+ \rightarrow K^+\pi^+\pi^-$ (Monte Carlo)
Top) Before D_s^+ mass reflection cut
Bottom) After D_s^+ mass reflection cut

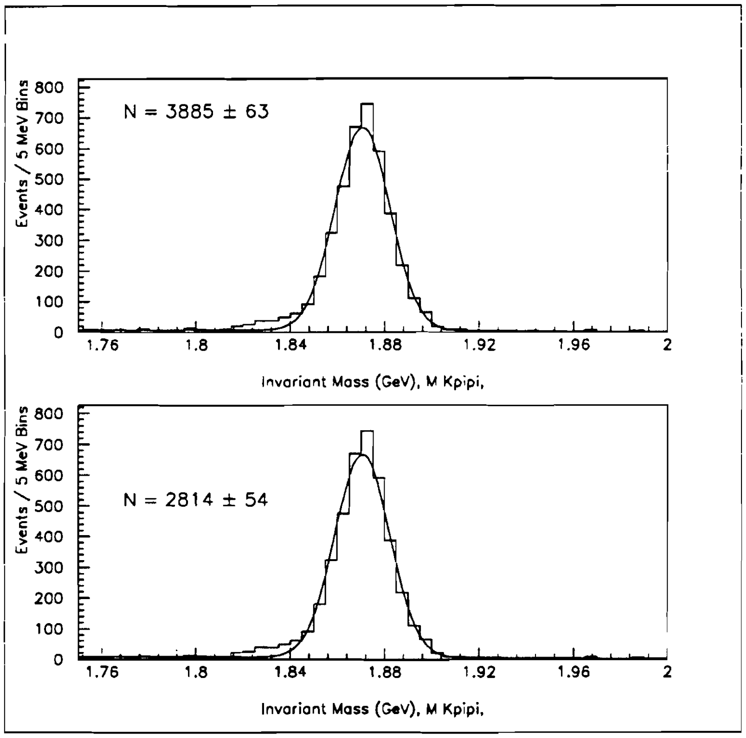

Figure 7.14: $D^+ \rightarrow K^-\pi^+\pi^+$ (Data)
Top) Before D_s^+ mass reflection cut
Bottom) After D_s^+ mass reflection cut

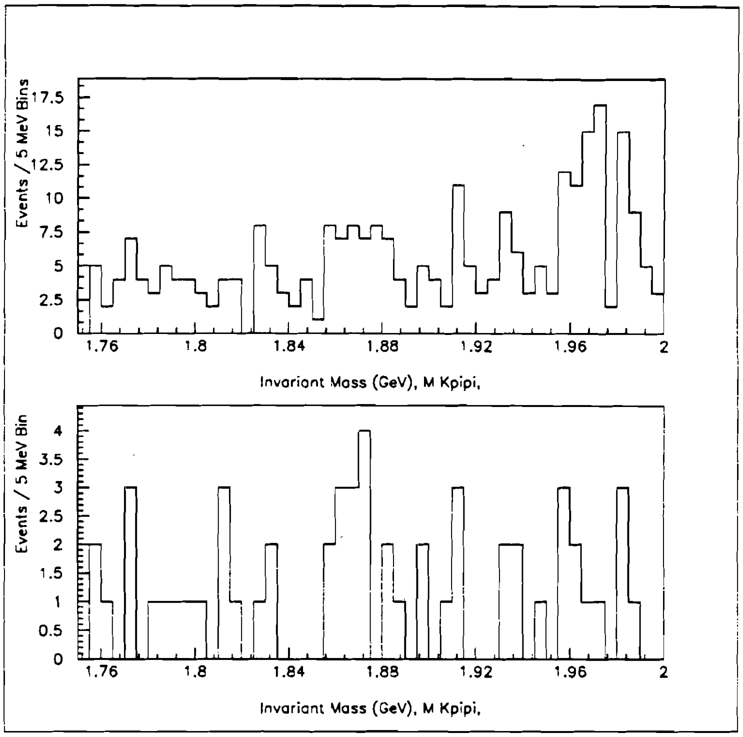

Figure 7.15: Lifetime Cut Applied to $K^+\pi^+\pi^-$ mass spectrum
Top: No cut, Bottom: $\tau > 1.5$ ps

One test is to allow the mass and width of the D_s^+ to float in the fit to the $K^+\pi^+\pi^-$ mass spectrum. This gives $M_{D_s^+} = 1.9700$ GeV and $\sigma_{D_s^+} = 10.7$ MeV.

The lifetime also should be indicative of the D_s^+. Unfortunately, without a calculation of the acceptance function one cannot fit for the lifetime. However, by making a cut on the reduced lifetime one can get a sense that it is shorter than the D^+ lifetime. Figure 7.15 shows the $K^+\pi^+\pi^-$ mass spectrum before and after a 1.5 ps cut on reduced lifetime. While this cut enhances the signal to background of the $D^+ \to K^+\pi^+\pi^-$, it greatly reduces the signal to background of the D_s^+ peak.

Therefore, we conclude that the decay $D_s^+ \to K^+\pi^+\pi^-$ is genuine.

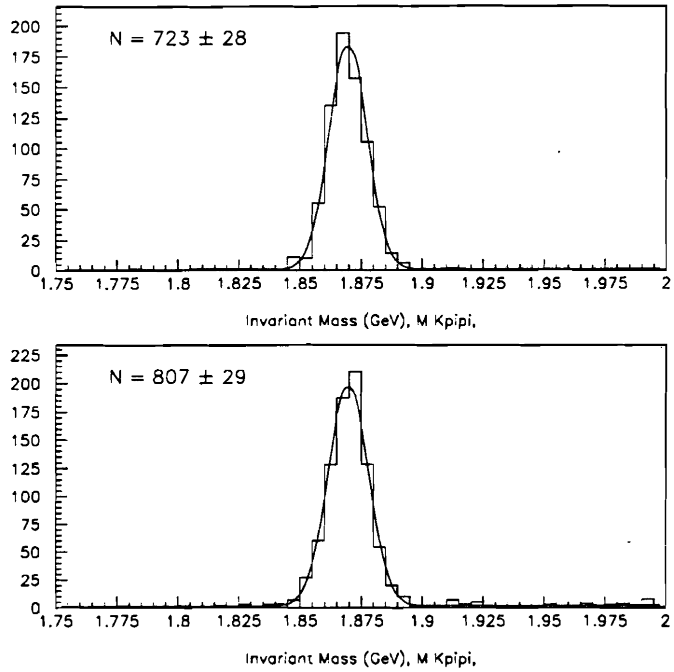

Figure 7.16: Monte Carlo Events run through the Entire Analysis
Top: Cabibbo Favored, Bottom: Doubly Cabibbo Suppressed

7.5 Monte Carlo Consistency Check

The philosophy of this analysis is to avoid using Monte Carlo to study the systematic differences between the $D^+ \to K^-\pi^+\pi^+$ and $D^+ \to K^-\pi^+\pi^+$ samples. However, Monte Carlo can be used to detect any gross errors in assumptions or coding.

In order to check for gross errors 100,000 $D^+ \to K^-\pi^+\pi^+$ and 100,000 $D^+ \to K^-\pi^+\pi^+$ events were generated. The Monte Carlo events were then run through the standard reconstruction, filter, strip, and substrip. The analysis cuts described in section 7.2 were then applied to the output.

The results are presented in figure 7.16. The difference 84 ± 40 is not statistically significant and therefore we conclude that no gross errors have been made.

7.6 Corrections to the Background Shape for Mass Reflection Cuts

The explicit mass reflection cuts made to remove $D^+ \to K^-\pi^+\pi^-$, $D^+ \to K^+K^-\pi^+$, and $D_s^+ \to K^+K^-\pi^+$ backgrounds also remove specific portions of the combinatoric background to $D^+ \to K^+\pi^+\pi^-$. In doing so, the resulting background shape is systematically altered.

For instance, as figure 7.8 illustrates, the mass cut made in order to remove $D_s^+ \to K^+K^-\pi^+$ events also removes combinatoric background, but only for values of $M_{K\pi\pi}$ less than 1.9 GeV. Therefore, the combinatoric background after this reflected mass cut will be systematically lower for masses less than 1.9 GeV.

The effects of the reflected mass cut made to remove the CFD events is illustrated in figure 7.17. The invariant mass of the candidate is plotted assuming $K^-\pi^+\pi^+$ along the vertical axis and $K^+\pi^+\pi^-$ along the horizontal axis. The two horizontal lines in figure 7.17 indicate the mass reflection cut. The relationship between the $M_{K\pi\pi}$ and $M_{\pi\pi K}$ can be calculated exactly

$$M^2_{K\pi\pi} = M^2_{\pi\pi K} + 2[(E1E2 - E1'E2') + (E1E3 - E1'E3') + (E2E3 - E2'E3')] \quad (7.1)$$

where the prime indicates the energies when the mass hypothesis of particles 1 and 3 are exchanged (this means $E2 = E2'$). Equation 7.1 predicts the events in figure 7.17 should be along the diagonal but smeared by the second term. This smearing effect must be large since the $D^+ \to K^-\pi^+\pi^+$ events in the cut out region are smeared across the entire $M_{K^+\pi^+\pi^-}$ axis. In order to obtain the correction to the $D^+ \to K^+\pi^+\pi^-$ mass spectrum, required because of the mass reflection cut the figure 7.17 is fit to a Gaussian $\frac{1}{\sqrt{2\pi\sigma}} e^{\frac{-(M_{K\pi\pi} - M\pi\pi K)^2}{2\sigma^2}}$ along the diagonal in the region

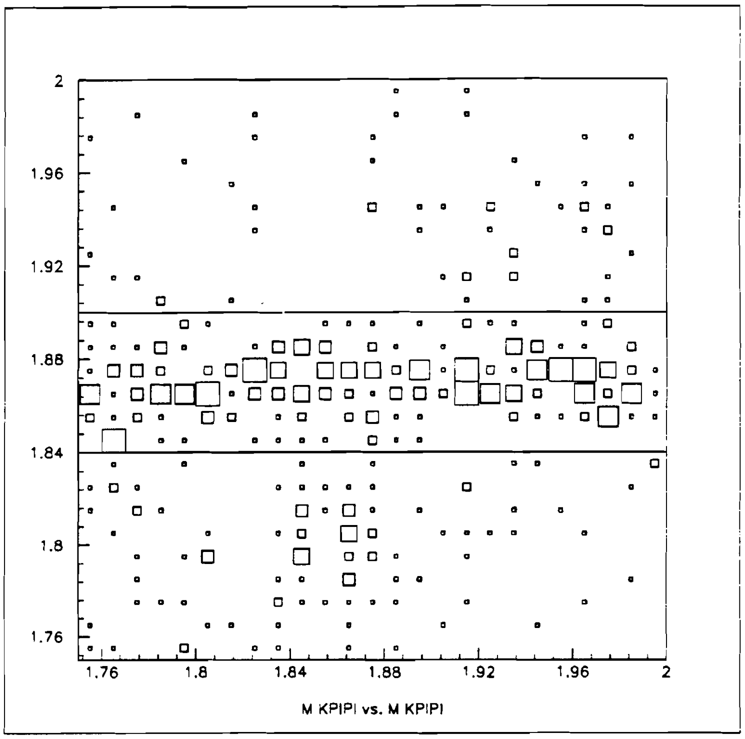

Figure 7.17: $M_{K^-\pi^+\pi^+}$ (vertically) vs. $M_{K^+\pi^+\pi^-}$ (horizontally)
The horizontal lines indicate the $D^+ \rightarrow K^-\pi^+\pi^+$
Mass reflection cut

outside the mass cut. The correction to the background shape resulting from the fit is shown as the shaded region in figure 7.18. A correction derived by fitting a plane to the figure 7.17 is shown in figure 7.19. A linear correction such as that in figure 7.19 will not systematically alter the fitted number of DCSD events. The correction derived from Gaussian hypothesis deviates only slightly from linearity therefore the systematic correction in the fitted number of DCSD events will be very small. Therefore, we ignore the effect of this mass reflection cut on the background shape.

The systematic deformations in the DCSD background shape due to the D_s^+ mass reflection cut will be corrected for by using the $M_{K^+\pi^+\pi^-}$ invariant mass distribution of the events in regions of the $M_{K^+K^-\pi^+}$ distribution. For three prong vertices, one can work out the relationship between $M_{K\pi\pi}$ and $M_{KK\pi}$ to first order

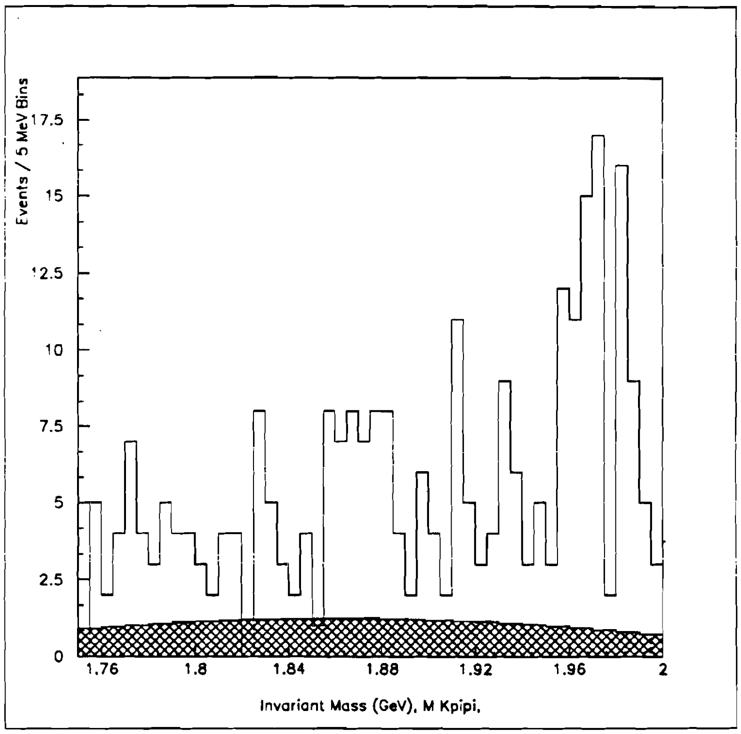

Figure 7.18: Background shape correction for mass reflection cut made to remove $D^+ \rightarrow K^-\pi^+\pi^+$ decays.
From a fit of a Gaussian along the diagonal of figure 7.17

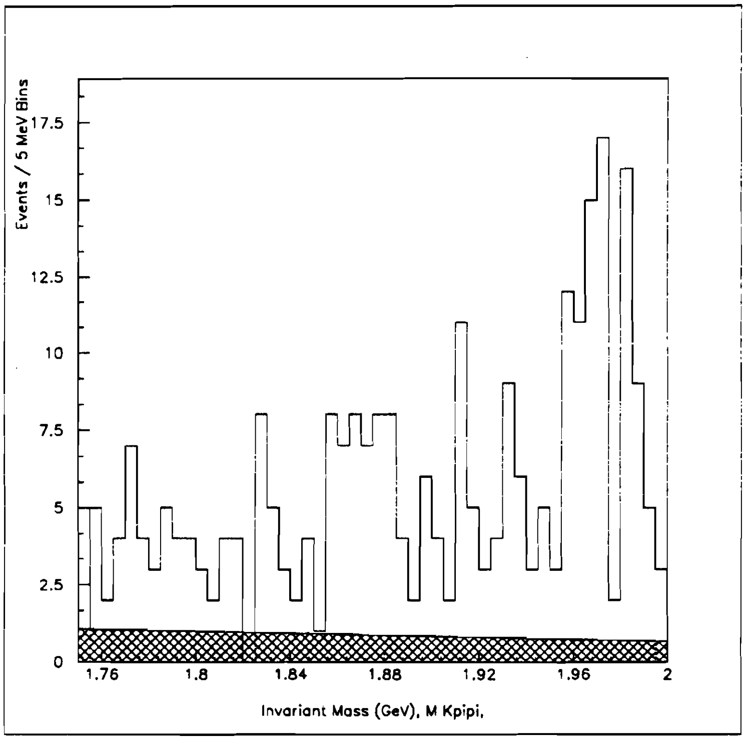

Figure 7.19: Background shape correction for mass reflection cut made to remove $D^+ \rightarrow K^-\pi^+\pi^+$ decays. From a fit of a plane to figure 7.17

in $\frac{m_2}{p_2}$ (it is assumed that $p \gg m$ and that the second particle is the one flipped between pion and kaon). In this case, it is found that

$$M^2_{K\pi\pi} = M^2_{KK\pi} + (m^2_\pi - m^2_K) + \frac{E1 + E3}{p_2}(m^2_\pi - m^2_K) \qquad (7.2)$$

Where m_π and m$_K$ are the rest masses of the pion and kaon respectively, and the indices 1, 2, and 3 refer to the three particles in the vertex (as mentioned before the second particle is the one flipped between pion and kaon). From equation 7.2 it is apparent that even to lowest order the reflection of $KK\pi$ into $K\pi\pi$ depends on the detailed kinematics of the vertex, not just on the masses. Monte Carlo studies indicate (figure 7.20) that the reflection from $KK\pi$ into $K\pi\pi$ is somewhat different for different resonant structure. Therefore, there is no reason to assume that the background events removed have the same M$_{K^+\pi^+\pi^-}$ distribution as the signal plus background events in this region.

Instead, we will obtain the approximate shape of the background spectrum removed, from a two dimensional fit to figure 7.8 excluding the regions in the $D^+, D^+_s \rightarrow K^+K^-\pi^+$ mass windows. In addition, we exclude the $D^+_s \rightarrow K^+\pi^+\pi^-$ mass region. Then fit is then integrated along the M$_{KK\pi}$ axis in the cut out regions and projected onto the M$_{K\pi\pi}$ axis. The correction for the D^+_s mass reflection cut from this two dimensional fit is shown in figure 7.21.

The correction to the $D^+ \rightarrow K^+\pi^+\pi^-$ candidates required because of the $D^+ \rightarrow K^+K^-\pi^+$ mass reflection cut is constructed in an identical manner (via the projection of the two dimensional fit). This correction shown as the shaded events with the raw $D^+ \rightarrow K^+\pi^-\pi^+$ spectrum is shown in figure 7.22.

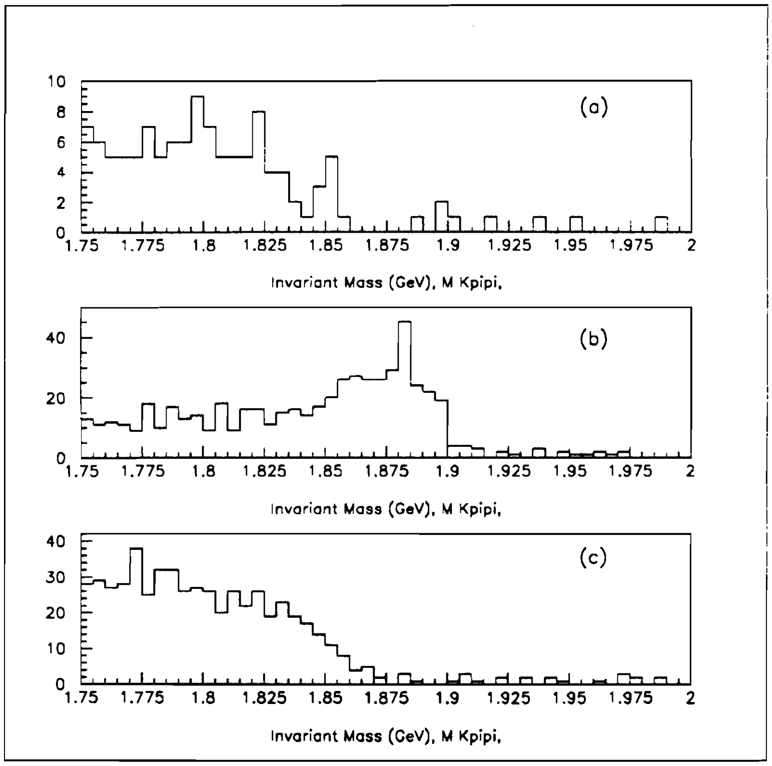

Figure 7.20: $D_s^+ \rightarrow K^+K^-\pi^+$ (MC) reflected into $D^+ \rightarrow K^+\pi^+\pi^-$
(a) Non-resonant, (b) $D_s^+ \rightarrow K^*K^+$, (c) $D_s^+ \rightarrow \phi\pi$

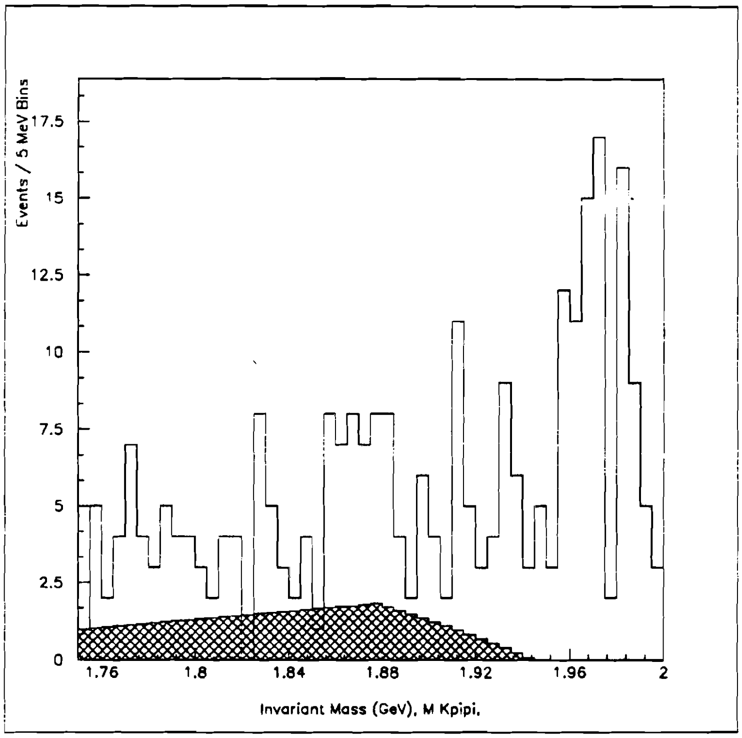

Figure 7.21: $D^+ \rightarrow K^+\pi^+\pi^-$ shaded region is correction needed because of D_s^+ mass reflection cut. The correction is derived from a two dimensional fit to the purely background regions of figure 7.9

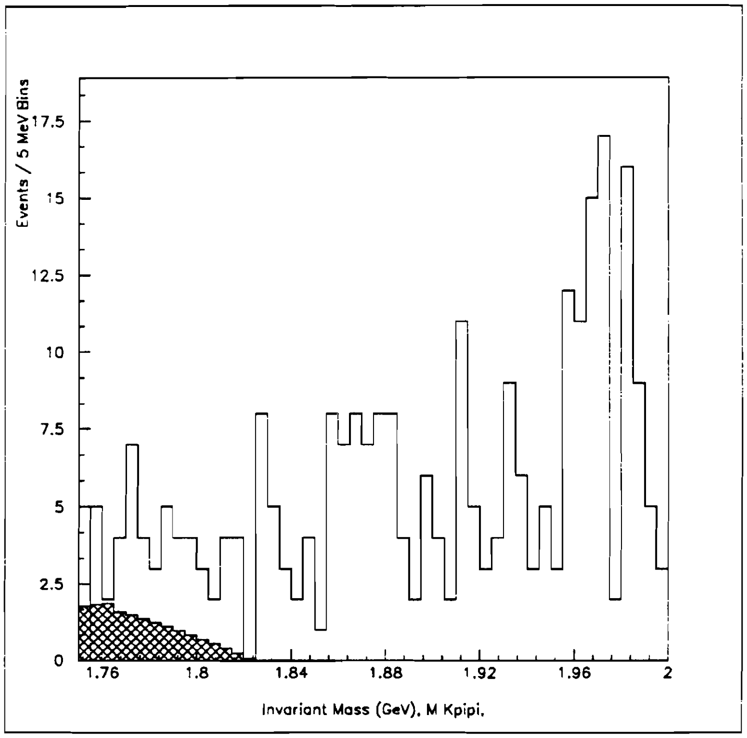

Figure 7.22: $D^+ \rightarrow K^+\pi^+\pi^-$ shaded region is correction needed because of $D^+ \rightarrow K^+K^-\pi^+$ mass reflection cut.

7.7 Simulating the DCSD background shape

The previous sections postulate that the remaining background events in figure 7.12 are combinatoric background. If this is so, it might be possible to simulate the shape of this background by forming an invariant mass distribution from completely uncorrelated tracks. In this section, we describe an attempt to do just that.

The algorithm is as follows. We randomly select a category 7 or category 15 track with a kaon Čerenkov probability greater than .3. We make 10 attempts in an event to find such a track and if no such track is found we proceed to the next event to try to locate a suitable "kaon" track. Once we have the "kaon" we randomly select a category 7 or category 15 track with a pion Čerenkov probability greater than .55 in a subsequent event to be the first "pion". Finally, we randomly select a second "pion" category 7 or category 15 track with a pion Čerenkov probability greater than .55 from a subsequent event so that total charge of the three tracks is ± 1 and that the "kaon" has the same charge as the vertex. Again, if we fail to find such a track after 10 tries in one event we move to the next event. Finally, we generate a invariant mass for these three tracks.

Since, the manner in which we have chosen our three uncorrelated tracks precludes the possibility of them originating from a single vertex, almost none of our analysis cuts can be applied to the resulting candidates. However, we have postulated that the effects of the these analysis cuts on combinatoric background over the scale of .25 GeV should be small (otherwise the assumption of an initially linear background shape certainly wouldn't be true). The shape of the resulting mass distribution therefore tests both the assumption that the remaining background is from combinatorics and that the acceptance for our analysis cuts is not a strong function of mass.

The following figures show the effects of various mass reflection cuts on the simulated background in order to demonstrate that this independent investigation of the background shapes agrees with the others described earlier. First, figure 7.23 shows the raw combinatoric background shape. Figure 7.24 shows this combinatoric background after the mass reflection cut made to remove $D^+ \rightarrow K^-\pi^+\pi^+$ background. This confirms the results of section 7.5, that this mass cut has no dramatic effect on the background shape. Figure 7.25 shows the effects of the mass reflection cut made to remove $D^+ \rightarrow K^+K^-\pi^+$ background. The cutout region in this figure is surprisingly similar to the correction shown in figure 7.22. Figure 7.26 shows the combinatoric background after the $D_s^+ \rightarrow K^+K^-\pi^+$ mass reflection cut is made. Again the similarity of the cutout region to Figure 7.21 is striking. Finally, figure 7.27 shows the simulated background after all mass reflection cuts are applied simultaneously.

7.8 Mass Fits

The invariant mass distributions in this thesis are fit by the unbinned maximum likelihood method.

A hypothesis is made for the CFD candidates that the probability density function for the invariant masses of the candidates is

$$P(M) = \frac{e^{-\nu}\nu^N}{N!} \times f \times S(M) + (1-f) \times B(M)$$

The first term represents the Poisson probability for observing sample size N and it is needed in order to account for the variability in N. The signal function is hypothesized to be a Gaussian.

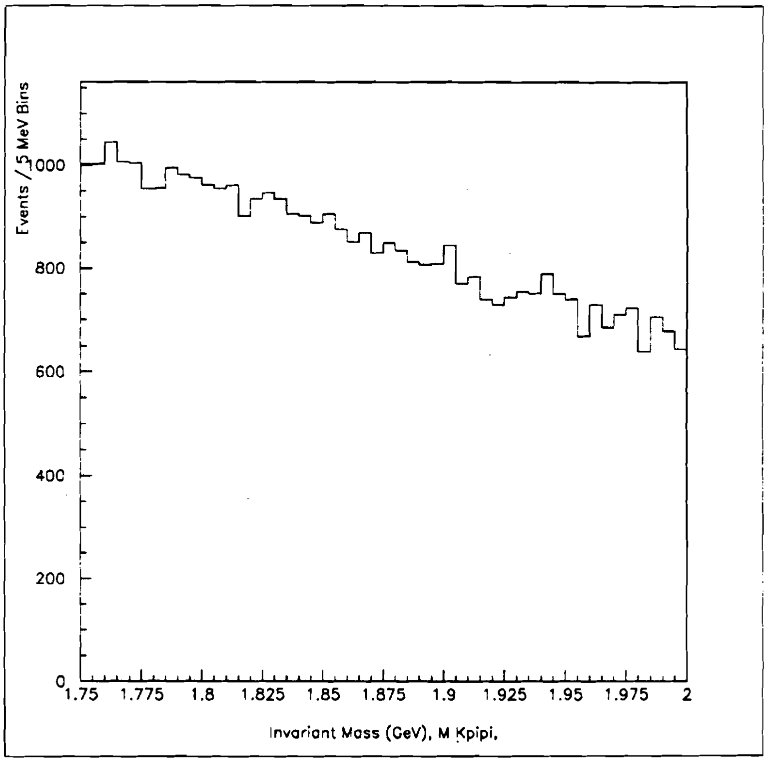

Figure 7.23: Simulated combinatoric $D^+ \rightarrow K^+\pi^+\pi^-$ background

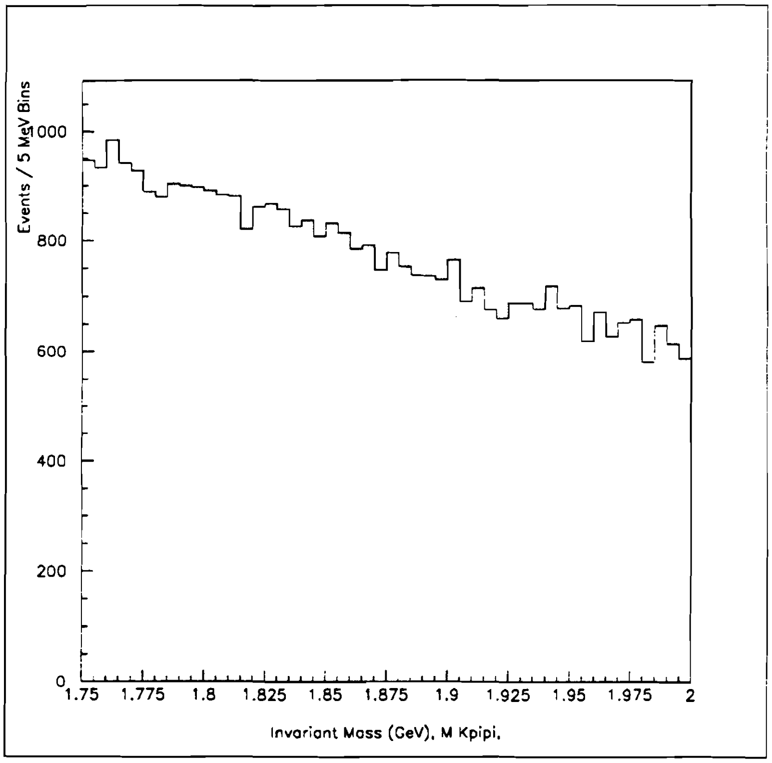

Figure 7.24: Simulated combinatoric $D^+ \rightarrow K^+\pi^+\pi^-$ background
$D^+ \rightarrow K^-\pi^+\pi^+$ mass reflection cut applied

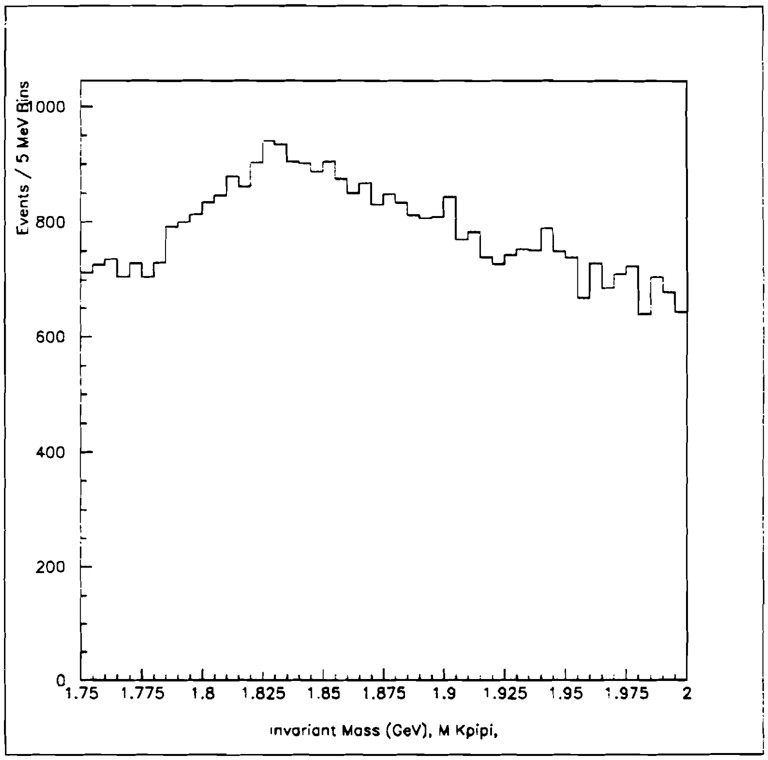

Figure 7.25: Simulated combinatoric $D^+ \to K^+\pi^+\pi^-$ background $D^+ \to K^+K^-\pi^+$ mass reflection cut applied

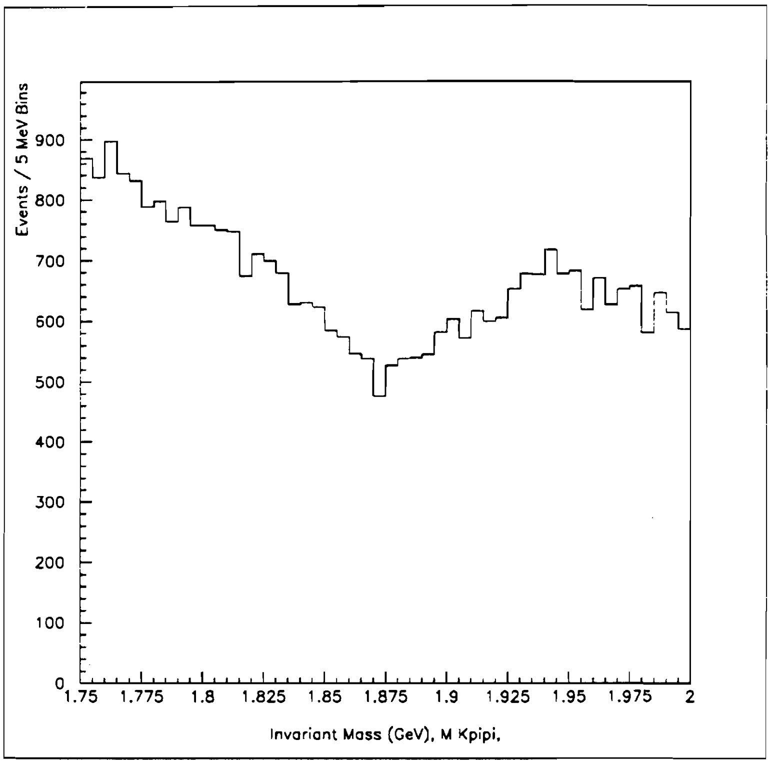

Figure 7.26: Simulated combinatoric $D^+ \rightarrow K^+\pi^+\pi^-$ background $D_s^+ \rightarrow K^+K^-\pi^+$ mass reflection cut applied

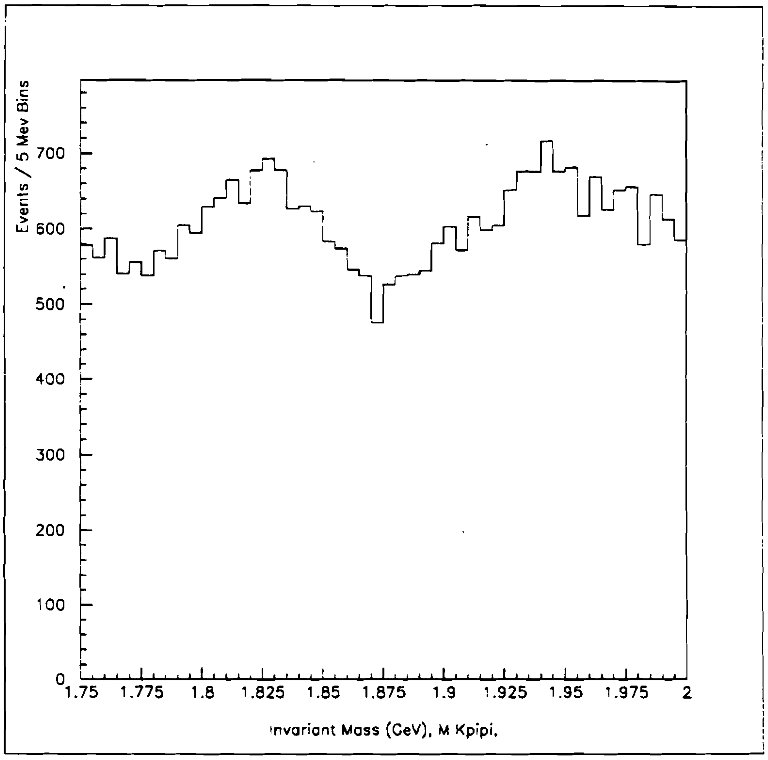

Figure 7.27: Simulated combinatoric $D^+ \to K^+\pi^+\pi^-$ background
All mass reflection cuts applied

Table 7.5: Cabibbo Favored Mass Fit

Parameter	Value	Parabolic Error
f	0.9053	0.0174
$\overline{M}$	1.8716 GeV	0.0002 GeV
σ	0.0115 GeV	0.0002 GeV
SLP	-4.8427	0.7668

$$S(M) = \frac{1}{\sqrt{2\pi}\sigma} e^{-\frac{1}{2}\frac{(M-\overline{M})^2}{\sigma^2}}$$

While the background function is assumed to be linear.

$$B(M) = \frac{1}{Norm}(1 + SLP(M - \overline{M}))$$

For the DCSD candidates two Gaussian signal functions are assumed. One centered at 1.87 GeV for the $D^+ \to K^+\pi^+\pi^-$ decays and one centered at 1.97 GeV for $D_s^+ \to K^+\pi^+\pi^-$ decays. The background function is obtained by fitting a cubic spline to figure 7.27.

For the Cabibbo favored mode the signal fraction, mass, width, and linear slope are all allowed to float. The results of this fit with errors is displayed in table 7.5 and figure 7.28. The fit gives a signal of $N_{CF} = 2813.0 \pm 54.0$ events.

The background shape for the DCSD fit is obtained from simulations described in the previous section. The Gaussian at the D^+ mass is fixed to be the mass and width measured in the CF data. The results of the fit are displayed in table 7.6 and figure 7.29. The mass and width of the D_s^+ are fixed.

The fit to DCSD candidates gives $N_{DCSD} = 27.3 \pm 7.9$. Figure 7.31 shows the background subtracted signal, the error bars are the square root of the entries in figure 7.29.

One also fits for N_{DCSD} using the background shape obtained assuming the

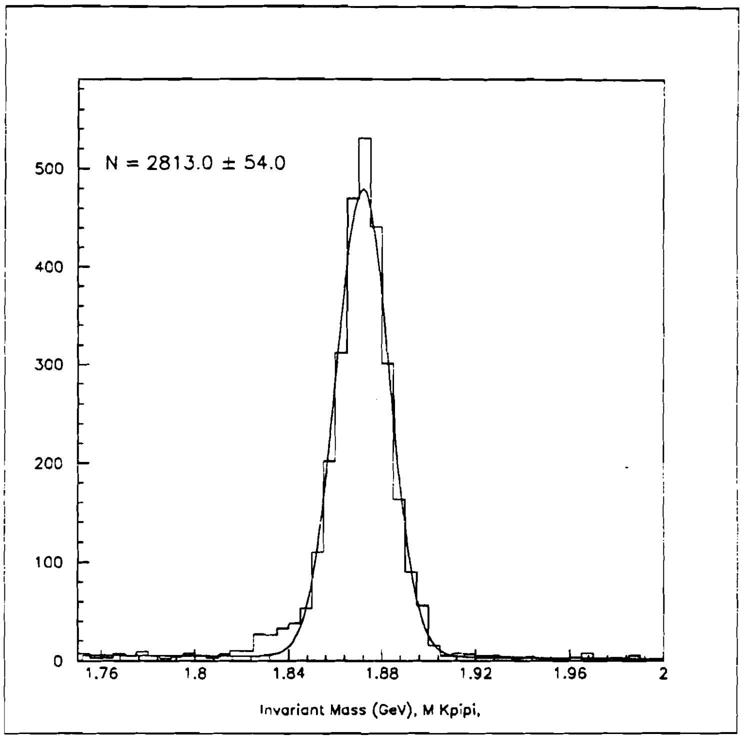

Figure 7.28: Fit to Cabibbo Favored Data

Table 7.6: Doubly Cabibbo Suppressed Mass Fit

Parameter	Value	Parabolic Error
f_{D^+}	0.0986	0.2850
M_{D^+}	1.8716 GeV	fixed
σ_{D^+}	0.0115 GeV	fixed
$f_{D_s^+}$	0.1920	0.3658
$M_{D_s^+}$	1.9700 GeV	fixed
$\sigma_{D_s^+}$	0.0108	fixed

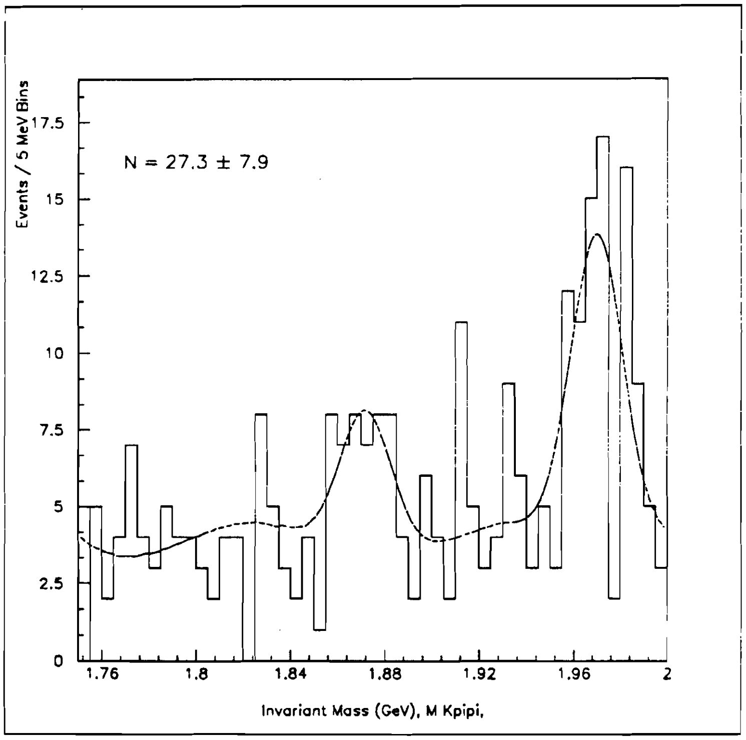

Figure 7.29: Fit to Doubly Cabibbo Suppressed Data Background Shape from Figure 7.27

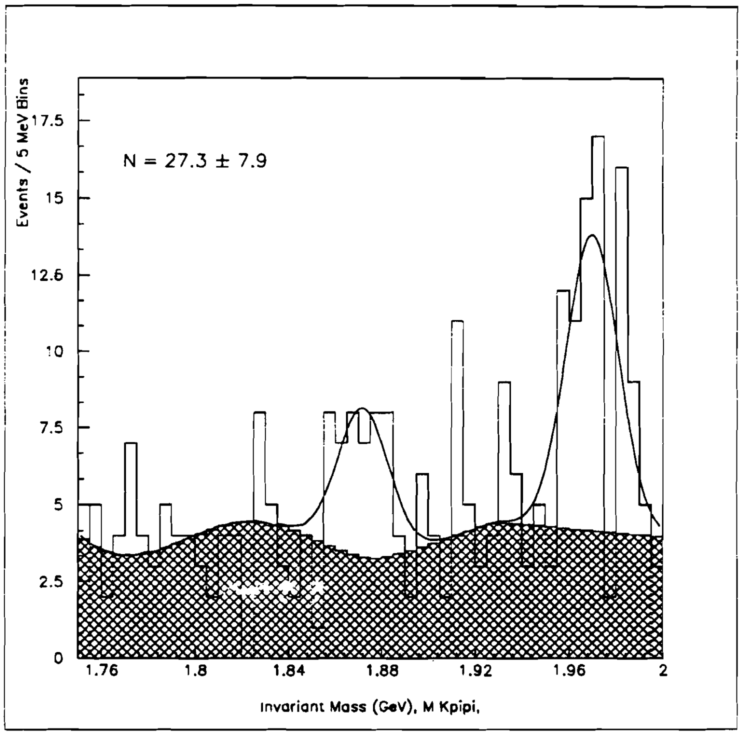

Figure 7.30: Fit to Doubly Cabibbo Suppressed Data
Background shape from figure 7.27
Shaded region is the background shape

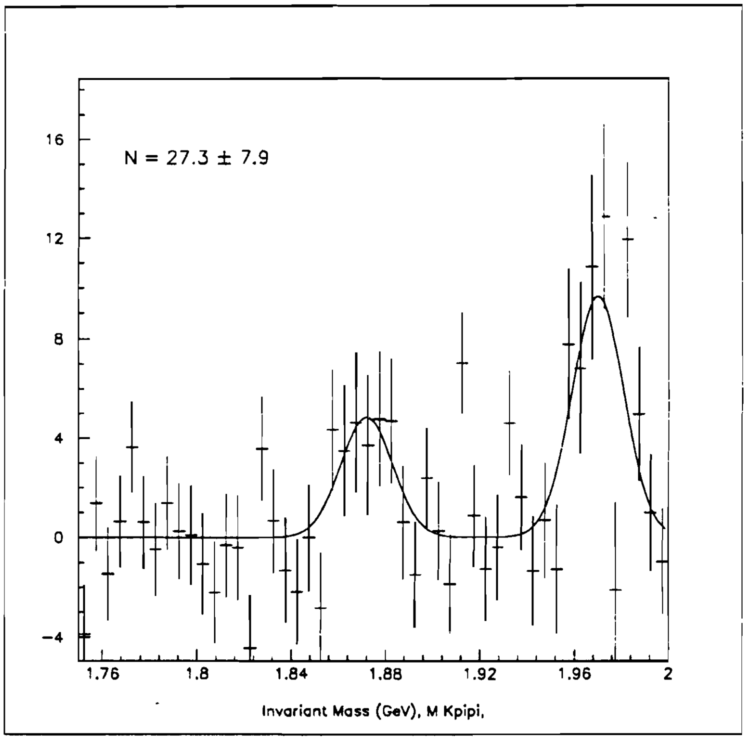

Figure 7.31: Fit to Doubly Cabibbo Suppressed Data
Background subtracted data
The Error Bars are the from 7.29

Table 7.7: Doubly Cabibbo Suppressed Mass Fit

Parameter	Value	Parabolic Error
f_{D^+}	0.0888	0.0283
M_{D^+}	1.8716 GeV	fixed
σ_{D^+}	0.0115 GeV	fixed
SLP	-1.0245	0.9421
$f_{D_s^+}$	0.1664	0.0395
$M_{D_s^+}$	1.9700 GeV	fixed
$\sigma_{D_s^+}$	0.0108	fixed

background was a straight line minus the corrections for the two dimensional fit to figure 7.8. The sizes of these corrections are not allowed to float as they are determined uniquely from the fit. Table 7.7 and figure 7.32 show the results of this fit. This fit gives $N_{DCSD} = 24.6 \pm 7.9$

7.8.1 Quality of Fits

One measure of the quality of an unbinned likelihood fit is the Kolmogorov-Smirnoff test. This test essentially determines the maximum deviation between the cumulative probability distribution of the fit and the observed cumulative probability distribution of the data([Fr79]).

For the fit to the DCSD with the simulated background shape the maximum deviation is found to be 3.6 %. For the fit to the DCSD with the "2-D Fit" background shape the maximum deviation was found to be 5.0 % For 277 events the maximum deviation necessary to falsify the fit at the 80 % confidence level (ie. there is only a 20 % chance of getting a larger deviation) is 6.4 % ([Fr79]). Therefore, we can accept both of these fits.

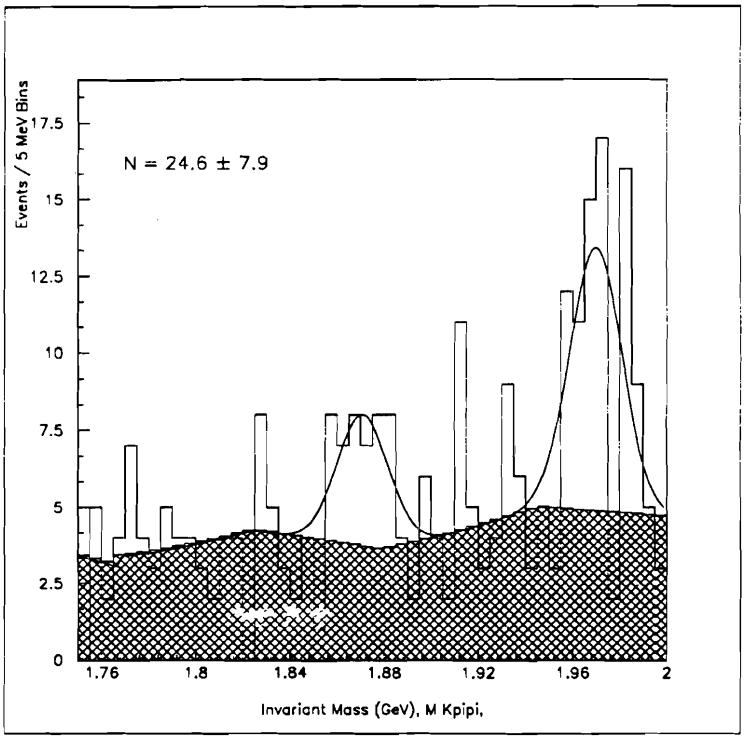

Figure 7.32: Fit to Doubly Cabibbo Suppressed Data
Background Shape: Straight line minus 2-D Fit Corrections

Table 7.8: N_{DCSD} under permutation of MC and shape corrections

	"Simulated' BKG Shape	"2-D Fit" BKG Shape
	27.3	24.6

7.9 Systematic Error due to Background Shape

The amount of measured DCSD signal is critically dependent on the background shape. Since we have determined the DCSD background shape in numerous ways we can use them to determine the systematic error due to uncertainty in the background shape. Table 7.8 contains the fit values for N_{DCSD} given alternate assumptions about the background shape. Column labeled "Simulated" background shape indicates the background was assumed to have the shape of a cubic spline fit to figure 7.27. The column labeled "2-D" fit BKG Shape is the shape obtained by assuming the background was a straight line minus the corrections from the two dimensional fit to figure 7.8. The sizes of these corrections are not allowed to float as they are determined uniquely from the fit. The difference between the two values, 2.7 events is the systematic error due to uncertainty in the background shape.

7.10 Systematic Difference due to Kaon identification

One difference between the Cabibbo favored and the doubly Cabibbo suppressed samples is the way in which the kaon is identified. For the Cabibbo favored data the particle called the kaon is the one which has a charge opposite of the $D^{\pm}$ candidate. For real Cabibbo favored decays of the charged D mesons the efficiency of this identification is 100%. The kaon identification for the doubly Cabibbo suppressed sample is somewhat different. The kaon is the particle with the largest kaon Čerenkov probability that has the same sign as the $D^{\pm}$ candidate. The requirement that the kaon as identified by charge, in the CFD sample, have a greater kaon Čerenkov probability than the first pion in the decay can be used to measure the efficiency of the kaon identification for the DCSD decays.

The requirement that the kaon Čerenkov probability of the kaon be greater than the kaon Čerenkov probability of the first pion is made on the CFD data and the results are shown in figure 7.33 The fit to this sample yields $N_{\mathrm{ckvcut}} = 2790 \pm 54$ which gives an efficiency (compared to the nominal $D^+ \rightarrow K^-\pi^+\pi^-$ sample of figure 7.28).

$$\epsilon_{\mathrm{ckvcut}} = .990 \pm .002$$

It is not surprising that this efficiency is very high. In order for a real kaon to fail this test, not only must the kaon Čerenkov probability of the first pion be greater than that of the kaon, it also must be greater than .3.

7.11 Systematic Differences due to Resonant Substructure

The decays $D^+ \rightarrow K^+\pi^+\pi^-$ and $D^+ \rightarrow K^-\pi^+\pi^+$ have different resonant substructure. If the acceptance is a strong function of an event's position on the dalitz plot then it may be that the DCSD and CFD decays have different acceptance due to different resonant substructure.

The way this is investigated is to use non-resonant $D^+ \rightarrow K^-\pi^+\pi^+$ Monte Carlo. The dalitz plot is constructed from the truth table and from accepted events.

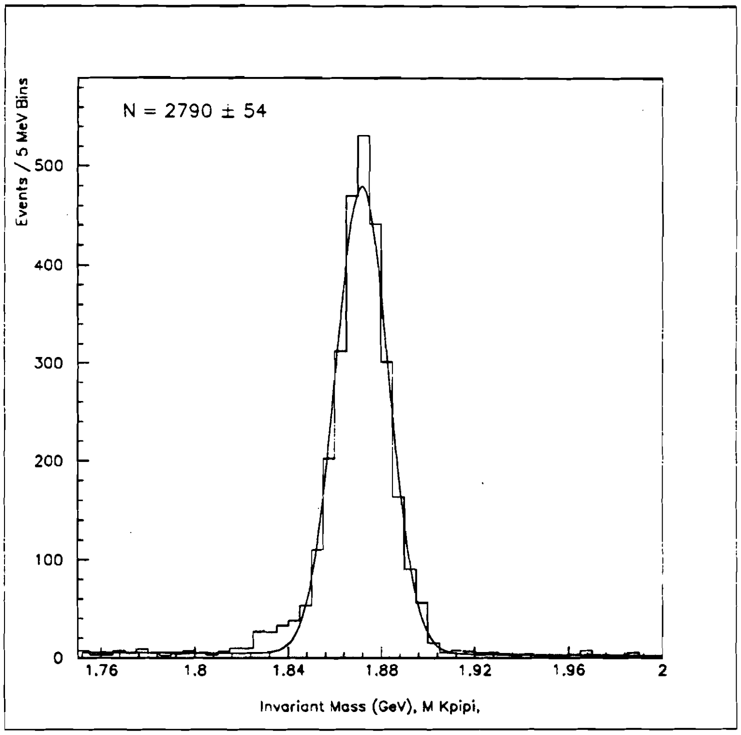

Figure 7.33: Fit to Cabibbo Favored Data
CKV Probability of K > CKV Probability of π

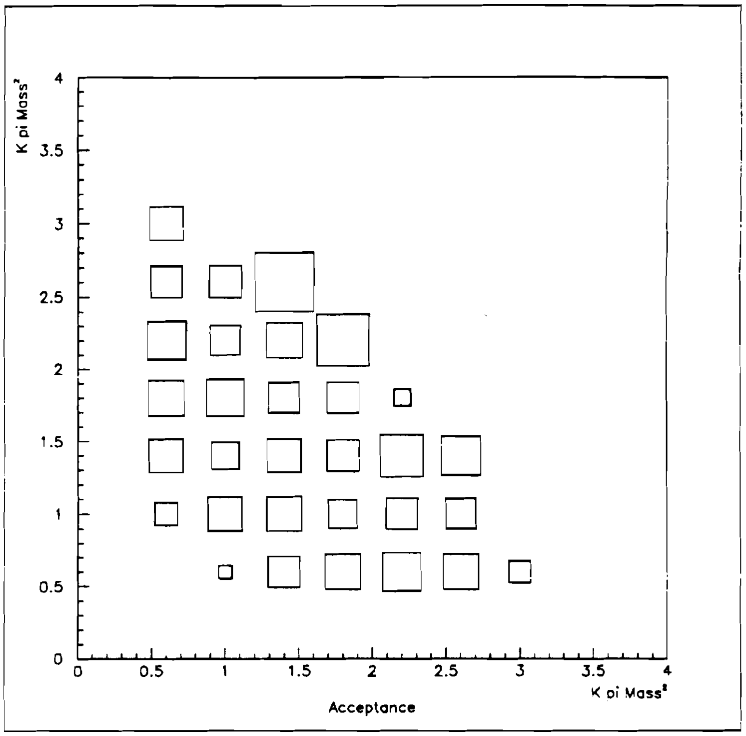

Figure 7.34: Acceptance
$M^2_{K\pi}$ vs. $M^2_{K\pi}$

We can then form an acceptance function. Except for regions along the edge of the dalitz plot (which are dominated by statistics) the acceptance function is essentially flat. We used the variance of the bins as a measure of the error in the flatness of the Dalitz and plot and therefore, possible error in the acceptance due to resonant substructure.

Figure 7.34 shows the acceptance across the Dalitz Plot. Ignoring, the low statistics bins around the edges, the mean of the acceptance is 15 % and the standard deviation of the acceptance is 1 %. (The acceptance is high because the study is done with Monte Carlo that has been filtered, stripped, and substripped.) Therefore, we do not assign any systematic error due to differing acceptances in resonant substructure.

7.12 $D^+ \rightarrow K^+\pi^+\pi^-$ Branching Fraction

The principal systematic errors in this analysis are the uncertainty in the DCSD background shape and the uncertainty in the kaon identification efficiency. Summing them in quadrature gives a total systematic error of 11.1 %.

We choose the "2-D Fit" background shape as our central value since it is determined directly from the data. Therefore, the amount of DCSD signal corrected for the efficiency of the Kaon identification is

$$\mathrm{N_{DCSD}} = \frac{24.6 \pm 7.9 \pm 2.7}{\epsilon_{\mathrm{ckvcut}}} = 24.8 \pm 8.0 \pm 2.7$$

Where the first error is statistical and the second systematic.

The ratio of the branching fractions is

$$\frac{\Gamma(D^+ \rightarrow K^+\pi^+\pi^-)}{\Gamma(D^+ \rightarrow K^-\pi^+\pi^+)} = \frac{24.8 \pm 8.0 \pm 2.7}{2813.0 \pm 54.0} = .0089 \pm .0028 \pm .0011$$

7.13 Lifetime Consistency Check

Instead of removing the dangerous $D_s^+ \rightarrow K^+K^-\pi^+$ contamination through an explicit mass reflection cut one can try using the short D_s^+ lifetime to separate D^+ from D_s^+. Following the work of Alberto Reis [Re94] we attempt to remove the $D_s^+ \rightarrow K^+K^-\pi^+$ by requiring our DCSD candidates to have a lifetime greater than 1.2 D^+ lifetimes (note this is a cut on the lifetime not the reduced lifetime).

Therefore the nominal analysis cuts (Table 7.1) and the additional requirement that the candidates have a lifetime greater the 1.2 D^+ lifetimes are placed on the DCSD candidates. The reflection of $D^+ \rightarrow K^+\pi^-\pi^+$ into $K^+K^-\pi^+$ is shown in figure 7.35.

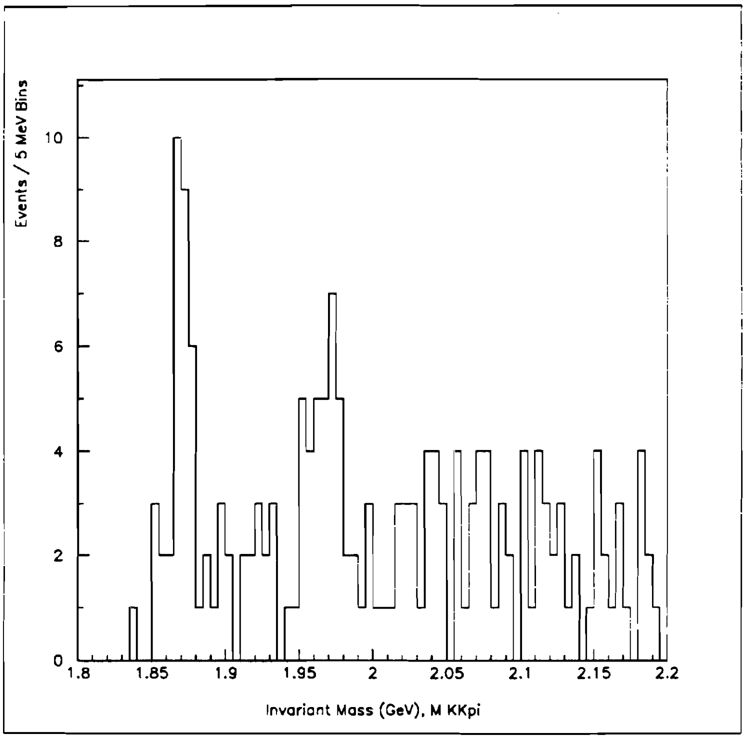

Figure 7.35: $D^+ \rightarrow K^+\pi^+\pi^-$ reflected into $K^+K^-\pi^+$
Standard Analysis Cuts, Lifetime $> 1.2 \times \tau_{D^+}$

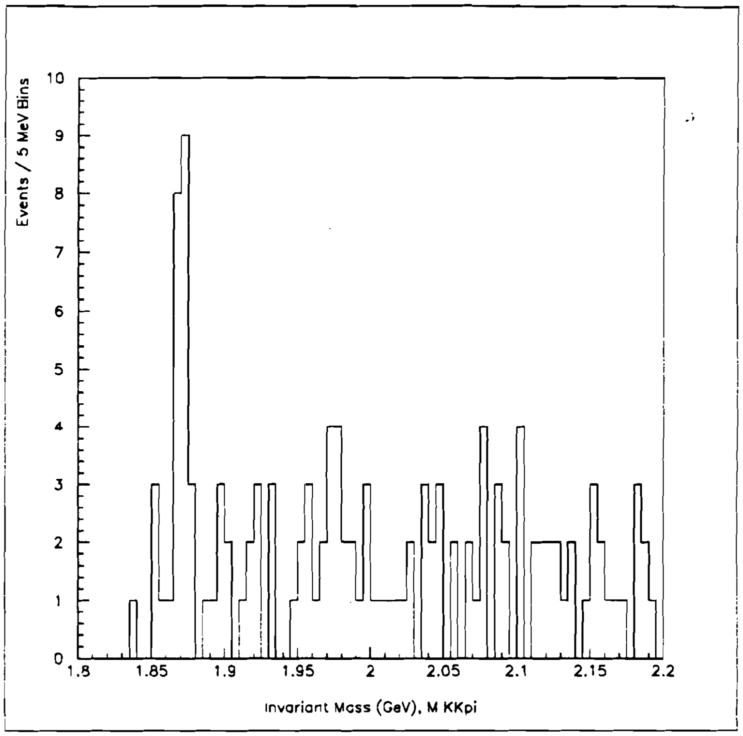

Figure 7.36: $D^+ \to K^+\pi^+\pi^-$ reflected into $K^+K^-\pi^+$
Standard Analysis Cuts, Lifetime $> 1.2 \times\tau_{D^+}$
π Čerenkov probability $> .8$

One can still see a significant D_s^+ contamination in this sample. Therefore, we also require the pion Čerenkov probabilities to be greater than .8. The resulting charm contamination is shown in figure 7.36. There still is a small visible $D_s^+ \to K^+K^-\pi^+$ signal. The charm backgrounds $D^+ \to K^-\pi^+\pi^-$ and $D^+ \to K^+K^-\pi^+$ are removed by explicit mass reflection cuts (discarding events that have a $K^-\pi^+\pi^+$ or $K^+K^-\pi^+$ mass between 1.84 and 1.9 GeV).

Finally, figures 7.37, 7.38 show the $D^+ \to K^-\pi^+\pi^+$ and $D^+ \to K^+\pi^+\pi^-$ candidates with these analysis cuts applied.

Fitting the DCSD candidates to a straight line plus two Gaussians gives $N_{DCSD} = 18.2 \pm 6.3$. Fitting the $D^+ \to K^-\pi^+\pi^+$ candidates gives $N_{CFD} = 2005 \pm 46$. We still need to account for the 6 ± 4 $D_s^+ \to K^+K^-\pi^+$ events that are present in the

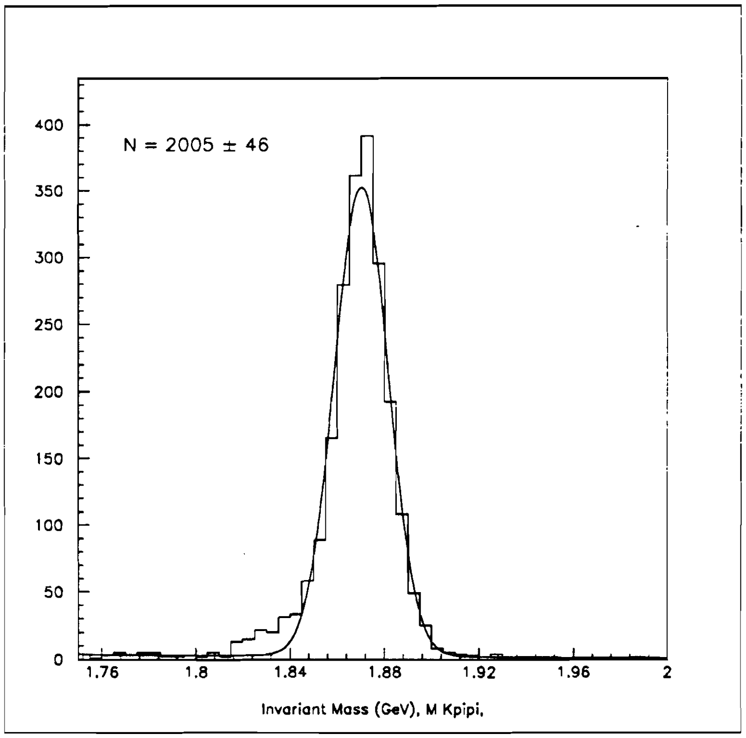

Figure 7.37: $D^+ \to K^-\pi^+\pi^+$, Lifetime $> 1.2 \times \tau_{D^+}$
π Čerenkov probability $> .8$
$D^+ \to K^+\pi^+\pi^-$ and $D^+ \to K^+K^-\pi^+$ are removed by mass reflection cuts

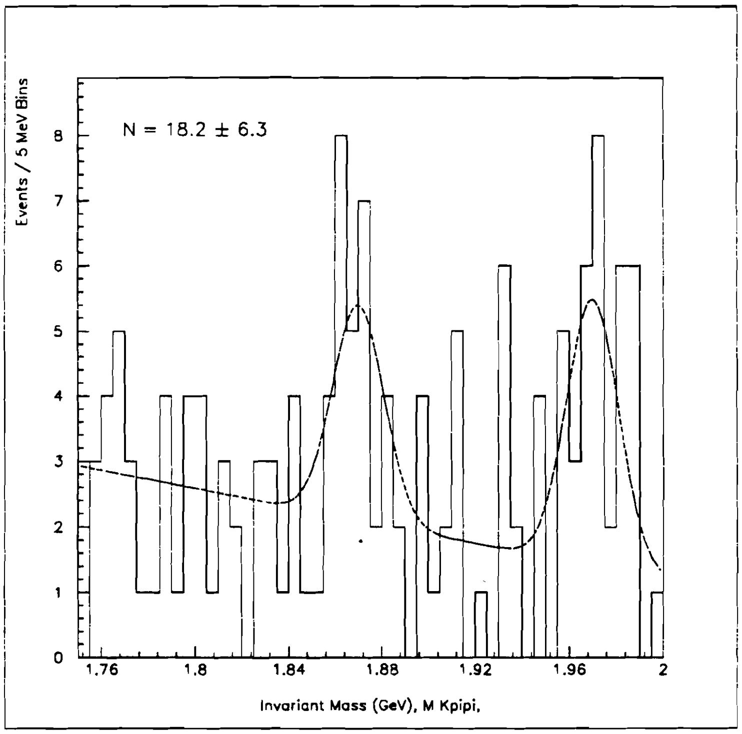

Figure 7.38: $D^+ \rightarrow K^+\pi^+\pi^-$, Lifetime $> 1.2 \times\tau_{D^+}$
π Čerenkov probability $> .8$
$D^+ \rightarrow K^+\pi^+\pi^-$ and $D^+ \rightarrow K^+K^-\pi^+$ are removed by mass reflection cuts

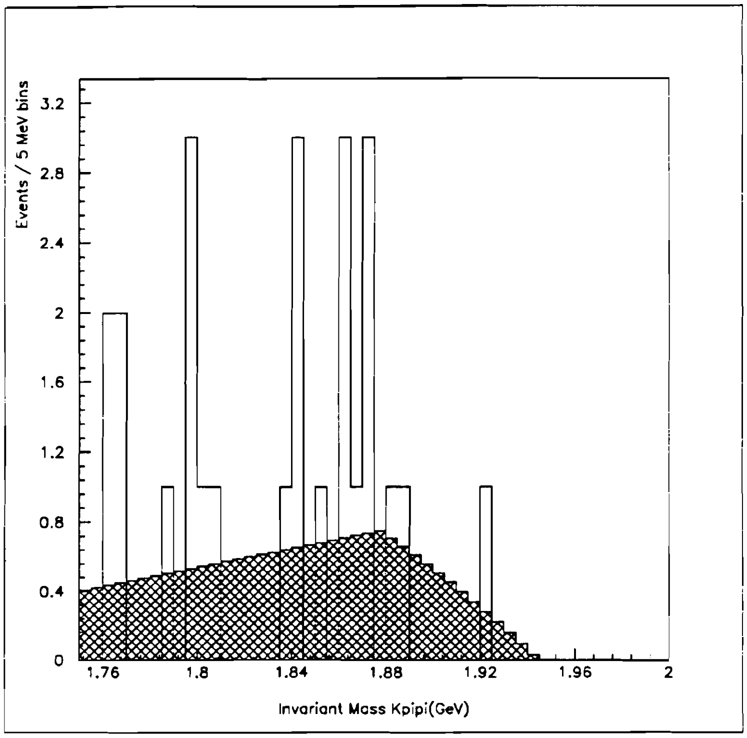

Figure 7.39: Histogram: Events with 1.94 < $M_{KK\pi}$ < 2.0 reflected into $K^+\pi^+\pi^-$
Shaded: The Combinatoric background

DCSD background. Figure 7.39 shows the $K^+\pi^+\pi^-$ distribution of events that have a $K^+K^-\pi^+$ invariant mass between 1.94 and 2.0 GeV. The dashed histogram is the shape of the combinatoric background extracted from a 2-D fit to the $K\pi\pi$ - $KK\pi$ plane (a procedure identical to that in section 7.6 was used). The excess of events over the combinatoric background within two sigma of the center of signal region, between 1.85 and 1.89 GeV is 3.7 ± 3.2 events (the error is taken to be the square root of the total number of events in this region). Subtracting this excess of events gives $N_{DCSD} = 14.5 \pm 6.3 \pm 3.2$, where the second error is due to the statistical uncertainty in the number of excess events.

This implies a branching ratio of approximately

$$\frac{\Gamma(D^+ \to K^+\pi^+\pi^-)}{\Gamma(D^+ \to K^-\pi^+\pi^+)} = .0072 \pm .0032 \pm .0019$$

which is consistent with our earlier result.

7.14 Resonant Doubly Cabibbo Suppressed Decays

The D^+ can also decay to $K^+\pi^+\pi^-$ through resonances. It may be that by confining the decay products to be on the resonant mass shell, the background will be suppressed enough to enhance the significance of the signal.

We have considered these resonant doubly Cabibbo suppressed decays, $D^+ \to K^+\rho^0$ and $D^+ \to K^*\pi^+$. Since $\Gamma_\rho \approx 150$ MeV there is not much chance of observing $D^+ \to K^+\rho^0$. However, $\Gamma_{K^*} \approx 50$ MeV. One can try constraining the Kaon and the oppositely charged pion in the $D^+ \to K^+\pi^+\pi^-$ decay to lie within 2σ of the K^* mass (between 840 and 945 MeV). In addition, because of angular momentum considerations the cosine of the angle between the K$^+$ and the π^+ in the K^* rest frame should be distributed as $cos^2\theta$. A cut requiring $|cos\theta| > .5$ was made. This cut should retain 87.5 % of the signal. Figure 7.40 shows the $D^+ \to K^+\pi^-\pi^+$ candidates when the K^* mass and $cos\theta$ requirements were made.

Correcting for the efficiency of kaon identification in the DCSD and the 87.5 % efficiency of the $cos\theta$ cut and the 90 % efficiency of the 2σ mass cut gives N$_{D^+\to K^*(892)\pi^+}$ = $14.0 \pm 4.8 \pm 0.9$ The systematic error is from the uncertainty in background shape. Both the spline background and a simple linear background were used in a fit to the $D^+ \to K^*(892)\pi^+$ candidates. This shows the insensitivity of the signal size to background shape even at these modest signal to background ratios.

The Branching fraction of $K^*(892) \to K^+\pi^-$ is $\frac{2}{3}$ (obtained from isospin conservation).

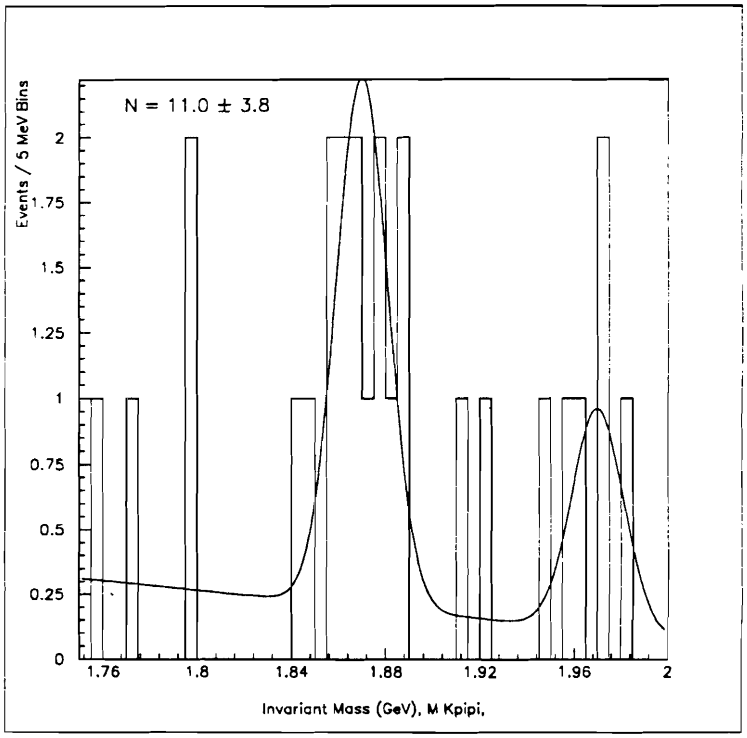

Figure 7.40: $D^+ \rightarrow K^*(892)\pi^+$

This gives a limit

$$\frac{\Gamma(D^+ \to K^*(892)\pi^+)}{\Gamma(D^+ \to K^-\pi^+\pi^+)} = \frac{14.0 \pm 4.8 \pm .9}{2813.0 \pm 54.0} < .0072 \times 1.5 = .0108 \text{ @ } 90\% \text{ CL}$$

or

$$\frac{\Gamma(D^+ \to K^*(892)\pi^+)}{\Gamma(D^+ \to K^-\pi^+\pi^+)} \times \frac{1}{tan^4\theta_c} < 4.3 \text{ @ } 90\% \text{ CL}$$

Chapter 8

Search for $D^+ \rightarrow K^+K^+K^-$

8.1 Introduction

Another three prong doubly Cabibbo suppressed decay of the D^+ is $D^+ \rightarrow K^+K^+K^-$. One need not draw the Feynman diagram to see that this is doubly Cabibbo suppressed. It is enough to observe that it is a $\Delta C = -1$, $\Delta S = +1$ decay.

Nevertheless, it is interesting to draw the diagram for the decay $D^+ \rightarrow K^+K^+K^-$. As figure 8.1 shows the only way this decay can proceed through a spectator diagram is via final state rescattering. This phenomena may enhance the partial width of this decay.

In this chapter, an analysis similar to the analyses in the previous chapter is performed on the decay $D^+ \rightarrow K^+K^+K^-$ and the resonant decay $D^+ \rightarrow K^+\phi$. The same tighter analysis cuts (Table 7.1) were applied to the results of the $D^+ \rightarrow K^+K^+K^-$ substrip,except that the Kaon Čerenkov probability cut was relaxed to .2, the DIP cut was relaxed to 40 μ, ,the SDZ cut was relaxed to 12, and only Category 7 and 15 tracks were used. Also, additional Kaon Čerenkov probability cuts were applied to the other kaons in the decay.

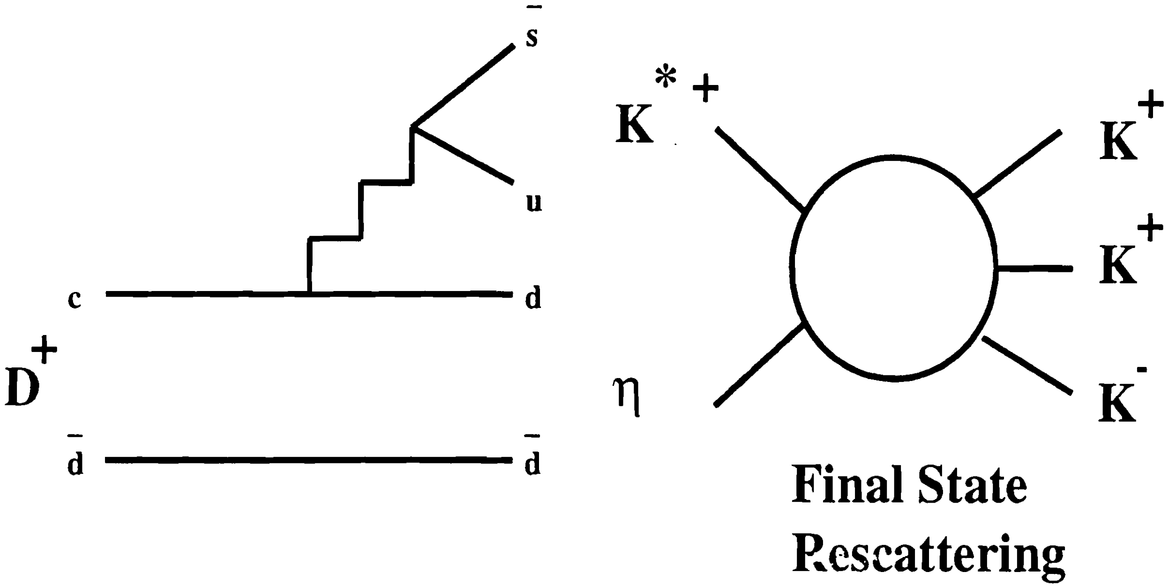

Figure 8.1: $D^+ \rightarrow K^+K^+K^-$, Spectator Diagram

8.2 Mass Width of $D^+ \rightarrow K^+K^+K^-$

The width of the decay $D^+ \rightarrow K^+K^+K^-$ in Monte Carlo is less than width of the decay $D^+ \rightarrow K^-\pi^+\pi^+$ in Monte Carlo. In addition, the Monte Carlo and data widths for $D^+ \rightarrow K^-\pi^+\pi^+$ are different.

The procedure used for determining the width is to determine a correction factor for the $D^+ \rightarrow K^+K^+K^-$ Monte Carlo width by comparing the widths in data and Monte Carlo of several three prong decays of the D^+ and D_s. The results are shown in Table 8.1. The Q values of the decays were included in the table because it was thought that the correction might depend on Q. It does not appear to. The the ratio of data to Monte Carlo mass widths is 1.4 ± .1. Using this value as a correction to the Monte Carlo width of $D^+ \rightarrow K^+K^+K^-$ and a measured width in the Monte Carlo of $\sigma_{D^+ \rightarrow K^+K^+K^-}$ = 4.0 MeV gives $\sigma_{D^+ \rightarrow K^+K^+K^-}$ = 5.6 ±.4 MeV.

Table 8.1: Monte Carlo and Data Mass widths

Decay	Data	Monte Carlo	Q Value
$D^+ \rightarrow K^-\pi^+\pi^+$	10.8 ± .2 MeV	7.6 ± .2 MeV	1100 MeV
$D^+ \rightarrow K^+K^-\pi^+$	7.1 ± .3 MeV	5.8 ± .1 MeV	740 MeV
$D_s \rightarrow K^+K^-\pi^+$	8.0 ± .6 MeV	5.4 ± .3 MeV	840 MeV

8.3 Backgrounds to $D^+ \rightarrow K^+K^+K^-$

Again the possible backgrounds to $D^+ \rightarrow K^+K^-K^+$ considered are those that can be misconstrued as $D^+ \rightarrow K^+K^-K^+$ with few reconstruction errors. In that case the principal backgrounds will be the decays $D^+ \rightarrow K^+K^-\pi^+$ and $D_s^+ \rightarrow K^+K^-\pi^+$. The reflection of $D^+ \rightarrow K^+K^+K^-$ into $K^+K^-\pi^+$ is shown in figure 8.2. A small peak indicating $D^+ \rightarrow K^+K^-\pi^+$ is visible. This is removed via a mass reflection cut made between 1.84 and 1.90 GeV.

Another possible background that was investigated was $\Lambda_c \rightarrow pK^-\pi^+$. 100,000 Monte Carlo events were generated, filtered, stripped, and substripped. Two events at 1.98 GeV made it to the final analysis histogram. We therefore conclude that this is not a significant background to $D^+ \rightarrow K^+K^+K^-$.

8.4 Mass Fits

The same analysis cuts that are applied to the $D \rightarrow K\pi\pi$ samples (Table 7.1), are applied the to the $D \rightarrow KKK$ sample. In addition, all particles in the vertex are required to have a kaon Čerenkov probability greater than .2. A mass reflection cut to remove background from $D^+ \rightarrow K^+K^-\pi^+$ is made. The fit to these data is shown in Table 8.2 and Figure 8.3. The fit gives $N_{D^+ \rightarrow K^+K^-K^+} = 3.1^{+2.7}_{-2.2}$. The Kolmogorov-Smirnoff test for this fit indicates the maximum deviation between the theoretical

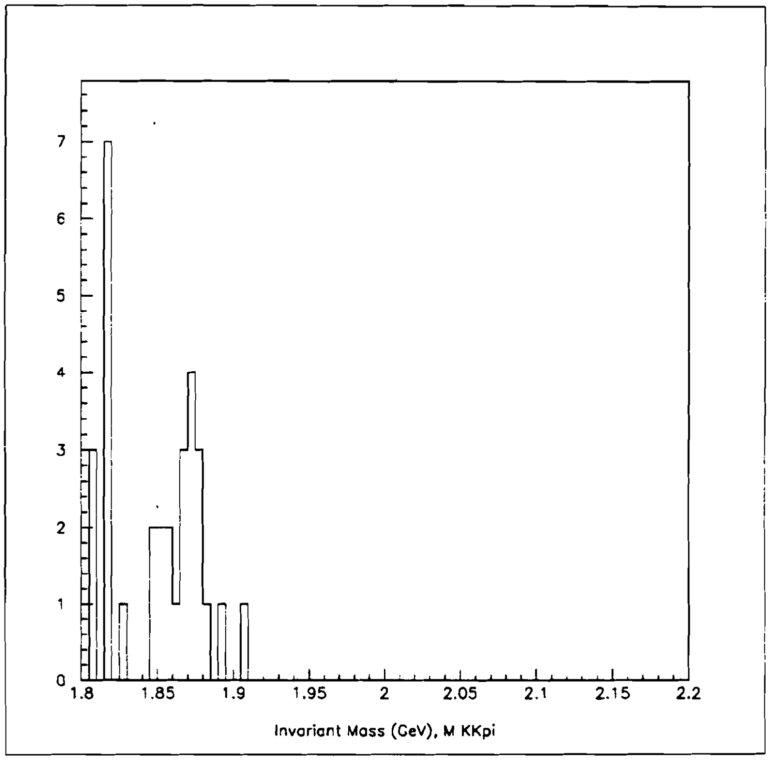

Figure 8.2: $D^+ \to K^+K^+K^-$ reflected into $K^+K^-\pi^+$

Table 8.2: $D^+ \rightarrow K^+K^+K^-$ Mass Fit

Parameter	Value	Parabolic Error
f	.0686	$^{+.062}_{-.051}$
M_{D^+}	1.870 GeV	Fixed
σ_{D^+}	.0055 GeV	Fixed
SLP	-4.507	2.257
$f_{D_s^+}$	.0962	.0551
$M_{D_s^+}$	1.9700 GeV	fixed
$\sigma_{D_s^+}$	.0055 GeV	fixed

cumulative probability distribution and the experimental probability distribution is 4.7%. The amount of deviation necessary to falsify the fit at the 80% confidence level is 15.6% ([Fr79])

The normalizing sample of $D^+ \rightarrow K^-\pi^+\pi^-$ events with all the analysis cuts of table 7.1 and the mass reflection cut to remove $D^+ \rightarrow K^+K^-\pi^+$ events is shown in figure 8.4. With these cuts $\mathrm{N}_{D^+\rightarrow K^-\pi^+\pi^+} = 5570.8 \pm 78.8$.

8.5 Systematic Error Due to Background Shape

One source of systematic uncertainty in the measured number of $D^+ \rightarrow K^+K^+K^-$ events is the uncertainty in the background shape. We postulate that the significant charm backgrounds have been removed by the mass reflection cut made to discard $D^+ \rightarrow K^+K^-\pi^+$ events. Therefore, we can obtain the background shape from a technique analogous to the procedure of section 7.7.

Figure 8.5 shows the $D^+ \rightarrow K^+K^+K^-$ background shape simulated using "Kaon" tracks (category 7 or 15 tracks with Kaon Čerenkov probability greater than .2) from separate events. In addition, figure 8.6 shows the background shape from real $D^+ \rightarrow K^+K^+K^-$ events when the analysis cuts are loosened in order to

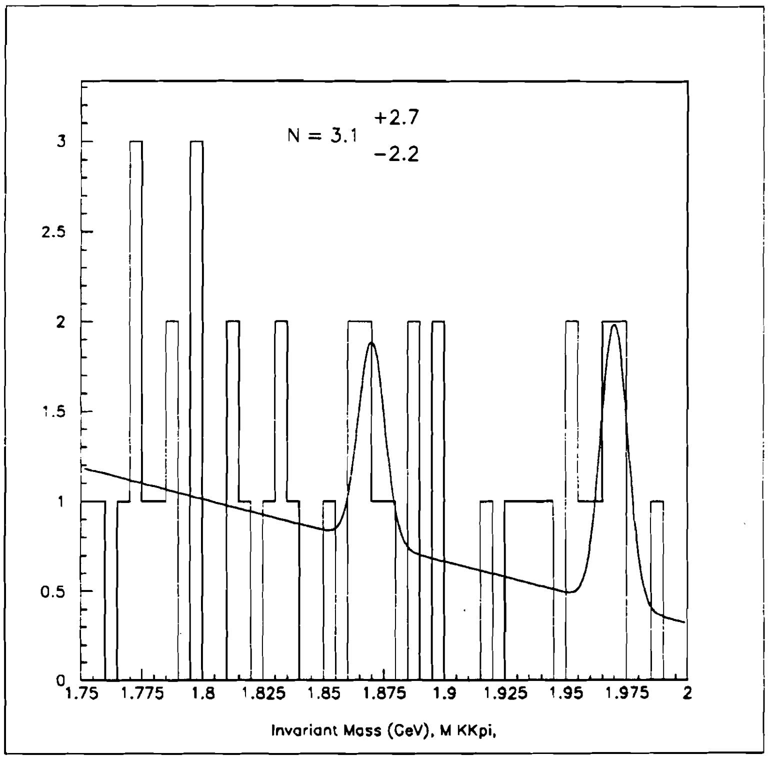

Figure 8.3: $D^+ \rightarrow K^+K^+K^-$

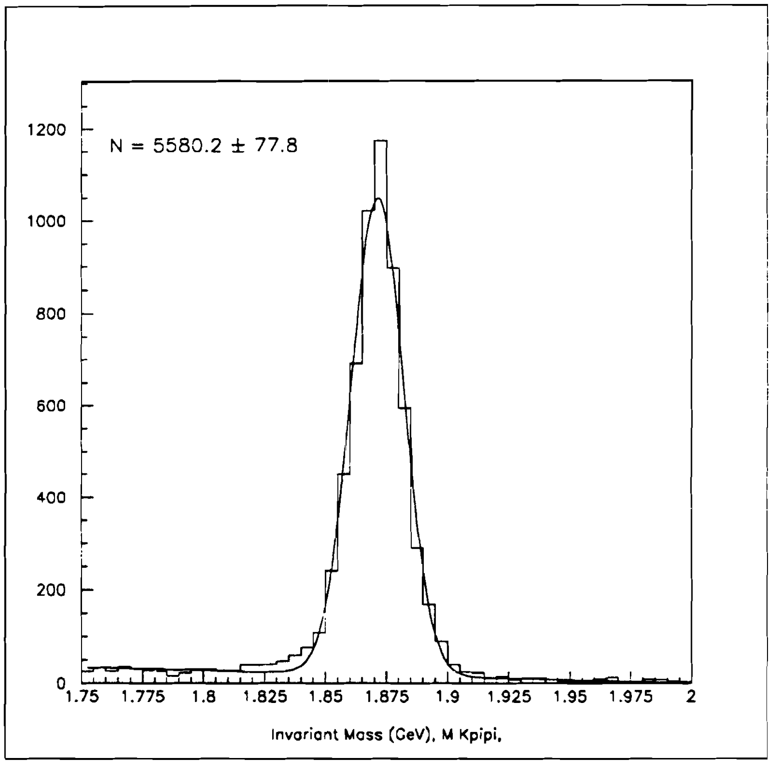

Figure 8.4: $D^+ \rightarrow K^-\pi^+\pi^+$

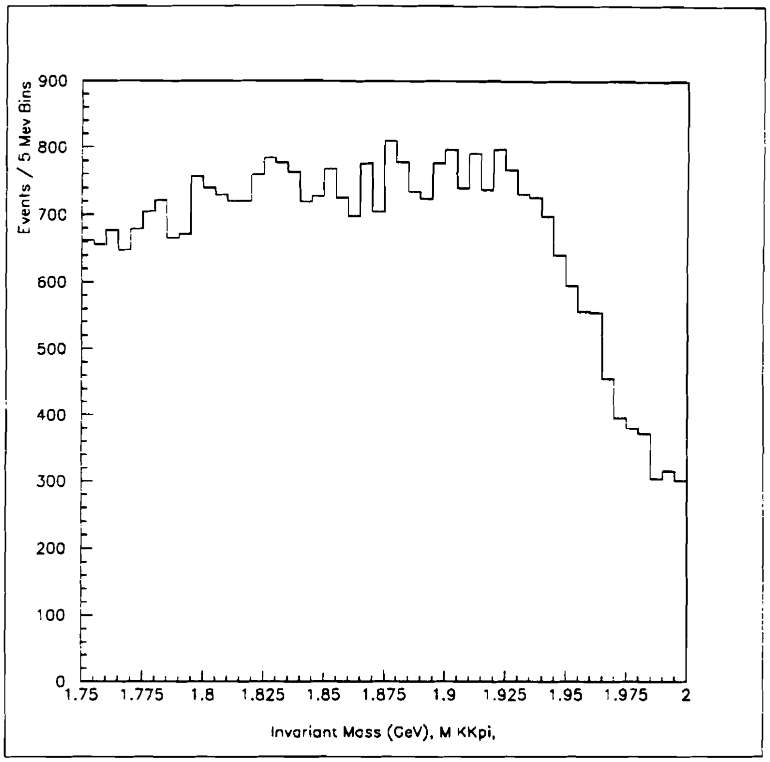

Figure 8.5: Simulated Background Shape
Assuming Background shape is from Combinatorics

allowing more combinatoric background in the final histograms. The shapes from both data and background are remarkably similar.

A fit using this background shape, shown in figure 8.7, gives $N_{D^+\to KKK} = 2.8^{+2.8}_{-2.1}$.

A final source of systematic uncertainty in the background shape is the uncertainty in the mass width of $D^+ \to K^+K^+K^-$. To measure the size of this uncertainty one can vary the width used in the fit by $\pm 2\sigma$. Doing this gives a change in the mean value of $N_{D^+\to KKK}$ equal to .1.

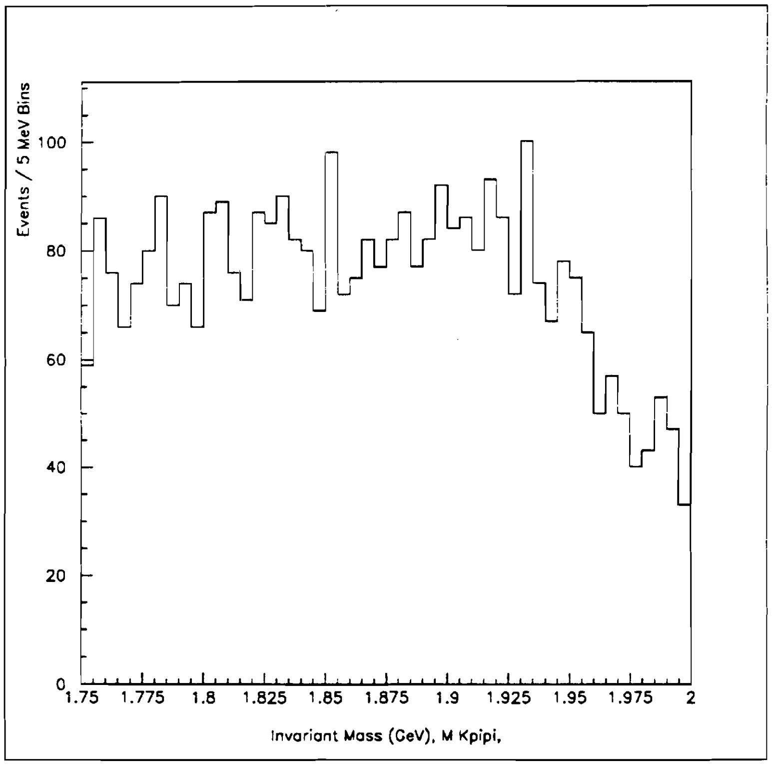

Figure 8.6: Background Shape from data with looser cuts

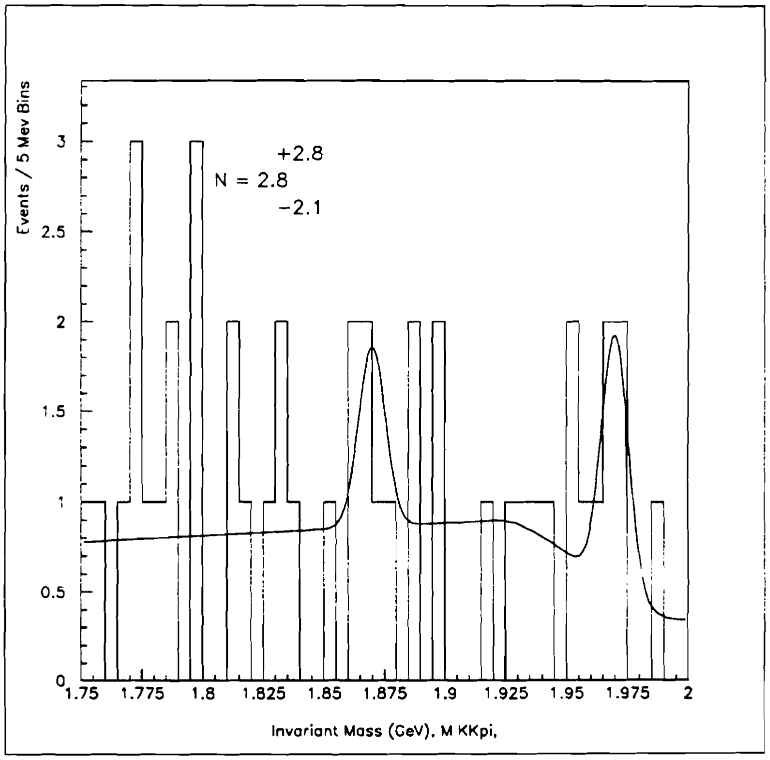

Figure 8.7: Fit with simulated background shape

8.6 Systematic Error Due to Relative Acceptance

The decays $D^+ \rightarrow K^-\pi^+\pi^+$ and $D^+ \rightarrow K^+K^+K^-$ have different acceptances because of differences in their respective decay topologies. The decay $D^+ \rightarrow K^+K^+K^-$ has significantly less Q than the decay $D^+ \rightarrow K^-\pi^+\pi^+$. This means that the opening angle in the $D^+ \rightarrow K^+K^+K^-$ case is smaller than the opening angle in the $D^+ \rightarrow K^-\pi^+\pi^+$ decay. Figure 8.8 shows the distribution of $\Delta\theta_x = \theta_{xparent} - \theta_{xdaughter}$ from the Monte Carlo Truth Table, for the $K^+K^+K^-$ and $K^-\pi^+\pi^+$ decays. The RMS of the $D^+ \rightarrow K^-\pi^+\pi^+$ events is .026 and the RMS of the $D^+ \rightarrow K^+K^+K^-$ events is .019. By this measure the opening angle of the $K^-\pi^+\pi^+$ decay is 30 % larger than the $K^+K^+K^-$ decay. This effect can generate a difference in acceptance because of the hole in the center of our drift chambers.

Figure 8.9 shows the drift chamber hole as it appears in data and $D^+ \rightarrow K^+K^+K^-$ Monte Carlo. Since the hole is centrally located and we have reason to believe that the $D^+ \rightarrow K^+K^+K^-$ decays are more central than the $D^+ \rightarrow K^-\pi^+\pi^-$ decays the $D^+ \rightarrow K^+K^+K^-$ decays might have a smaller acceptance.

Figure 8.10 shows 100,000 Monte Carlo $D^+ \rightarrow K^+K^-K^+$ and $D^+ \rightarrow K^-\pi^+\pi^-$ events run through the filter, strip, substrip, and analysis programs. The $D^+ \rightarrow K^+K^+K^-$ only had a Kaon Čerenkov cut placed on the K^- so that the samples would be directly comparable.

In addition, there is some uncertainty as to the exact hole parameters. This causes systematic uncertainty in the relative acceptance of $D^+ \rightarrow K^+K^+K^-$ with respect to $D^+ \rightarrow K^-\pi^+\pi^+$. By varying the hole within a reasonable set of parameters this systematic uncertainty is determined to be 5%.

Finally, one needs a measure of the efficiency of the two additional Kaon Čerenkov probability cuts that are applied to the $D^+ \rightarrow K^+K^+K^-$ decays. M The

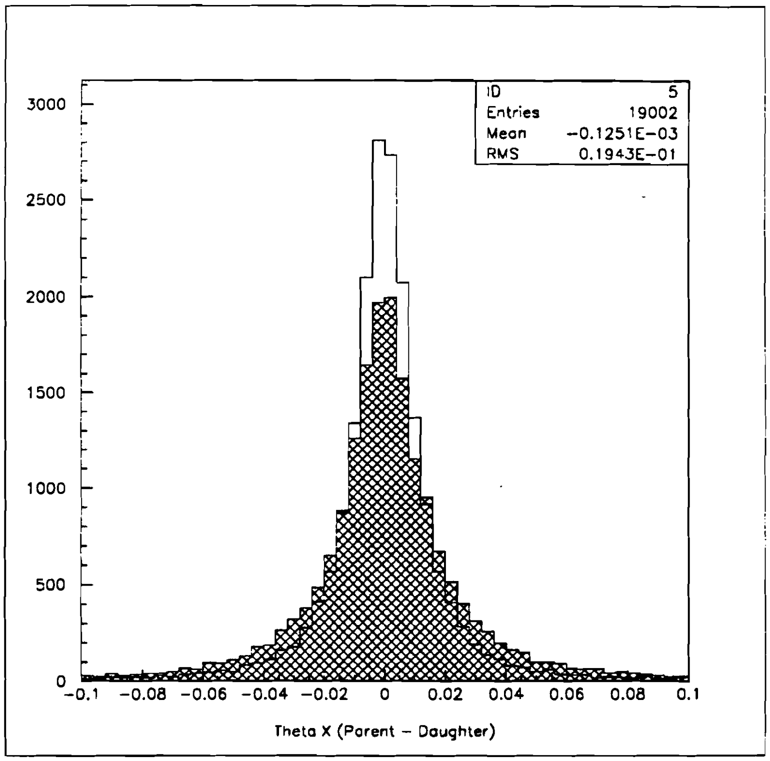

Figure 8.8: $\theta_{xdaughter} - \theta_{xparent}$ from Truth Table
White Histogram is for $D^+ \rightarrow K^+K^+K^-$
Shaded Histogram is for $D^+ \rightarrow K^-\pi^+\pi^+$

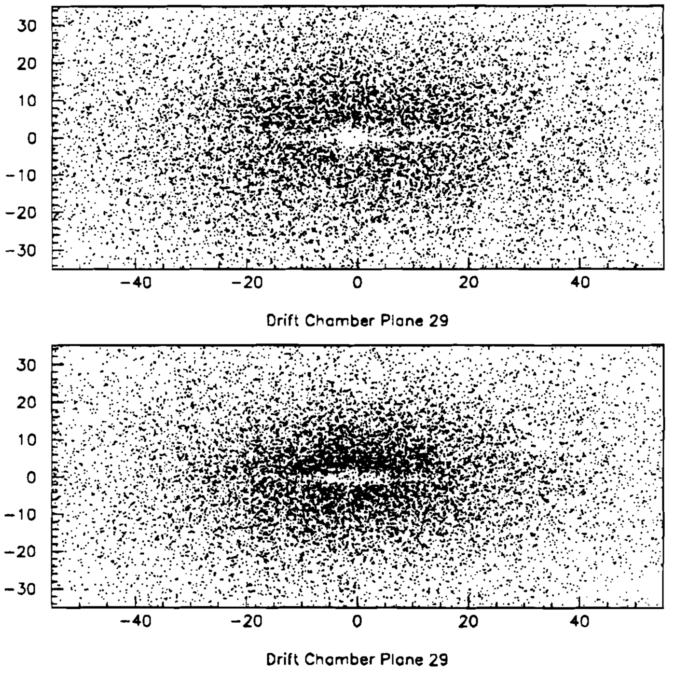

Figure 8.9: Drift Chamber hole in Plane 29
Top) Data
Bottom) $D^+ \rightarrow K^+K^+K^-$ Monte Carlo

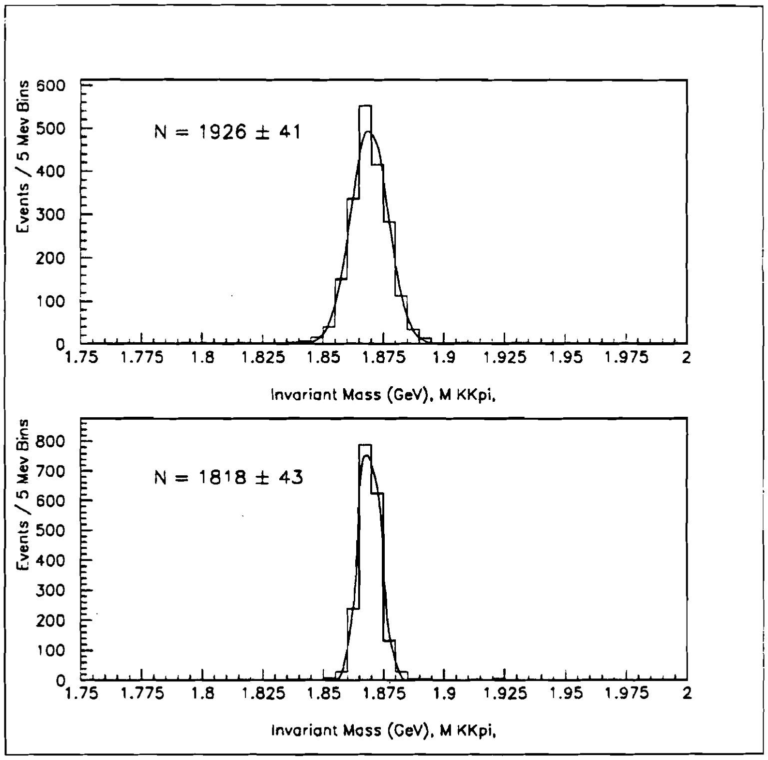

Figure 8.10: Number of $D^+ \rightarrow K^-\pi^+\pi^+$ (Top)and $D^+ \rightarrow K^+K^+K^-$ (Bottom) events accepted

Table 8.3: Systematic Errors

Source	Error
Background Shape	11 %
Monte Carlo Statistics	5 %
Mass Width	3 %
Uncertainty in DC Hole	5 %

single Kaon efficiency when a cut of .2 is applied to the Kaon in $D^+ \to K^-\pi^+\pi^+$ decays, summed over all momentum bins was found to be $\epsilon = .552 \pm .013$ ([Pu93]). The efficiency for the two additional Kaons is taken to be the square of this efficiency.

So, the results in figure 8.10 combined with the efficiency of the additional Kaon Čerenkov probability cuts give a result for the detection efficiency of $D^+ \to K^+K^+K^-$ relative to $D^+ \to K^-\pi^+\pi^+$ of $\epsilon = 0.280 \pm 0.014$.

8.7 Limit on $D^+ \to K^+K^+K^-$

Correcting for the efficiency of $D^+ \to K^+K^+K^-$ relative to $D^+ \to K^-\pi^+\pi^+$ we get $N_{D^+\to K^+K^+K^-} = 11.1\ ^{+9.6}_{-7.9} \pm 1.6$. Table 8.3 summarizes the contribution to the systematic error, which are added in quadrature.

Therefore

$$\frac{\Gamma(D^+ \to K^+K^+K^-)}{\Gamma(D^+ \to K^-\pi^+\pi^+)} = \frac{11.1^{+9.6}_{-7.9} \pm 1.6}{5580.2 \pm 77.8} = .0020^{+.0017}_{-.0014} \pm .0003$$

Therefore,

$$\frac{\Gamma(D^+ \to K^+K^+K^-)}{\Gamma(D^+ \to K^-\pi^+\pi^+)} < .0042 \text{ @ } 90\% \text{ CL}$$

or

$$\frac{\Gamma(D^+ \to K^+K^+K^-)}{\Gamma(D^+ \to K^-\pi^+\pi^+)} \times \frac{1}{tan^4\theta_c} < 1.6 \text{ @ } 90\% \text{ CL}$$

8.8 Limit on $D^+ \to K^+\phi$

Although only a few $D^+ \to K^+K^+K^-$ events were observed in the previous section, it maybe possible to observe a resonant decay such as $D^+ \to K^+\phi$ because the extremely narrow width of the ϕ will greatly suppress background. Because of the narrow ϕ width the Čerenkov kaon probability cuts were relaxed to 0.14. The width of the ϕ in our detector in this decay is measured by examining $D^+ \to \pi^+\phi$ events. Analysis cuts identical to those in Table 7.1 were applied to the three prong sample of $D^+ \to K^+K^-\pi^+$ candidates and the K^+K^- invariant mass is plotted in figure 8.11. Therefore, a cut on the invariant mass for either K^+K^- pairing between 1.005 and 1.035 GeV is 100 % efficient for ϕ's. The result of making the ϕ mass cut is shown in figure 8.12. (The result for $D^+ \to K^+\phi$ is not adjusted for the branching ratio of $\phi \to K^+K^-$ this will drop out when the ratio is taken to $D^+ \to \pi^+\phi$).

In addition to a cut on the ϕ mass one can use the angular distribution of the D^+ decay products in order to separate signal from background. Since the ϕ is spin one and the D^+ is spin zero in the rest frame of the ϕ the relative angular momentum between the two K^+s must be one (see Figure 8.13). Hence the angle must be distributed as $\cos^2\theta$. A cut of $|\cos\theta| > .5$ enhances signal with respect to background. Figure 8.14 shows the $D^+ \to K^+\phi$ invariant mass spectrum after this $\cos\theta$ cut is made.

The invariant mass for the decay $D^+ \to \phi\pi^+$ is shown in figure 8.15. The fit yields $N_{D^+\to\pi^+\phi} = 142.5 \pm 12.3$ (again this is uncorrected for the branching ratio of $\phi \to K^+K^-$). Assuming that the geometric acceptance of $D^+ \to K^-\pi^+\pi^+$ is

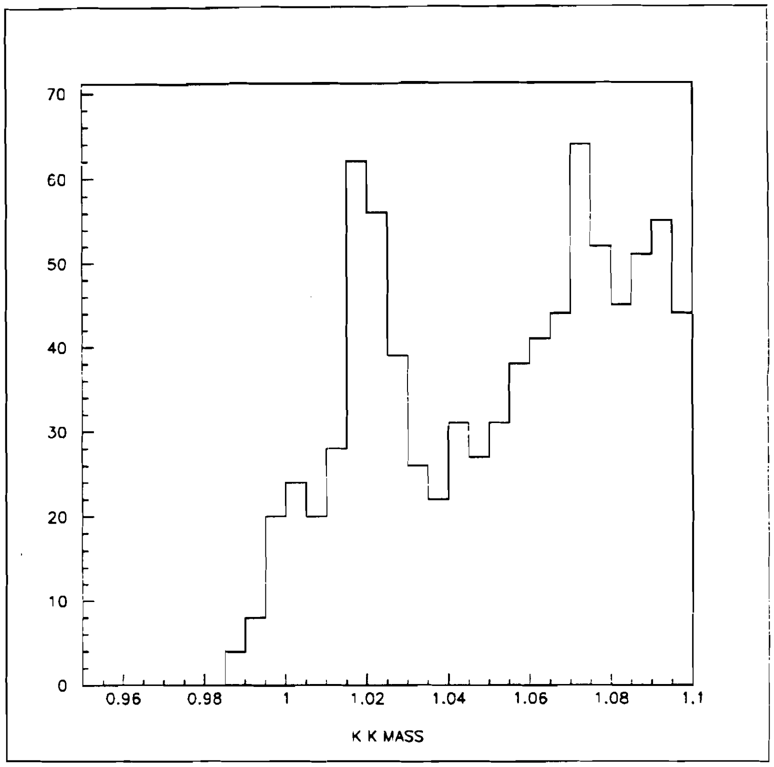

Figure 8.11: K^+K^- invariant mass in $D^+ \to K^+K^-\pi^+$ decays

Table 8.4: $D^+ \to K^+\phi$ Mass Fit

Parameter	Value	Parabolic Error
f	.6362	$^{+1.3}_{-1.5}$
M_{D^+}	1.870 GeV	Fixed
σ_{D^+}	.0055 GeV	Fixed
SLP	0.	fixed

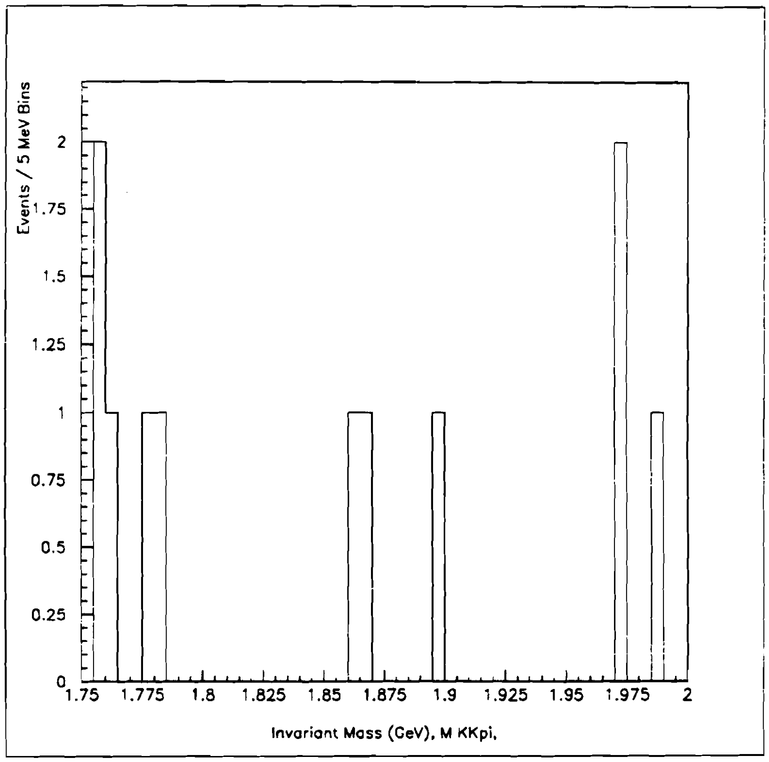

Figure 8.12: $D^+ \rightarrow K^+\phi$

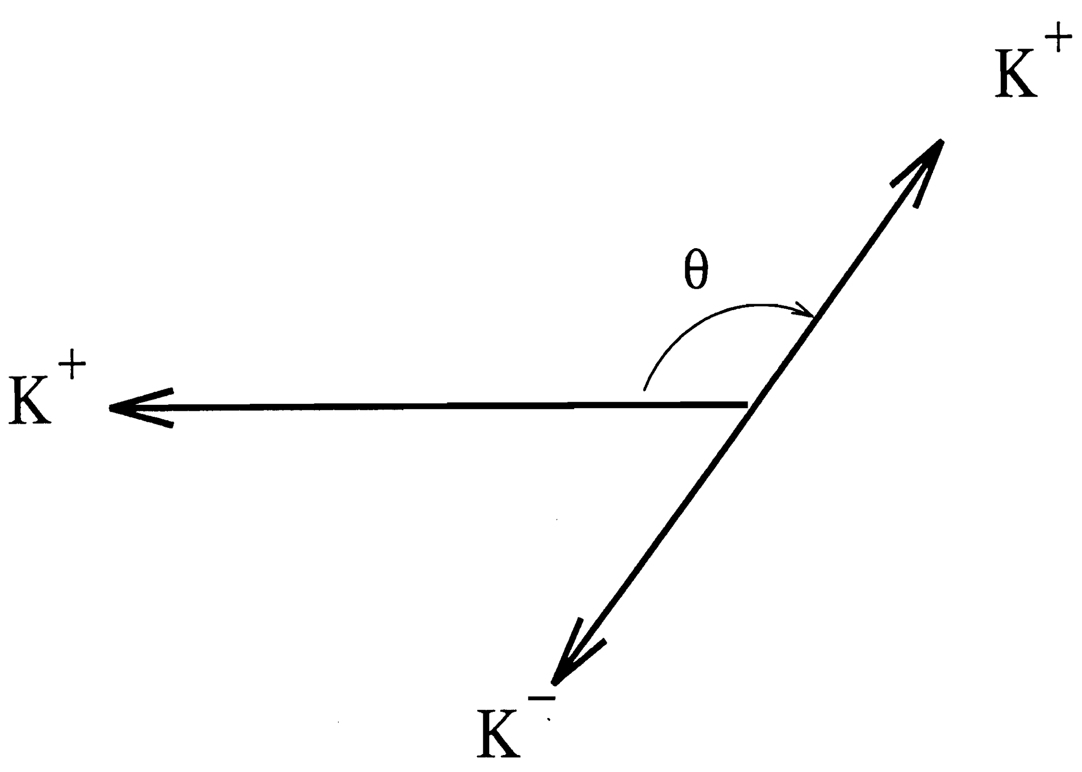

Figure 8.13: The definition of θ

identical to $D^+ \to \phi\pi^+$ the particle data group predicts $N_{D^+\to\pi^+\phi}$ = (5580 ± 77.8) × (.075 ± .007) × (.73 ± .03) × (.491 ± .008) = 150.0 ± 15.0. Where the second term is $\frac{\Gamma(D^+\to\phi\pi^+)}{\Gamma(D^+\to K^-\pi^+\pi^+)}$, the third term is the relative efficiency of the different Kaon Čerenkov probability cuts, and the fourth term is the branching fraction of ϕ into K^+K^-. Finally, figure 8.16 shows the $D^+ \to \phi\pi^+$ events after a $|cos\theta| > .5$ cut is applied.

8.8.1 Systematic Error due to the Uncertainty in background shape

In order to determine the systematic error in $N_{D^+\to K^+\phi}$, we vary the mass width by ± 1 MeV. This gives a systematic error of 4%.

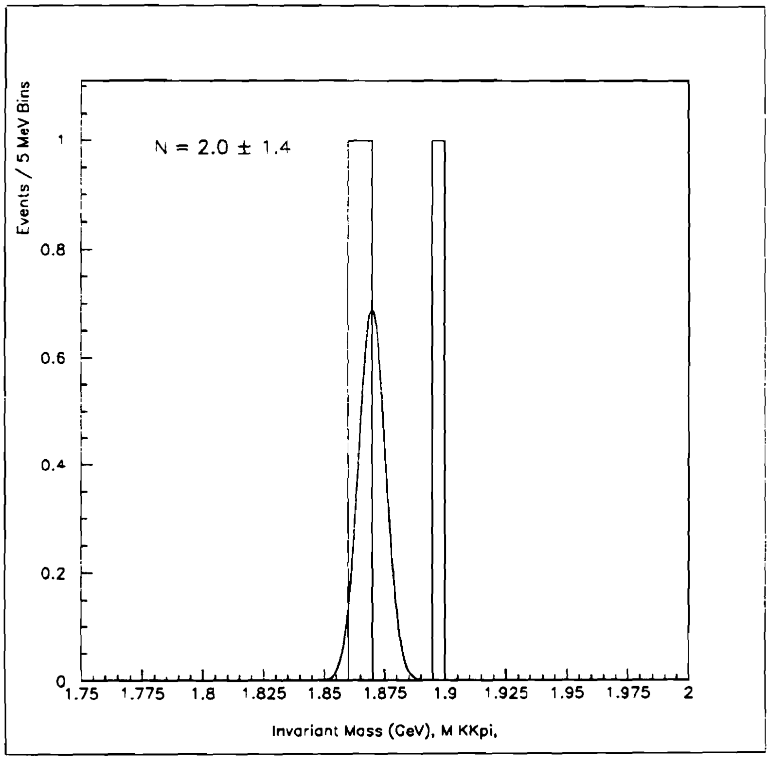

Figure 8.14: $D^+ \rightarrow K^+\phi$ after cosθ cut

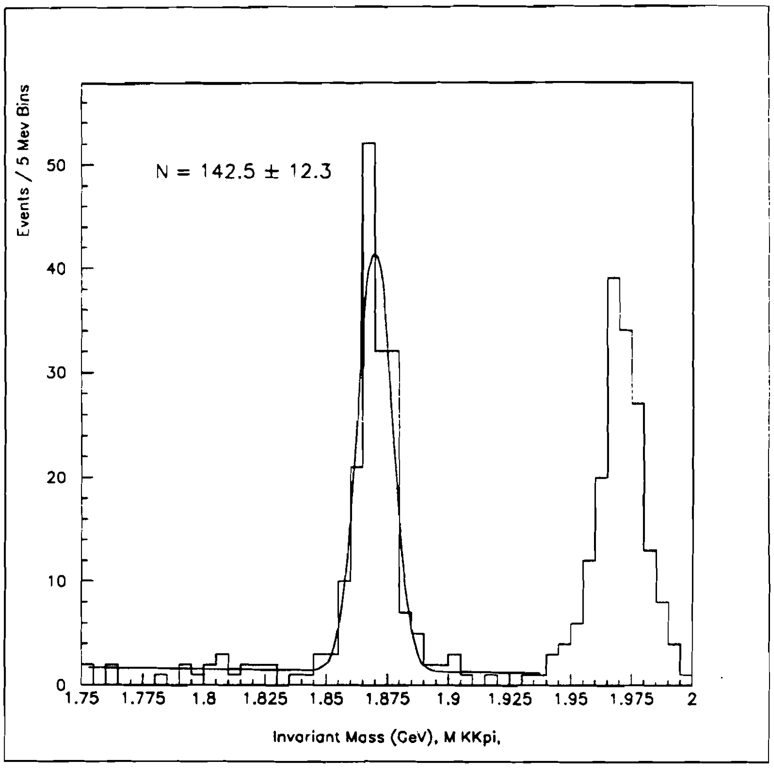

Figure 8.15: $D^+ \rightarrow \pi^+\phi$

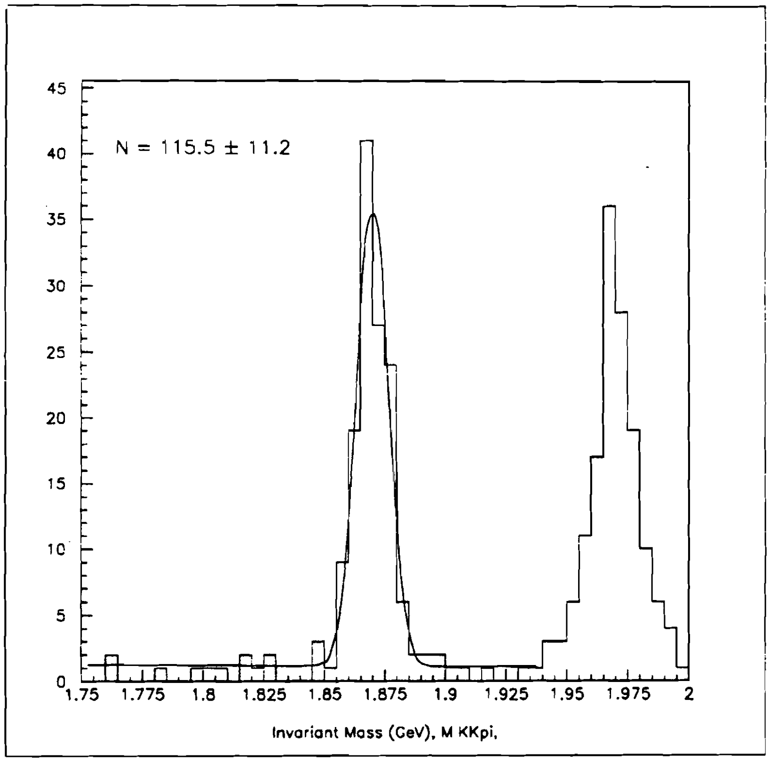

Figure 8.16: $D^+ \rightarrow \pi^+\phi$, after $cos\theta$ cut

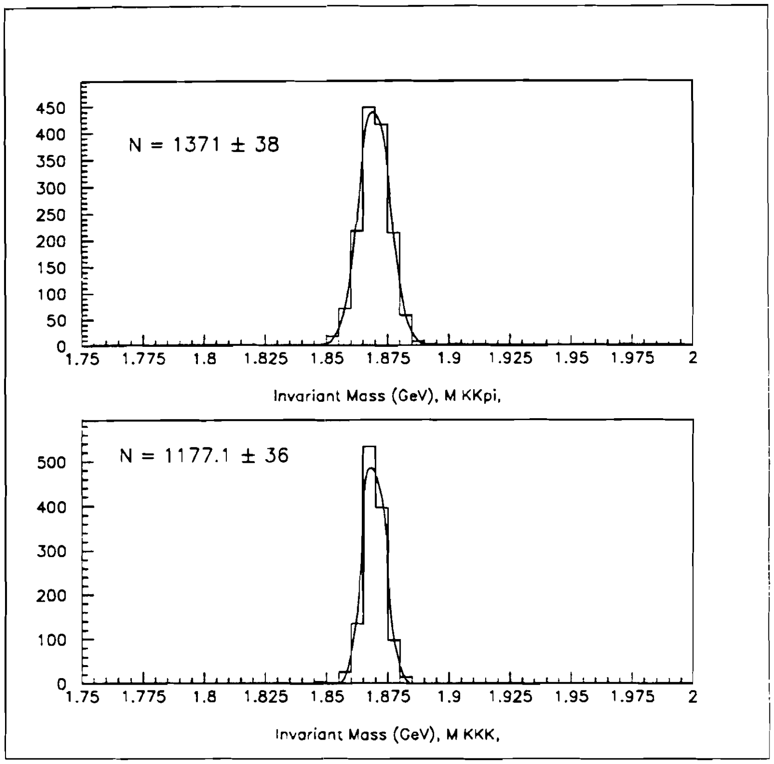

Figure 8.17: Top) $D^+ \to \pi^+\phi$
Bottom) $D^+ \to K^+\phi$

8.8.2 Relative Acceptance

To determine the acceptance of $D^+ \to K^+\phi$ relative to $D^+ \to \pi^+\phi$ we again use Monte Carlo. Figure 8.17 shows the results of generating, filtering, stripping, and substripping 100,000 Monte Carlo $D^+ \to K^+\phi$ and $D^+ \to \pi^+\phi$ events. All the standard analysis cuts were applied except that for the $D^+ \to K^+\phi$ events Kaon Čerenkov probability cuts were only applied to two particles so that samples would be directly comparable.

The results of this study give a relative acceptance of 86 ± 4 %.

Table 8.5: Systematic Errors

Source	Error
Monte Carlo Statistics	4 %
Mass Width	4 %
Uncertainty in DC Hole	5 %

8.8.3 Limit

Finally, correcting for the relative acceptance and additional the Kaon Čerenkov probability cut

$$\frac{\Gamma(D^+ \to K^+\phi)}{\Gamma(D^+ \to \phi^+\pi^+)} = \frac{1}{\epsilon}\frac{1.9^{+1.3}_{-1.5} \pm .1}{115.5 \pm 11.2} = 3.2^{+2.2}_{-2.3} \pm 0.3 \times 10^{-2}$$

or a Limit of

$$< 6.0 \times 10^{-2} @ \ 90\%\mathrm{CL}$$

Table 8.5 shows the contribution to the systematic errors for $D^+ \to K^+\phi$, which are added in quadrature.

Chapter 9

Conclusions

9.1 Introduction

Measurements of doubly Cabibbo suppressed decays of the D^+ test theories of hadronic charm decay. Two alternate explanations for the experimental fact $\tau_{D^+} \approx 2.5 \times \tau_{D^0}, \tau_{D_s^+}$ exist. The first postulates that the spectator dominance model does not hold for charm meson decays. Therefore, because figure 9.1(a) is singly Cabibbo suppressed and figures 9.1(b) and 9.1(c) are Cabibbo favored the D^+ has a longer lifetime. The other explanation is that destructive interference between the diagrams in figure 9.2 is responsible for suppressing the hadronic width of the D^+. Measurement of DCSDs of the D^+ may be able to distinguish between these two explanations.

9.2 $D^+ \to K^+\pi^+\pi^-$

If the spectator dominance model is correct then the measurement of $\frac{\Gamma(D^+\to K^-\pi^+\pi^+)}{\Gamma(D^+\to K^+\pi^-\pi^+)}$ is a direct measure of the relative strength of the diagrams in figure 9.3. Because

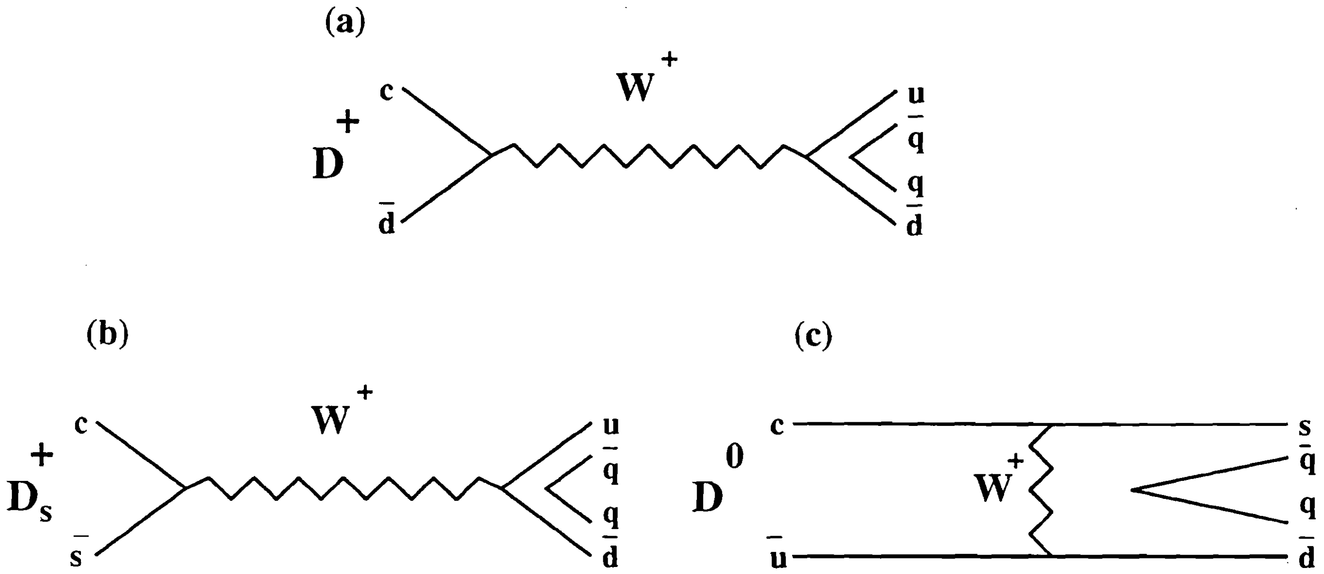

Figure 9.1: WA Diagrams: (a) of the D^+, (b) of the D_s^+, and (c) of the D^0

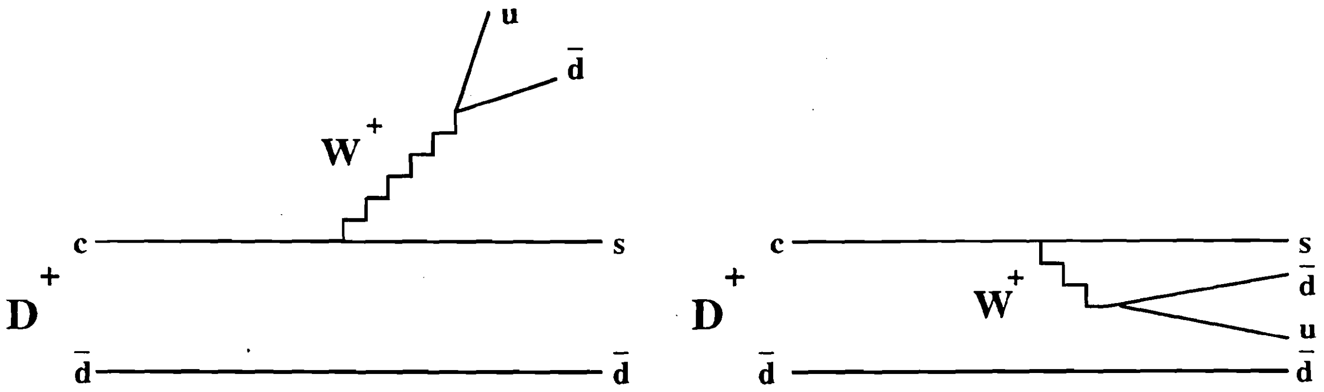

Figure 9.2: D^+ spectator decay diagram and the diagram obtained by exchange of identical $\bar{d}$ quarks

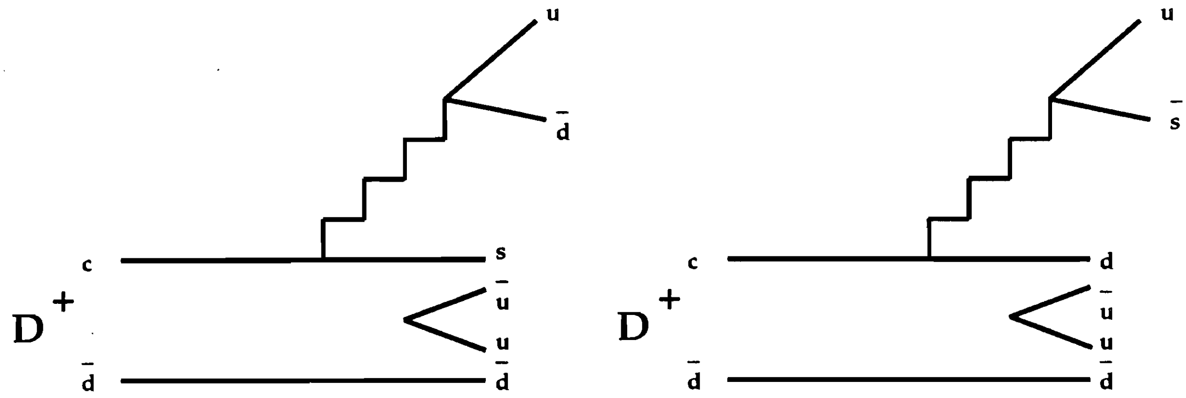

$D^+ \to K^-\pi^+\pi^+$ $D^+ \to K^+\pi^+\pi^-$

Figure 9.3: $D^+ \to K^\pm\pi\pi$

the DCSD diagram does not have identical quarks in its final state it should be enhanced relative to the Cabibbo favored diagram after accounting for two Cabibbo suppressions.

If the WA diagrams are not suppressed then DCSD diagrams similar to figure 9.1(a) will contribute to the DCSD width (but not the favored mode width). Therefore, this model also predicts an enhancement relative to the favored mode after accounting for two Cabibbo suppressions.

However, the DCSD measurement along with information from singly Cabibbo suppressed decays allows us to choose between the two competing explanations. Table 9.2 shows a series of two body Cabibbo favored and singly Cabibbo Suppressed decays of the D^0 and D^+ from [PDG92].

The first thing one notices is that $\frac{\Gamma(D^0\to\overline{K}^{*-}\pi^+)}{\Gamma(D^0\to\overline{K}^{*-}K^+)} = 21.4 \pm 9.0$, $\frac{\Gamma(D^0\to K^-\rho^+)}{\Gamma(D^0\to K^-K^{*+})} = 17.4 \pm 4.3$, and $\frac{\Gamma(D^0\to K^-\pi^+)}{\Gamma(D^0\to K^-K^+)} = 8.8 \pm 1.0$. The first two ratios seem in excellent agreement with the spectator dominance model of charm meson decays which would predict $\frac{1}{tan^2\theta_c} \approx 20$.

Furthermore $\frac{\Gamma(D^+\to\overline{K}^0\pi^+)}{\Gamma(D^+\to\overline{K}^0K^+)} = 3.5 \pm 1.2$ and $\frac{\Gamma(D^+\to\overline{K}^{*0}\pi^+)}{\Gamma(D^+\to\overline{K}^{*0}K^+)} = 4.5 \pm 1.6$. Without any enhancement one would expect these numbers to be of order 20. Therefore,

Table 9.1: Some D^+ and D^0 Two Body Decays
Adapted From [So94, PDG92]

		PP	VP	PV
D^+	Mode	$\overline{K}^0\pi^+$	$\overline{K}^{*0}\pi^+$	$\overline{K}^0\rho^+$
Cabibbo	BR (%)	$2.6 \pm .4$	$1.9 \pm .7$	6.6 ± 1.7
Allowed	Width (10^{10}sec^{-1})	$2.4 \pm .4$	$1.8 \pm .7$	6.2 ± 1.6
D^0	Mode	$K^-\pi^+$	$K^{*-}\pi^+$	$K^-\rho^+$
Cabibbo	BR (%)	$3.7 \pm .2$	$4.5 \pm .6$	7.3 ± 1.1
Allowed	Width (10^{10}sec^{-1})	$8.8 \pm .5$	10.7 ± 1.4	17.4 ± 2.6
D^+	Mode	$\overline{K}^0K^+$	$\overline{K}^{*0}K^+$	$\overline{K}^0K^{*+}$
Cabibbo	BR (%)	$.7 \pm .2$	$.5 \pm .1$	
Suppressed	Width (10^{10}sec^{-1})	$.7 \pm .2$	$.4 \pm .1$	
D^0	Mode	K^-K^+	$K^{*-}K^+$	K^-K^{*+}
Cabibbo	BR (%)	$.40 \pm .04$	$.2 \pm .1$	$.4 \pm .1$
Suppressed	Width (10^{10}sec^{-1})	$1.0 \pm .1$	$.5 \pm .2$	$1.0 \pm .2$

these data predicts the Cabibbo suppressed diagrams are enchanced relative to the Cabibbo favored by a factor of 5.0 ± 1.4 after the Cabibbo suppression is taken into account. Therefore, the singly Cabibbo suppressed data predicts that if the spectator dominance model is correct

$$\frac{\Gamma(D^+ \rightarrow K^+\pi^+\pi^-)}{\Gamma(D^+ \rightarrow K^-\pi^+\pi^+)} \times \frac{1}{tan^4\theta_c} = 5.0 \pm 1.4$$

We measure,

$$\frac{\Gamma(D^+ \rightarrow K^+\pi^+\pi^-)}{\Gamma(D^+ \rightarrow K^-\pi^+\pi^+)} \times \frac{1}{tan^4\theta_c} = 3.5 \pm 1.1 \pm .4$$

which agrees with the spectator dominance model and the idea the Cabibbo favored hadronic diagrams of the D^+ are suppressed by destructive interference.

Since, $D^+ \rightarrow K^*(892)\pi^+$ is a two body decay, one can use the Bauer, Stech, and Wirbel formalism to calculate its partial width. As explained in Chapter 1 the BSW formalism is a phenomenological approach incorporating the spectator dominance model and destructive interference in the hadronic Cabibbo favored spectator diagrams of the D^+. I. I. Bigi has calculated

$$\frac{\Gamma(D^+ \rightarrow K^*(892)\pi^+)}{\Gamma(D^+ \rightarrow K^-\pi^+\pi^+)} \times \frac{1}{tan^4\theta_c} \approx 1.1 \sim 2.4 \qquad \text{[Bi88b, PDG92]}$$

We measure

$$\frac{\Gamma(D^+ \rightarrow K^*(892)\pi^+)}{\Gamma(D^+ \rightarrow K^-\pi^+\pi^+)} \times \frac{1}{tan^4\theta_c} = 2.9 \pm 1.0 \pm .2$$

Which supports the spectator dominance model and the idea of destructive interference in hadronic Cabibbo favored diagrams of the D^+.

These results add to a large and growing body of evidence that the spectator dominance model with destructive interference in the D^+ hadronic diagrams explains the long D^+ lifetime.

9.3 $D^+ \rightarrow K^+K^+K^-$

Other 3-prong doubly Cabibbo suppressed decays are easily accessible in this dataset. The WA82 Collaboration has reported the observation of the doubly Cabibbo suppressed decay $D^+ \rightarrow K^+K^+K^-$. They have measured

$$\frac{\Gamma(D^+ \rightarrow K^+K^+K^-)}{\Gamma(D^+ \rightarrow K^-\pi^+\pi^+)} = 0.057 \pm 0.020 \pm 0.007 \qquad \text{[Ad93]}$$

Our measurement of

$$\frac{\Gamma(D^+ \rightarrow K^+K^+K^-)}{\Gamma(D^+ \rightarrow K^-\pi^+\pi^+)} < 0.0044 \text{ @ } 90\%\text{CL}$$

clearly contradicts this result.

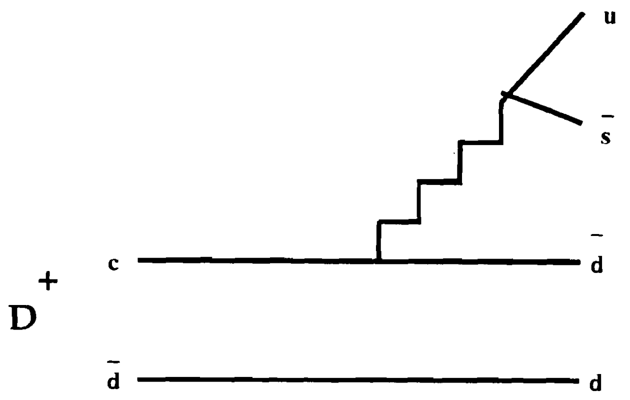

Figure 9.4: Spectator DCSD Feynman diagram for the D^+

The doubly Cabibbo suppressed decay $D^+ \to \phi K^+$ is particularly interesting. Neither it nor the $D^+ \to K^+K^+K^-$ decay can proceed via the spectator DCSD diagram figure 9.4. Therefore, in the spectator dominance model one would expect these decays to be even more suppressed than the average DCSD.

However, the one clear exception to the spectator dominance model is the decay $D^0 \to \phi\overline{K}^0$ which does have a relatively large branching ratio [PDG92]. Since it cannot proceed via a spectator diagram, it has been postulated that some sort of final state rescattering may be responsible for the enhancement of this mode. If that is the case the decay $D^+ \to \phi K^+$ might be enchanced by similar means.

Experiment E691 has measured

$$\frac{\Gamma(D^+ \to \phi K^+)}{\Gamma(D^+ \to \phi\pi^+)} = (5.8^{+3.2}_{-2.6} \pm 0.7) \times 10^{-2} \qquad \text{[An92]}$$

While we measure

$$\frac{\Gamma(D^+ \to \phi K^+)}{\Gamma(D^+ \to \phi\pi^+)} = (2.8^{+1.9}_{-2.0} \pm .2) \times 10^{-2}$$

This is consistent with E691 result. Although the statistical significance is so low that it is hard to make much out of this result. Nevertheless, should the mean hold up with more data the apparent enhancement of this mode would be very interesting.

9.4 Prospects for the future

This thesis represents analysis of one third of E791's full dataset. It seems likely that the tripling of the amount data we can analyze will allow us to announce the unambiguous discovery of the doubly Cabibbo suppressed decays $D^+ \rightarrow K^+\pi^+\pi^-$ and $D^+ \rightarrow K^*(892)\pi^+$ with five sigma peaks. Furthermore, it is possible we may be able confirm E691's observance of $D^+ \rightarrow \phi K^+$.

Appendix A

Linear Discriminant Functions

A.1 Introduction

A common problem in High Energy Physics is the separation of events into broad categories. The separation between kaons and pions, between muons and hadrons, and between ghosts and real tracks are familiar examples. The common solution to this problem is to generate a series of cuts, on the kinematic variables that describe the events, which optimize the separation between the categories. This technique is only undesirable in that is does not prescribe the method by which these cuts are to be determined.

In this situation it may be fruitful to apply techniques of statistical pattern recognition to the data sample. The basic idea of statistical pattern recognition is to form a $P(w_i|\vec{x})$ (probability of class w_i given the measurement or feature vector $\vec{x}$) for each class w_i. The event is then assigned to the class with the largest $P(wi|\vec{x})$. In this appendix, pattern recognition techniques that assume $P(w_i|\vec{x})$ is a linear function of the measurement vector are explored.

A.2 The Fisher Discriminant

A discriminant function is merely defined to be

$$g_i(\vec{x}) \equiv P(w_i|\vec{x})$$

and Fisher's linear discriminant function is just the most general linear form of $g_i(\vec{x})$

$$g_i(\vec{x}) = \tilde{\omega}_i \vec{x} + \omega_{i0} \qquad (A1.1)$$

Where the indice i refers to the category or class.

For the two class case instead of constructing a g_i for each class one constructs a single $g(\vec{x})$ and associates the measurements with class A if $g(\vec{x}) > \lambda$ and class B if $g(\vec{x}) < \lambda$ (the actual numerical value of λ is irrelevant since it can be absorbed into the definition of the $\tilde{\omega}_i$'s.) This procedure when used with linear discriminant functions amounts to projecting the vector $\vec{x}$ onto a line and hoping the projections are well separated by class. A trivial example in two dimensions is illustrated in figures A1.1 and A1.2. In figure A1.1 the projections of the two classes onto the dashed line ($\vec{\omega}$) are not well separated by class. While the projections onto the dashed line in figure A1.2 are well separated by class. The key question is then how to choose the orientation so that the separation is optimized.

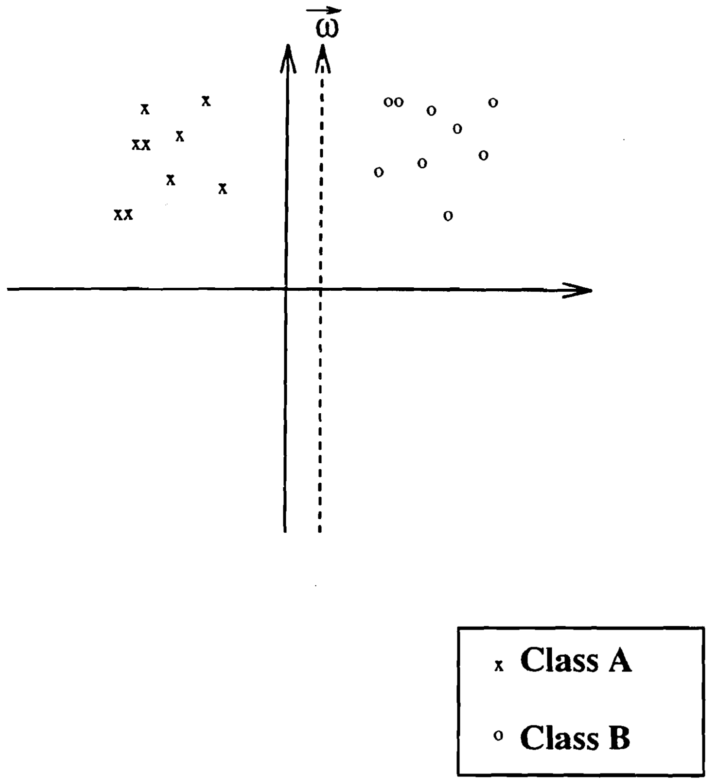

Figure A1.1: Geometric Interpretation of the Fisher Discriminant

The orientation of the line is poorly chosen

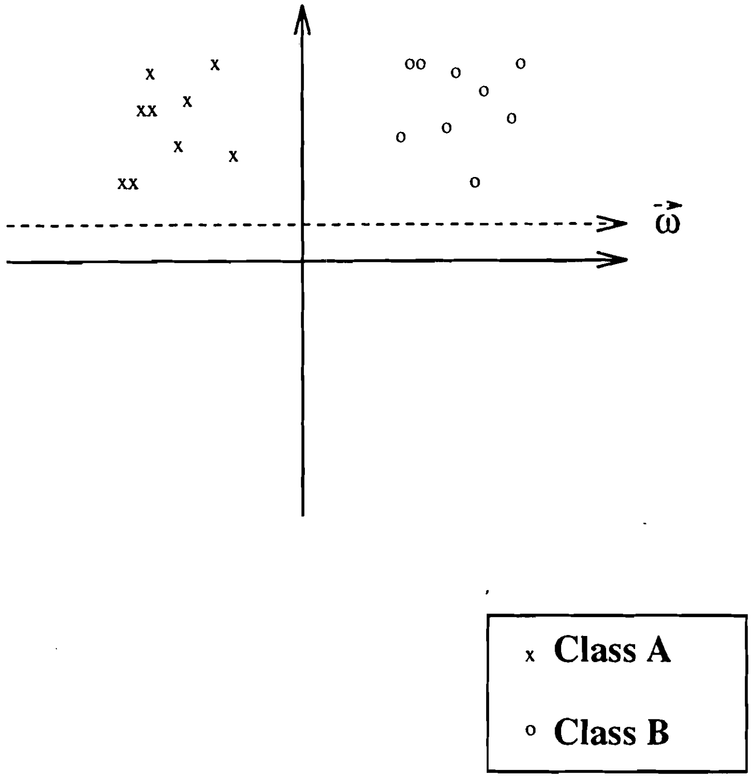

Figure A1.2: Geometric Interpretation of the Fisher Discriminant

The orientation of the line is wisely chosen

A reasonable measure of the class separation along the line is

$$J(\tilde{\omega}) = \frac{(\mu_a - \mu_b)}{(\sigma_a^2 + \sigma_b^2)}$$

where

$$\mu_i = \tilde{\omega} < \vec{x} > \qquad i = a, b$$

and

$$\sigma_i^2 = \tilde{\omega} \Sigma_i \vec{\omega} \qquad i = a, b$$

Σ_i is covariance matrix between the components of $\vec{x}$ for class i.

Fisher's solution for the orientation of $\tilde{\omega}$ is to solve

$$\frac{\partial J}{\partial \omega} = 0$$

This yields([Sc92])

$$\tilde{\omega} = \frac{1}{2}\frac{\sigma_a^2 + \sigma_b^2}{\mu_a - \mu_b}(\Sigma_a + \Sigma_b)^{-1}(\mu_a - \mu_b) \qquad (A1.2)$$

A.3 The Solution in High Energy Physics

Equation A1.2 is a somewhat roundabout way of determining $\tilde{\omega}$. It requires that we approve of $J(\tilde{\omega})$ as a measure of the separateness of the class projections. It is better to choose the orientation of $\tilde{\omega}$ tuning directly on the separation we which to optimize. Obviously, this requires a training set in which the class identities are known. Tuning on the data you wish to analyze will bias your results (one has this problem when choosing cuts in the standard high energy physics techniques), but one can use either Monte Carlo or related data samples.

In this thesis, the statistical significance of the DCSD signal is to be optimized. The values of $\tilde{\omega}$ have been chosen by tuning on the right sign sample. Initially, arbitrary values of chosen for the components of $\tilde{\omega}$. The Fisher discriminant (equation A1.1) is calculated for each event. If it is greater than zero the event's invariant mass is histogrammed. After processing all events in the sample the amount and signal and background is determined. Minuit then adjusts the values of the components in order to minimize the function $f = -\frac{Signal/80}{\sqrt{Signal/80+Background}}$. It is assumed that the DCSD signal has the same background as the Cabibbo favored sample and the signal is suppressed by a factor on $5 \times tan^4\theta_c$. The discriminant with these weights was then used to separate signal from background in the DCSD sample.

A.4 Other Methods

One should be aware that there are other powerful pattern recognition techniques (neural networks, binary decision trees, non-parametric techniques, parzen windows, the nearest neighbor rule, and etc.) that may be useful in high energy physics. I have found the book **Pattern Recognition, Statistical, Structural, and Neural Approaches** by Robert Schalkoff to be an excellent practical overview of these topics.

Bibliography

[Ad93] M. Adamovich *et. al.*, Physics Letter B 305, 177 (1993).

[An92] J.C. Anjos *et. al.*, Preprint Submitted to Physical Review Letters, 1992.

[Ap85] J.A. Appel *et. al.*, NIM 228, 283 (1985).

[Ap86] J.A. Appel *et. al.*, NIM A 243, 361 (1986).

[Am93] S. Amato *et. al.*, NIM A324. 535 (1993).

[Ba85] M. Bauer and B. Stech, Phys. Lett. B 152, 380 (1985).

[Ba87] M. Bauer, B. Stech, and M. Wirbel, Z. Phys. 34. 103 (1987).

[Bar87] D. Bartlett *et. al.* , NIM A 260, 55 (1987).

[Bi88a] I. Bigi, in *Charm Physics*, edited by Ming-Han Ye and Tao Huang, Gordon and Breach Science Publishers, (1988).

[Bi88b] I. Bigi, in *Proceedings of the Sixteenth SLAC Summer Institute on Particles Physics*, edited by E.C. Brennan, SLAC, (1988).

[Br88] T. Browder, *A Study of* D^0 - $\overline{D}^0$ *Mixing*, Ph. D. Thesis, University of California at Santa Barbara, (1988).

[Br94] S. Bracker, Private Communication, (1994).

[Fa78] D. Fakirov and B. Stech, Nucl. Phys. B133, 315 (1978).

[Fe86] R. Fernow, *Introduction to experimental particle physics*, Cambridge University Press, 1986.

[Fr79] A. G. Frodesen, *Probability and Statistics in Particle Physics*, Bergen, 1979.

[Ga93] P. Gagnon, *Measurement of the Form factors in the Semileptonic Decay* $D^+ \rightarrow \overline{K}^{*0} e^+ \nu_e$, Ph. D. Thesis, University of California at Santa Cruz, (1993).

[Gl70] S.L. Glashow *et. al.*, Phys. Rev. D2, 1285 (1970).

[La92] J. F. Labs, *Search for doubly Cabibbo suppressed decays of the charged D Meson*, Ph. D. Thesis, Stanford University, (1992).

[PDG92] The Particle Data Group, *Review of Particle Properties*, Physical Review D 45, (1992).

[Pu90] M. Purohit *et. al.*, *The Princeton Scanner / Controller Manual*, 1990.

[Pu93] M. Purohit, *E791 Čerenkov Identification and Misidentification Probabilities*, E791 Memo, 1993.

[Ra87] J. Raab, *Lifetime Measurements of the Three Charmed Pseudoscalar Mesons*, Ph. D. Thesis, University of California at Santa Barbara, (1987).

[Re94] A. Reis, Private Communication, 1994.

[So94] M. Sokoloff, Private Communication, 1994.

[Th94] K. Thorne, Private Communication, 1994.

[Wi94] N. Witchey, Private Communication, 1994.

[Ya93] H. Yamamoto, in *Proceedings of the workshop on B physics at Hadron Accelerators*, edited by Patricia McBride, FNAL, (1993).